Analysis of a Strange Attractor in $\mathbb{R}^4$

A Thesis

Submitted to the Faculty

of

Drexel University

by

Benjamin Coy

in partial fulfillment of the

requirements for the degree

of

Doctor of Philosophy

December 2011

UMI Number: 3496872

UMI®

Dissertation Publishing

ProQuest®

ProQuest LLC
789 East Eisenhower Parkway
P.O. Box 1346
Ann Arbor, MI 48106-1346

Office of Graduate Studies

Dissertation / Thesis Approval Form

This form is for use by all doctoral and master's students with a dissertation/thesis requirement. Please print clearly as the library will bind a copy of this form with each copy of the dissertation/thesis. All doctoral dissertations must conform to university format requirements, which is the responsibility of the student and supervising professor. Students should obtain a copy of the Thesis Manual located on the library website.

Dissertation/Thesis Title: Analysis of a Strange Attractor in $\mathbb{R}^4$

Author: Benjamin Coy

This dissertation/thesis is hereby accepted and approved.

Signatures:

Examining Committee

    Chair

    Members

    Academic Advisor

    Department Head

Dedications

To my father, Mr. Colin Thomas Coy

Acknowledgments

I am very grateful to my advisor, Dr. Robert Gilmore. When I first began looking for a research topic I was unsure which area of physics to pursue except that I was interested in theoretical work. Dr. Gilmore introduced me to the study of nonlinear dynamics and presented me with the project that eventually lead to this thesis. His dedication to research is truly inspiring.

I would like to thank my colleagues for many useful discussions. In particular Tim Jones, Dan Cross and Ryan Michaluk, it has been a pleasure working alongside each of you.

I would also like thank everyone who helped me settle in when I first moved to Philadelphia. Fiona Hoyle, Randall Rojas and Chris Danchise all helped me a great deal when I began graduate school and for that I am grateful.

I must thank everyone in the department who has helped me and every other graduate student. Especially the head of department, Dr. Michel Vallieres. Also the members of staff Jacqueline Sampson, Janice Wilhelm, Laura D'Angelo and Lisa Ferrara.

Last but not least, I appreciate all of the support and encouragement that my family has given me over the years.

Table of Contents

TABLE OF CONTENTS

vii

TABLE OF CONTENTS

List of Tables

List of Figures

LIST OF FIGURES

Abstract

Analysis of a Strange Attractor in $\mathbb{R}^4$
Benjamin Coy
Robert Gilmore, Ph.D

Strange attractors in $\mathbb{R}^3$ are remarkably well understood because they may be classified through a topological analysis. This involves determining the organization of the unstable periodic orbits in the attractor by computing linking numbers for pairs of these orbits and then identifying a branched manifold that supports these and all other orbits, and serves to identify the mechanism that generates chaotic behavior. This topological invariant can be calculated in $\mathbb{R}^3$ but there is no analog for higher dimensions. We analyze a strange attractor generated by a four dimensional dynamical system and show the first steps in extending the current topological analysis program to higher dimensions. The linking numbers for pairs of unstable periodic orbits are computed in three different ways. Firstly, through projections of the attractor to three dimensional subspaces. Secondly, using a recently proposed higher dimensional linking integral [1] to compute linking numbers in $\mathbb{R}^4$ for the first time. Thirdly, with a dimensionality reduction technique, Locally Linear Embedding, that successfully represents pairs of orbits in three dimensions allowing the organization within the strange attractor to be determined.

Chapter 1: Introduction

A topological analysis program exists for strange attractors generated by three dimensional dynamical systems [2]. The biggest current problem for the analysis of chaotic dynamical systems is that there is no analogous topological analysis program for strange attractors when the dimension is greater than three.

The topological analysis program depends heavily on the unstable periodic orbits within the strange attractor. These orbits can be thought of as forming a skeleton for the attractor and determining the organization of these orbits is a crucial step in the program. In three dimensions, the organization of the orbits is determined by computing Gauss linking numbers. A table of these linking numbers, for pairs of orbits, uniquely describes their organization in the strange attractor. The lack of a higher dimensional analog to the Gauss linking number is the primary reason why the topological analysis program is restricted to three dimensions.

In this thesis I will take the first small steps in breaking through this barrier. I will do this by reviewing the basic steps in the topological analysis program in Chapter 2. In Chapter 3 I then introduce a four-dimensional dynamical system and study the strange attractor that this dynamical system produces. The strange attractor is essentially three-dimensional, in the sense that it has a Lyapunov dimension $D_L < 3$. This means that it should be possible to find an embedding of this attractor in a three-dimensional manifold. Our aim is to extend the topological analysis program to four

dimensions in the case where the strange attractor is three dimensional by "squeezing" or "shoehorning" the attractor into a three-dimensional manifold, straightening out this manifold so that it is essentially a Euclidean space, and then carrying out the standard topological analysis program in this enveloping manifold.

Surrogates for the unstable periodic orbits can be found through the method of close returns [2]. This method will be described in Chapter 4 but the important point is that these surrogates behave very much like the unstable periodic orbits themselves. The method of close returns is a procedure that is easily extended to higher dimensions. We can use it to find surrogate unstable periodic orbits in the attractor in four dimensions but then we need a way to determine their organization.

In Chapter 5 we consider projections of the attractor to three dimensional subspaces. These are the projections (X, Y, Z) and (X, Y, U). We carry out a topological analysis on the attractor, in these projections, by calculating tables of linking numbers in the three dimensional subspaces. In Chapter 6 we explain why some of the surrogate UPO's could not be found for all values of the control parameter, β. The reasons are rather complicated. We determine that this is due to a sequence of homoclinic explosions that are analogous to those in the Lorenz attractor. We calculate the control parameter values at which the UPO's are removed and re-introduced to the attractor for all the UPO's up to period six. In Chapter 7 we compute linking numbers for the UPO's using a second method. This is a recently proposed higher dimensional linking integral for visible hypersurfaces [1]. We are able to find a visible point in $\mathbb{R}^4$ by calculating the minimum distance between rays and the strange attractor. Locating the visible point in this way allows us to compute linking numbers

CHAPTER 1: INTRODUCTION

for UPO's in $\mathbb{R}^4$ for the first time. In Chapter 8 we compare and discuss several techniques for dimensionality reduction. We test some of the most popular nonlinear techniques and determine that the locally linear embedding (LLE) algorithm is well suited to finding a three dimensional manifold containing the strange attractor in $\mathbb{R}^4$. In Chapter 9 we explain, in detail, how the LLE algorithm can be successfully applied to the UPO's within the strange attractor. We generate a three dimensional representation of the UPO's using the LLE algorithm and compute a table of linking numbers for all the UPO's up to period five, which determines the organization of the orbits with the strange attractor. This marks a breakthrough in extending the existing topological analysis program to strange attractors in $\mathbb{R}^4$. Our results are summarized in Chapter 10.

CHAPTER 1: INTRODUCTION

Chapter 2: Topological Analysis Program

2.1 Background

A dynamical system is a set of ordinary differential equations of the form

$$\dot{\mathbf{x}} = \frac{d\mathbf{x}}{dt} = \mathbf{F}(\mathbf{x}; \mathbf{c}) \qquad (2.1)$$

where the variables $\mathbf{x}$ are called state variables and the variables $\mathbf{c}$ are called control parameters. A dynamical system may generate a strange attractor for certain values of the control parameters. Unstable periodic orbits (UPO's) exist in abundance within strange attractors [3] and a topological analysis of the strange attractor is based upon these orbits. The steps in this program are as follows [4],

1. Find the unstable periodic orbits

2. Compute topological invariants

3. Identify a template

4. Verify the template

We elaborate on each of these steps in the next four sections.

2.2 Finding orbits

Unstable periodic orbits are located by finding an initial condition that evolves around the attractor and returns the neighborhood of it's starting point. These are segments

in a chaotic data set that almost close up. When this occurs, the difference $|\mathbf{x}(t) -$ $\mathbf{x}(t + T)|$ remains small for awhile, where T is the time for one period. The periodic orbits found in this way are called surrogate periodic orbits. Since they lie in the neighborhood of the unstable periodic orbit they behave similarly to the orbit itself. This method of finding orbits is known as the method of close returns and more details are given in Chapter 4.

2.3 Computing topological invariants

The topological invariants, linking numbers for pairs of orbits, can be determined by computing the Gauss linking number [5, 6]. This topological invariant is calculated for all surrogate UPO's found by the method of close returns.

The Gauss linking number is defined by

$$\mathrm{LN}(A, B) = \frac{1}{4\pi} \oint_A \oint_B \frac{(\mathbf{r}_A - \mathbf{r}_B) \cdot (d\mathbf{r}_A \times d\mathbf{r}_B)}{|\mathbf{r}_A - \mathbf{r}_B|^3} \tag{2.2}$$

where A and B are two loops in $\mathbb{R}^3$ described by two three-vectors $\mathbf{r_A}$ and $\mathbf{r_B}$. An alternative but equivalent method [4] for computing the linking number is by counting crossings in a two-dimensional projection. Each intersection of the orbits in the projection is assigned an integer ± 1. Figure 2.1 shows how the sign is determined, right handed crossing are assigned a value $+1$ and left handed crossings -1. The linking number is half the sum of the signed crossings.

CHAPTER 2: TOPOLOGICAL ANALYSIS PROGRAM
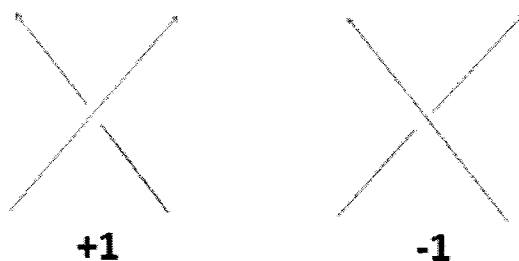
Figure 2.1: Signed crossings of oriented curves in a two-dimensional projection.

2.4 Identify a template

Each surrogate periodic orbit is assigned a name, using a symbolic sequence, and a template is proposed that is consistent with a few of the lowest period surrogate UPO's. This identification with a branched manifold relies on following the Birman-Williams theorem [7, 8]. Before the theorem is stated points in phase space are identified if they have the same asymptotic future, by the following projection,

$$\mathbf{x} \approx \mathbf{y} \quad \text{if} \quad |\mathbf{x}(t) - \mathbf{y}(t)| \xrightarrow{t \to \infty} 0 \tag{2.3}$$

This identification corresponds to projecting the flow along the stable direction to a two-dimensional branched manifold. Under this projection the forward flow is uniquely determined but these trajectories no longer have unique histories. The flow in $\mathbb{R}^3$ becomes a semi-flow on the branched manifold. The important aspect of the Birman-Williams theorem is that when a strange attractor is projected down to the branched manifold the unstable periodic orbits remain unchanged, in the following way. In the projection, there are the same number and type of periodic orbits with

---

CHAPTER 2: TOPOLOGICAL ANALYSIS PROGRAM

the same topological organization as those in the strange attractor.

2.5   Verify the template

The template is verified by computing a table of linking numbers for all pairs of the surrogate UPO's that are found by the method of close returns. A table of the linking numbers for pairs of periodic orbits describes their organization on the branched manifold and within the strange attractor. The mechanism that produces the strange attractor can be identified from the particular type of branched manifold.

CHAPTER 2: TOPOLOGICAL ANALYSIS PROGRAM

Chapter 3: A Four-Dimensional Dynamical System

In this chapter we present the dynamical system that will be considered throughout this thesis. In Section 3.1 the physical origin of the autonomous differential equations is explained in terms of a series of dynamo systems introduced by Hide [9]. The dynamo equations are then simplified and in Section 3.3 they are changed to dimensionless form. In Section 3.4 the dimensionless equations are transformed to the extended Malkus-Robbins equations. Lastly, the strange attractor generated by these equations and their connection to the Lorenz system are discussed.

3.1 Origin of the equations

A hierarchy of dynamo systems was introduced in a seminal paper by Hide [9]. Each member of the hierarchy consists of a number of units connected, either in a ring or lattice, where each unit contains a homopolar dynamo driven by a Faraday disk. Within each unit are a number of motors connected either in series or parallel with the coil of the dynamo. Each system is labeled as $S(N; \mathbf{J}(i))$, where N is the number of units and $\mathbf{J}(i)$ is the number of motors contained in the units, $i = 1, 2, ..., N$.

The behavior of each system is governed by a set of autonomous nonlinear differential equations. Some of the simplest members of the hierarchy correspond to previously studied dynamo systems. These include an $S(1; 0)$ system studied by Bullard [10]; an $S(2; 0, 0)$ system studied by Rikitake [11] and an $S(1; 3)$ system proposed by Malkus [12] and studied by Robbins [13]. We will focus on the $S(1; 3)$ system and

show how, under certain simplifying assumptions, the governing differential equations are an extended form of the Malkus-Robbins dynamo. In the literature [14, 15], these equations have been transformed and recast into several different forms. Here we will derive the set of nonlinear differential equations directly from considerations of the dynamo system. This is a two-step procedure where the equations are first re-written in terms of dimensionless variables in Section 3.3 and then transformed to their final form in Section 3.4.

This model is a four dimensional dynamical system with two properties that make it ideal for extending the existing methods for topological analysis in $\mathbb{R}^3$. The first is that the model reduces to a well-known system, namely the Lorenz system, in a particular limit of the control parameter values. The second is that the attractor has a Lyapunov dimension that is less than three, such that it is essentially three dimensional. That is, in principle, there is a three dimensional manifold in which the strange attractor generated by this dynamical system can be embedded [16].

3.2 The Dynamo Equations

Here we consider an $S(1;3)$ type system which consists of a single unit Faraday disk and three electric motors. Figure 3.1 shows the coil and the disk connected in series and three motors. Each motor is labelled according to its connection to the rim, axle or coil as m_r, m_a and m_c respectively.

The first motor, m_r, is connected through one terminal to a brush at the rim of the disk. The second terminal is connected to a junction common to all three motors. This places m_r in series with m_a and the axle. It also connects m_r in series with

---
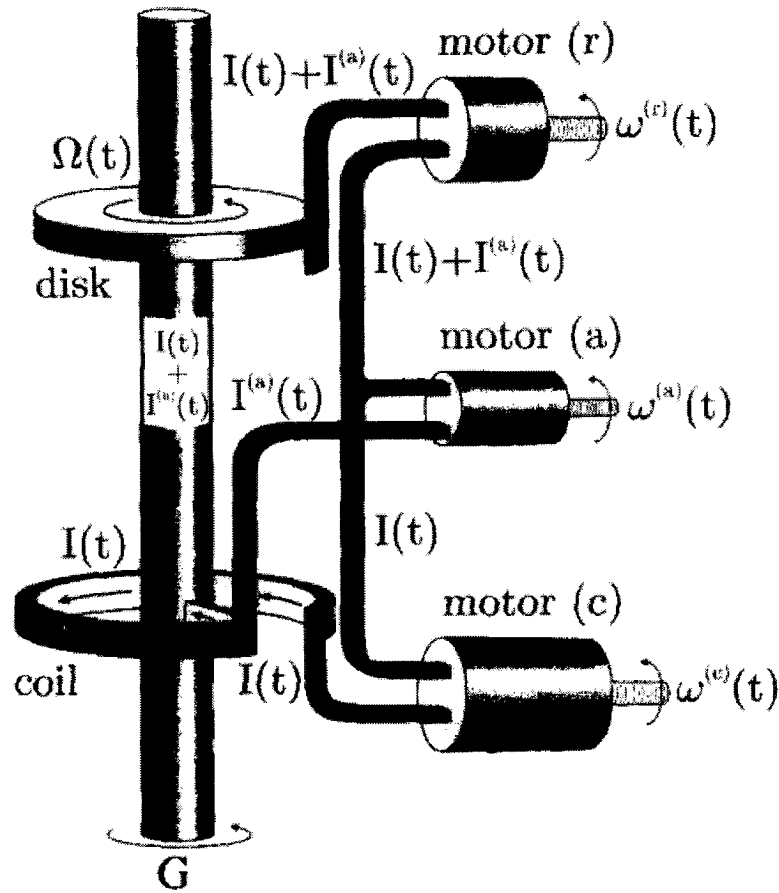
Figure 3.1: Illustration of an $S(1;3)$ type system. Image taken from [9]. Here $I(t) = I_c(t)$, the current through the coil

the motor m_c and the coil. The two motors, m_a and m_c, are connected in parallel, with m_a connected to the axle and m_c connected to the coil. The equivalent circuit diagram for this setup is shown in Figure 3.2. The current, I, resistance, R, self-inductance, L, and angular speed of the motor, ω, for each branch of the circuit are labelled using the same convention as the motors. The subscripts r, a or c, indicate that the branch of the circuit is connected to the rim, axle or coil respectively.

CHAPTER 3: A FOUR-DIMENSIONAL DYNAMICAL SYSTEM
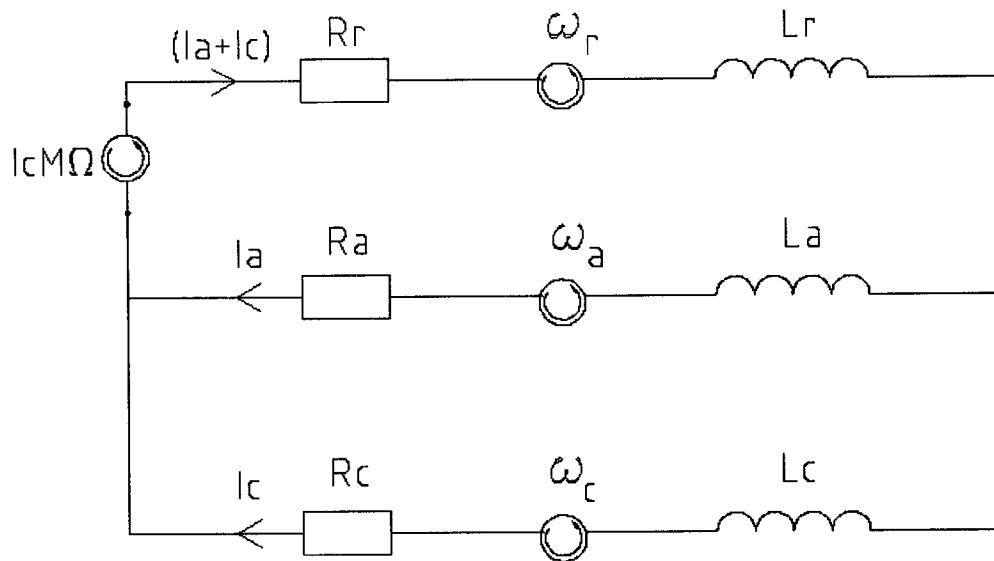
Figure 3.2: Equivalent circuit diagram for the $S(1;3)$ type system

To simplify the system, and allow for comparison with the Malkus-Robbins dynamo, the motor m_a is replaced by a resistor and m_r by an element with inductance and resistance only. In terms of the quantities given in Figure 3.2, we have

$$\omega_a = L_a = \omega_r = 0 \tag{3.1}$$

The emf generated by the motion of the disk is given by $I_c M \Omega$ where I_c is the current through the coil, Ω is the angular velocity of the disk and $2\pi M$ is the mutual inductance of the disk and coil [17]. This emf must be balanced by the sum of the

voltage drops throughout the circuit. The sum of these voltage drops gives,

$$I_c M \Omega = L_c \frac{dI_c}{dt} + L_r \frac{d(I_c + I_a)}{dt} + (I_c + I_a)R_r + I_c R_c + H_c \omega_c \qquad (3.2)$$

The last term is the voltage drop across the motor. The motors are assumed to have linear characteristics such that the voltage drop is proportional to the angular speed of the motor. If we denote the proportionality constant by H then the voltage drop is given by $H\omega$ where ω is the angular speed of the armature of the motor.

Next we consider the dynamics of the disk. The moment of inertia of the disk is denoted by A and the applied torque by G. The mechanical friction of the disk provides a retarding torque given by $-K\Omega$. Newton's second law then gives

$$A \frac{d\Omega}{dt} = G - M I_c (I_a + I_c) - K\Omega \qquad (3.3)$$

Applying Newton's second law to the motor, m_c, we find that

$$B_c \frac{d\omega_c}{dt} = H_c I_c - D_c \omega_c \qquad (3.4)$$

where B_c is the moment of inertia and ω_c is the angular velocity of m_c. The torque of the motor is proportional to the current flowing through it and is given by $H_c I_c$. Finally the term $-D_c \omega_c$ is the retarding torque due to friction. Since m_c and m_a are in parallel, the final equation required to describe the system is obtained by equating

CHAPTER 3: A FOUR-DIMENSIONAL DYNAMICAL SYSTEM

the voltage drops across these two motors.

$$I_a R_a = I_c R_c + L_c \frac{dI_c}{dt} + H_c \omega_c \qquad (3.5)$$

3.3 Dimensionless Equations

To write the four differential equations in dimensionless form we use the following

substitutions

$$\tau = \left(\frac{R_c}{L_c}\right) t \qquad (3.6)$$

$$x_a = \left(\frac{M}{G}\right)^{1/2} I_a \qquad (3.7)$$

$$x_c = \left(\frac{M}{G}\right)^{1/2} I_c \qquad (3.8)$$

$$y = \left(\frac{M}{R_c}\right) \Omega \qquad (3.9)$$

$$z_c = \left(\frac{M}{G}\right)^{1/2} \left(\frac{R_c B_c}{L_c H_c}\right) \omega_c \qquad (3.10)$$

$$r_{a,r} = R_{a,r}/R_c \qquad (3.11)$$

CHAPTER 3: A FOUR-DIMENSIONAL DYNAMICAL SYSTEM

$$l_{a,r} = L_{a.r}/L_c \tag{3.12}$$

$$x_{ac} = x_a + x_c \tag{3.13}$$

This leads to the following set of differential equations

$$\frac{dx_c}{d\tau} = r_a x_a - x_c - \left(\frac{L_c H_c^2}{B_c R_c^2}\right) z_c \tag{3.14}$$

$$\frac{dx_{ac}}{d\tau} = \frac{1}{l_r}\left(x_c y - r_a x_a - r_r x_{ac}\right) \tag{3.15}$$

$$\frac{dy}{d\tau} = \left(\frac{GML_c}{AR_c^2}\right)(1 - x_c x_{ac}) - \left(\frac{KL_c}{AR_c}\right) y \tag{3.16}$$

$$\frac{dz_c}{d\tau} = x_c - \left(\frac{D_c L_c}{B_c R_c}\right) z_c \tag{3.17}$$

3.4 Transformed Equations

The dimensionless equations can be transformed to take a similar form to the Malkus-Robbins dynamo equations. We use the following substitutions

$$z_c = aU \tag{3.18}$$

$$x_c = bX \tag{3.19}$$

$$y = c(d - Z) - r_a \tag{3.20}$$

$$x_{ac} = eY \tag{3.21}$$

$$\tau = fT \tag{3.22}$$

The transformed dimensionless equations are

$$\frac{dX}{dT} = r_a \left(\frac{ef}{b}\right) Y - (1 + r_a)fX - \left(\frac{L_c H_c^2}{B_c R_c^2}\right) fU \tag{3.23}$$

$$\frac{dY}{dT} = \frac{1}{l_r} \left[\left(\frac{bcdf}{e}\right) X - \left(\frac{bcf}{e}\right) XZ - (r_a + r_r)fY\right] \tag{3.24}$$

$$\frac{dZ}{dT} = \left(\frac{L_c}{AR_c}\right) \left(dfK - \frac{fGM}{cR_c} - \frac{fKr_a}{c}\right) + \left(\frac{befGML_c}{cAR_c^2}\right) XY - \left(\frac{fKL_c}{AR_c}\right) Z \tag{3.25}$$

$$\frac{dU}{dT} = \left(\frac{bf}{a}\right) X - \left(\frac{D_c L_c}{B_c R_c}\right) fU \tag{3.26}$$

These transformed equations are the extended Malkus-Robbins equations which we

CHAPTER 3: A FOUR-DIMENSIONAL DYNAMICAL SYSTEM

will now write in the more familiar form

$$\dot{X} = \sigma(Y - X) - \hat{\beta}U \qquad (3.27a)$$

$$\dot{Y} = \frac{RX}{\nu} - Y - XZ \qquad (3.27b)$$

$$\dot{Z} = -\nu Z + XY \qquad (3.27c)$$

$$\dot{U} = X - \Lambda U \qquad (3.27d)$$

where differentiation is performed with respect to T and $\hat{\beta} = \nu^2 \beta$. The control parameters are obtained under the following correspondence,

$$a = \left(\frac{AR_c^2}{GML_c}\right)^{1/2} \sqrt{l_r} \qquad (3.28)$$

$$b = \left(\frac{AR_c^2}{GML_c}\right)^{1/2} \frac{r_a + r_r}{\sqrt{l_r}} \qquad (3.29)$$

$$c = (r_a + r_r)(1 + 1/r_a) \qquad (3.30)$$

$$d = \frac{r_a + \frac{GM}{KR_c}}{(r_a + r_r)(1 + 1/r_a)} \qquad (3.31)$$

CHAPTER 3: A FOUR-DIMENSIONAL DYNAMICAL SYSTEM

$$e = \left(\frac{AR_c^2}{GML_c}\right)^{1/2} \frac{(r_a + r_r)(1 + 1/r_a)}{\sqrt{l_r}} \qquad (3.32)$$

$$f = \frac{l_r}{r_a + r_r} \qquad (3.33)$$

such that,

$$\sigma = (1 + r_a)f \qquad (3.34)$$

$$\hat{\beta} = \left(\frac{L_c H_c^2}{B_c R_c^2}\right) f \qquad (3.35)$$

$$R/\nu = \frac{1}{l_r}\left(\frac{bcdf}{e}\right) \qquad (3.36)$$

$$\Lambda = \left(\frac{D_c L_c}{B_c R_c}\right) f \qquad (3.37)$$

The dynamical system in the form of Equations (3.27) will be used in subsequent chapters and referred to as the EMR (Extended Malkus-Robbins) equations.

These dynamical equations are an extension of the Malkus-Robbins dynamo equations [13]. They essentially describe a Lorenz-like system with feedback. The strange attractor generated by the (X, Y, Z) subsystem behaves like a Lorenz attractor [18] that is coupled to the U subsystem through the control parameter β. When $\beta = 0$

CHAPTER 3: A FOUR-DIMENSIONAL DYNAMICAL SYSTEM

Equations (3.27) become identical to the Lorenz equations under the correspondence,

$$(\sigma, R/\nu, \nu) \rightarrow (\sigma, r, b). \tag{3.38}$$

The classic choice of Lorenz parameters $(\sigma, b, r) = (10, 8/3, 28)$ corresponds to $(\sigma, \nu, R) = (10, 8/3, 74.667)$. These values will be used throughout along with $\Lambda = 3.2$. For this particular choice of the control parameters chaotic solutions extend well into the $\beta > 0$ regime, until $\beta \approx 8$ at which point a boundary crisis destroys the attractor [19]. We will consider the strange attractor generated by Equation (3.27) for these values of the control parameters over the range of values $0 \leq \beta \leq 8.0$. An X-Z projection of the strange attractor for $\beta = 3.0$ is shown in Figure 3.3. In this projection the attractor bears a strong similarity to the Lorenz attractor. This projection exhibits the same type of symmetry as the Lorenz attractor, rotation about the Z-axis, and reduces to the Lorenz system as $\beta \rightarrow 0$.

3.5 Summary

We have presented the four-dimensional dynamical system, Equations (3.27), that will be considered throughout subsequent chapters. The physical origin of these equations was given in terms of the electro-mechanical self-exciting Faraday-disk homopolar dynamo systems first introduced by Hide [9]. The dynamo equations were then recast and transformed in Sections 3.3 and 3.4 to give the extended Malkus-Robbins equations.

The strange attractor generated by this dynamical system was also discussed.

CHAPTER 3: A FOUR-DIMENSIONAL DYNAMICAL SYSTEM
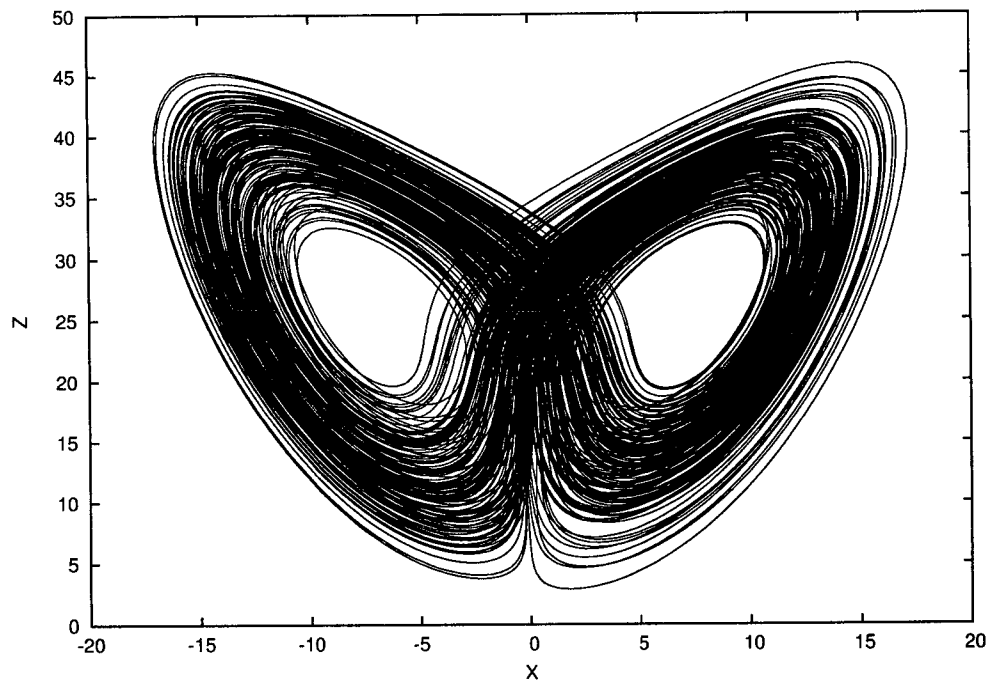
Figure 3.3: The X-Z projection of the strange attractor for $(\sigma, \nu, R, \beta, \Lambda) = (10, 8/3, 74.667, 3.0, 3.2)$.

The two key features of this attractor are that it reduces to the well-known Lorenz attractor for $\beta = 0$ and that it has Lyapunov dimension, $D_L \simeq 2.2$ [16]. The first feature makes this attractor an ideal model for further study since results can be compared to the Lorenz attractor for low values of the control parameter, β. The fact that we have $D_L < 3$ is appealing because, although the attractor exists in $\mathbb{R}^4$, it is essentially three dimensional. This makes the strange attractor an ideal candidate for extending existing methods, the computation of Gauss linking numbers, that have been successfully applied to strange attractors in $\mathbb{R}^3$.

CHAPTER 3: A FOUR-DIMENSIONAL DYNAMICAL SYSTEM

Chapter 4: Analysis of the Surrogate UPO's in $\mathbb{R}^4$

The key to analyzing low dimensional ($d < 3$) strange attractors is through the organization of their unstable periodic orbits (UPO's) [20]. Even though the topological tools used in this analysis cannot be directly applied in higher dimensions, we continue to focus on the UPO's whilst searching for useful methods to determine their organization. The method of close returns [2] is used to find the surrogate UPO's for low dimensional attractors and this technique is easily extended to higher dimensions.

In Section 4.1 we describe the procedure for finding the surrogates using the method of close returns. In Section 4.2 we show how two components of a Poincaré section can be used to label each of the surrogate UPO's. The efficiency for finding these surrogates is improved in Section 4.3. In Section 4.4 we demonstrate how a Fourier representation of UPO's can be used to construct surrogates for particular values of the control parameter, β.

4.1 Finding surrogate UPO's through the method of close returns

UPO's are abundant in strange attractors and initial conditions lying close to a UPO will remain close to the orbit for some amount of time. If the initial condition is close enough to a UPO along its unstable manifold, and its unstable Lyapunov exponent is not too large, the initial condition will evolve to a neighborhood of its starting point [2]. Such a trajectory lies close to the UPO for a full period and so behaves very

similarly to the UPO itself. These trajectories are called surrogate UPO's, they can be obtained from the time series data for the strange attractor. They are found by locating segments of the time series that close up such that a succession of point pairs in the time series lie close together. For an attractor in $\mathbb{R}^4$ the condition is

$$\|\mathbf{X}_{i+k} - \mathbf{X}_{j+k}\| < \delta \tag{4.1}$$

where $\mathbf{X_i} = \mathbf{X}(t_i)$, $\|\mathbf{X}\| = \sqrt{X^2 + Y^2 + Z^2 + U^2}$ and $k = 0, 1, 2...m$ such that the closeness condition holds for some time t_m, that is a reasonable fraction of the time-period of a period one orbit.

The parameter δ is usually chosen to be about 1% of the diameter of the strange attractor [4]. The actual value used depends on a compromise between the accuracy of the surrogates and how many are required. A more stringent threshold will result in fewer surrogates that are very good in the sense that they close up well and represent the UPO accurately.

4.2 Using Poincaré sections

Each surrogate orbit can be labeled using a symbol representation introduced by Moroz et al [16] which is based on the labeling used for the Lorenz attractor [21, 22]. The symbol representation is a sequence of the symbols L and R indicating passage in the neighborhood of the left or right focus respectively (cf. Figure 3.3). This passage is checked by the use of a Poincaré section consisting of two half infinite planes, each centered on one of the foci of the attractor. The number of times that a surrogate

CHAPTER 4: ANALYSIS OF THE SURROGATE UPO'S IN $\mathbb{R}^4$

UPO intersects these two planes, before approximately returning to its starting point, is the topological period of the orbit. For example, the period three orbit shown in Figure 4.1 intersects the left component of the Poincaré section once and the right component twice.
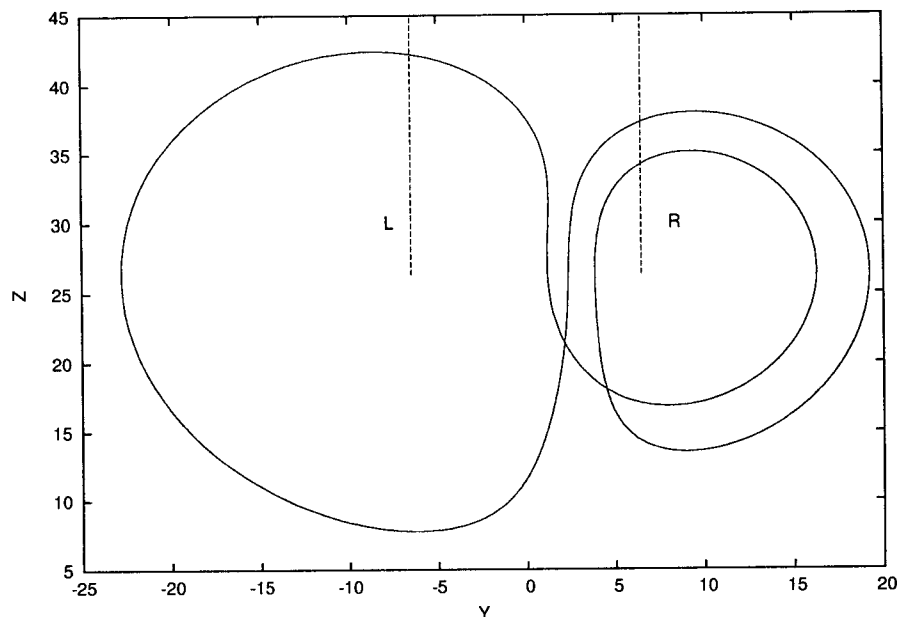
Figure 4.1: A surrogate period three orbit, found by the method of close returns, for $\beta = 3.0$ in Equations 3.27. The flow is directed counter-clockwise around the right hand focus. The point of close return is located at $(Y, Z) = (-1.59, 9.33)$. The dashed vertical lines are the two components of the Poincaré section.

Figure 4.1 illustrates the natural way to label each of the UPO's. Every orbit is labeled by a sequence of two symbols, L and R, indicating the order of intersection with component L or R of the Poincaré section. Under this labeling scheme the orbit shown in Figure 4.1 is LR^2. Checking for close returns only when the trajectory crossed the Poincaré did not yield a sufficient number of surrogates as the control parameter, β, was increased. This is why the point of close return in Figure 4.1 is not located near either component, L or R, since the closeness condition, given by

CHAPTER 4: ANALYSIS OF THE SURROGATE UPO'S IN $\mathbb{R}^4$

Equation 4.1, was continually checked along the trajectory to find a greater number of surrogate UPO's over the range of control parameter values.

4.3 Incorporating the time-period of orbits

The time period of an orbit is dependent on the control parameter value, β. Finding surrogates for a periodic orbit for several values of the control parameter shows that it is possible to fit this dependence with a smooth curve. This is displayed by Figure 4.2 where the fit has been made by a polynomial of degree two for the UPO $LLRR$. It was found that a quadratic fit could be used for all the low period orbits, up to period six.
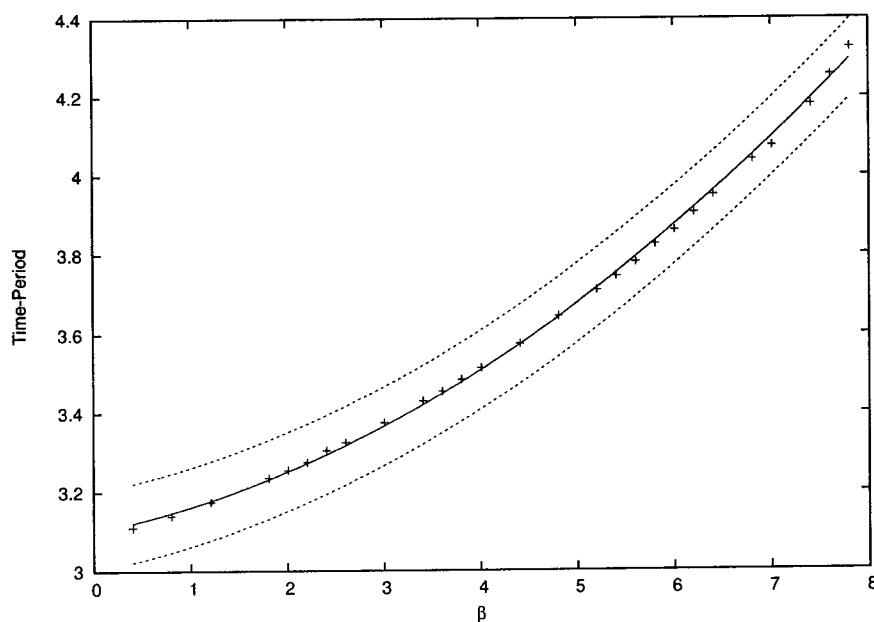
Figure 4.2: Time-period as a function of β for the UPO L^2R^2. The solid line shows the quadratic fit to the data and the dashed lines show the tolerance used to find more surrogates.

The predictable dependence of the time-period of a surrogate allows the method of close returns to be used more efficiently. This is achieved by setting a tolerance

CHAPTER 4: ANALYSIS OF THE SURROGATE UPO'S IN $\mathbb{R}^4$

on the time-period. Figure 4.2 shows the tolerance used for the orbit L^2R^2. For each

point in the data set only the future points lying within the tolerance range were

checked for close returns, significantly improving the efficiency of the algorithm. The

time-periods for all the orbits found using this method are shown in Figure 4.3
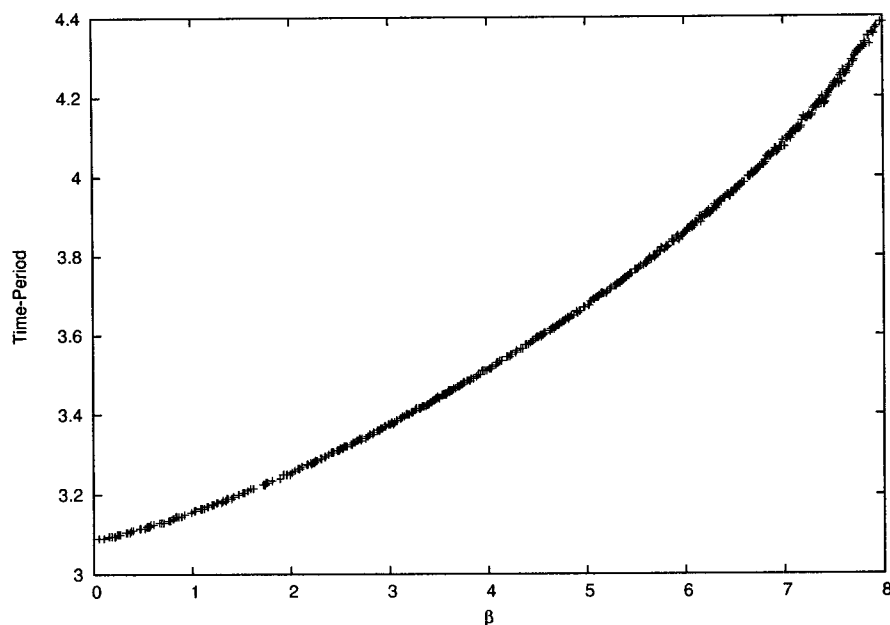
Figure 4.3: Time-period as a function of β for all the surrogate UPO's L^2R^2 found using the tolerance shown in Figure 4.2.

4.4 Fourier representation of UPO's

4.4.1 Parsing The Orbits

Once a surrogate periodic orbit has been extracted, a Fast Fourier Transform (FFT)

[23] is performed on the time series data. However, this requires that the time series

has 2^n data points where n is an integer. To fulfill this requirement linear interpolation

is used to expand or shrink the time-step.

For example, the time-series for a surrogate period two orbit is shown in Figure

CHAPTER 4: ANALYSIS OF THE SURROGATE UPO'S IN $\mathbb{R}^4$

4.4a. This particular orbit contains 158 data-points. Figure 4.4b shows the time series after it has been parsed to $2^8 = 256$ data-points. The x coordinates of the orbit are computed for 256 equally spaced time intervals t_n. If the time for one complete orbit is T then the t_n are given by

$$t_n = \frac{nT}{256} \tag{4.2}$$

where $0 \leq n \leq 255$.

(a) Surrogate period two orbit   (b) Parsed orbit with 256 data-points
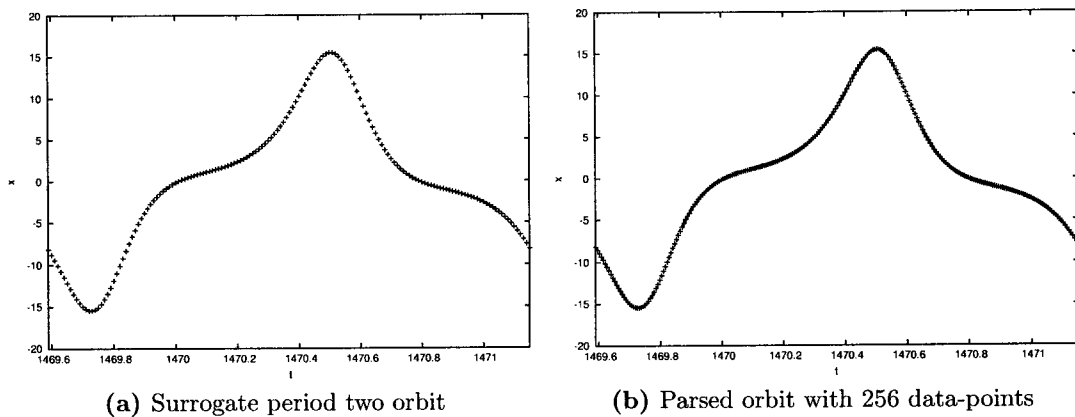
Figure 4.4: x-coordinate time series for the period two orbit, LR.

The x coordinates are computed by linear interpolation of the two nearest points from the original time series. The very first point of the parsed time series will be identical to the original while all the others will be interpolated values.

The same process is repeated for each of the other three coordinates. This results in four parsed time series each containing 256 data-points.

CHAPTER 4: ANALYSIS OF THE SURROGATE UPO'S IN $\mathbb{R}^4$

4.4.2   Computing the Fourier Coefficients

The next step in finding a Fourier representation of the UPO's is to compute their Fourier coefficients. This involves performing a Fast Fourier Transform on each orbit for several values of the control parameter, β.

First we will consider a single orbit for a fixed value of β. For example, the period two orbit, LR, for $\beta = 0$. The parsed time series for the x coordinate of this orbit is shown in Figure 4.4b. We represent this discrete time-series as,

$$x_j(\beta) = x(t_j) = x(j\Delta), \qquad j = 0, 1, 2, ..., N - 1 \tag{4.3}$$

where $\Delta = T/N$. Performing an FFT, using a standard method [24], on this time series will produce $N = 2^n$ complex Fourier coefficients given by,

$$X_k(\beta) = \sum_{j=0}^{N-1} x_j(\beta) e^{2\pi i j k/N} \tag{4.4}$$

These Fourier coefficients can be used to express the orbit as a sum using the discrete inverse Fourier transform,

$$x_j(\beta) = \frac{1}{N} \sum_{k=0}^{N-1} X_k(\beta) e^{-2\pi i j k/N} \tag{4.5}$$

If we express the Fourier coefficients in terms of real and imaginary parts as

$$X_k(\beta) = A_k(\beta) + iB_k(\beta) \tag{4.6}$$

CHAPTER 4:   ANALYSIS OF THE SURROGATE UPO'S IN $\mathbb{R}^4$

and use the fact that the original data set, $x_j(\beta)$, consisted only of real numbers, then the sum in Equation (4.5) reduces to

$$x_j(\beta) = \frac{1}{N} \sum_{k=0}^{N-1} A_k(\beta)\cos(\theta) + B_k(\beta)\sin(\theta) \qquad (4.7)$$

where $\theta = \frac{2\pi jk}{N}$.

However, not all of the N complex coefficients are required to produce the orbit accurately. The highest frequency components can be neglected since they are only present because the surrogate orbit does not close up completely (Gibbs phenomenon [25]). For $N = 256$, it was found that forty coefficients were sufficient to produce periodic orbits with this method. Figure 4.5 shows a plot of $|A_k|^2 + |B_k|^2$, on a logarithmic scale, for the surrogate orbit $LRRR$ with, $\beta = 4.5$, and clearly shows that the Fourier coefficients at the higher frequencies only give a negligible contribution to the sum in Equation 4.7. Therefore, finding the first forty coefficients for each coordinate (x, y, z, u) is sufficient to produce the UPO for a fixed value of the control parameter in the range $0 \leq \beta \leq 8$.

4.4.3 Fitting the Fourier Coefficients

The purpose of computing the Fourier coefficients for each orbit is to be able to produce the orbits for any value of the control parameter β. In order to do this the coefficients must be computed for each orbit at several values of the control parameter.

As an example, consider the period 3 orbit LLR. If this orbit has been found for several values of β, using the method of close returns, we can compute the Fourier coefficients for each value of the control parameter.

CHAPTER 4: ANALYSIS OF THE SURROGATE UPO'S IN $\mathbb{R}^4$
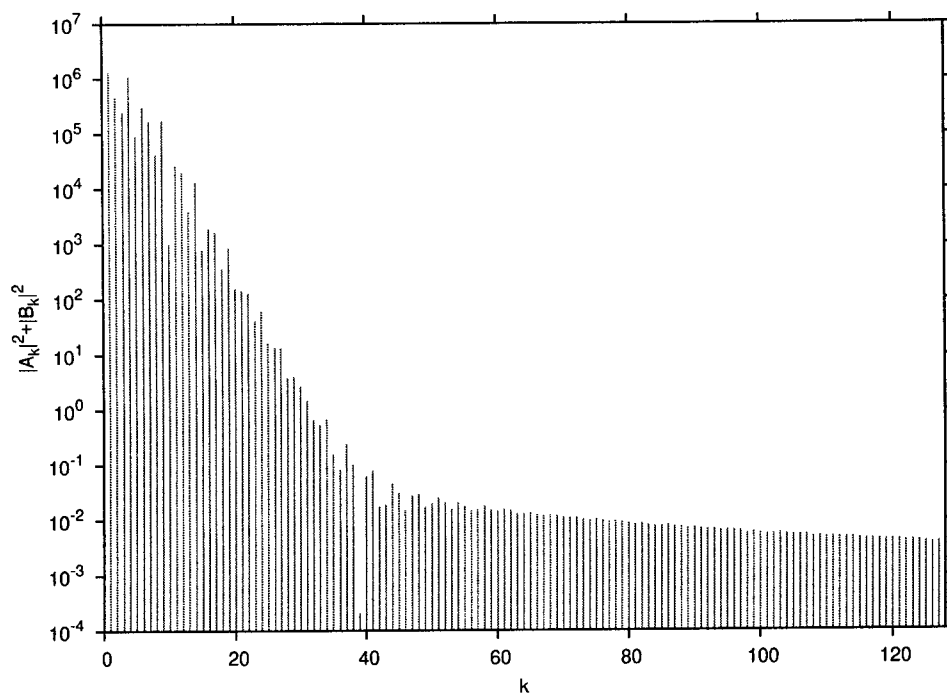
Figure 4.5: Power spectrum plot of $|A_k|^2 + |B_k|^2$ as a function of k for the x-coordinate time series data of the orbit $LRRR$ with $\beta = 4.5$.

A plot of the first Fourier coefficient, A_0 ,as a function of β is shown in Figure 4.6. It is possible to fit this plot with a smooth curve which parametrizes the Fourier coefficient. It was found that every Fourier coefficient could be approximated by a polynomial of degree three for all the orbits up to period five. The coefficients of these polynomials, $a_{k,i}$, $b_{k,i}$, can then be used to compute the Fourier coefficients for any value of β.

$$A_k(\beta) = a_{k,0} + a_{k,1}\beta + a_{k,2}\beta^2 + a_{k,3}\beta^3 \qquad (4.8)$$

$$B_k(\beta) = b_{k,0} + b_{k,1}\beta + b_{k,2}\beta^2 + b_{k,3}\beta^3 \qquad (4.9)$$

Repeating the process for each coordinate (x, y, z, u) gives a complete Fourier representation of each UPO found in the strange attractor.

4.4.4 Producing an Orbit for any Value of the Control Parameter

Producing a UPO for any given value of β involves three steps that invert the process described above.

The first step is to compute the Fourier coefficients for a chosen value of β. The Fourier coefficients can be found from Equations 4.8 and 4.9 using the known values of the polynomial coefficients.

The next step is to produce the coordinates of the orbit from the Fourier coefficients. For example, the x-coordinates can be found from equation 4.7 using the first forty Fourier coefficients.

CHAPTER 4: ANALYSIS OF THE SURROGATE UPO'S IN $\mathbb{R}^4$
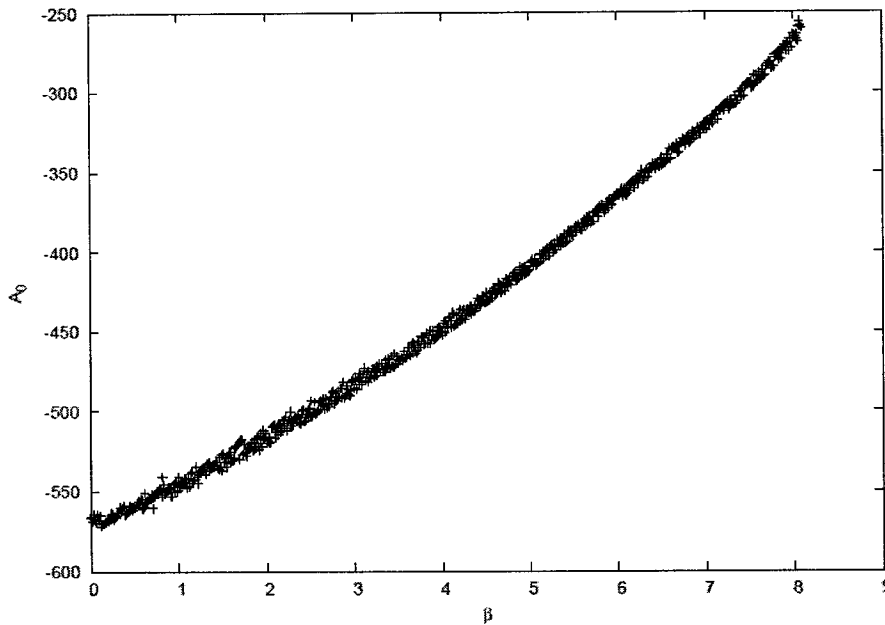
Figure 4.6: Plot of the first Fourier coefficient as a function of β for the period three orbit LLR.

Lastly, the procedure is repeated for each of the other three coordinates to construct the entire UPO for a specified value of the control parameter, β.

4.4.5 Remarks

The methods described here can be used to construct UPO's for any specified value of control parameters. There are two main requirements to use this method. Firstly, the UPO's must be found for several values of the control parameter. This can often be achieved through the method close returns. The second requirement is that the Fourier coefficients can be fitted by a polynomial such as in Figure 4.6. This will be possible when the UPO changes smoothly or "adiabatically" as the control parameter is varied.

CHAPTER 4: ANALYSIS OF THE SURROGATE UPO'S IN $\mathbb{R}^4$

If both these requirements are met then the method can be used to construct UPO's without searching for surrogate orbits in the strange attractor every time the control parameter is changed. Once the polynomial coefficients have been found in equations 4.8 and 4.9 the UPO's can be constructed for any value of the control parameter. The method is a very useful tool for analyzing the topological properties of UPO's as the control parameters are varied.

4.5 Summary

We have described in this chapter how the method of close returns can be applied in $\mathbb{R}^4$ to find surrogate UPO's. In Section 4.2 we explained how each surrogate is assigned a symbolic description using the Poincaré section. We also showed how incorporating the time-period of orbits can improve the efficiency of the method of close returns. In Section 4.4 we introduced the Fourier representation of UPOs and showed how this can be used to generate surrogate orbits for particular control parameter values.

CHAPTER 4: ANALYSIS OF THE SURROGATE UPO'S IN $\mathbb{R}^4$

Chapter 5: Three-Dimensional Projections

The mechanism responsible for creating a low dimensional strange attractor and organizing all the UPO's in it can be determined through a topological analysis of the dynamical system. The procedure for this involves computing topological invariants of the UPO's, their linking numbers, in $\mathbb{R}^3$.

The strange attractor generated by Equations (3.27) exists in $\mathbb{R}^4$ and the organization of the UPO's cannot be determined in the same way as for $\mathbb{R}^3$ since knots fall apart for dimensions greater than three. However, for the control parameter values given in Section 3.4, the Lyapunov dimension of the attractor is $D_L < 3$. This is an important property because it means that the attractor is essentially three-dimensional in the sense that there is a three-dimensional manifold in which the attractor can be embedded [16].

In this chapter we will review a previous study [16] on the strange attractor generated by the EMR Equations (3.27). This work involves projections of the attractor to three-dimensional sub-spaces in order to carry out a topological analysis. The two simplest projections are $(X, Y, Z, U) \to (X, Y, Z)$ and $(X, Y, Z, U) \to (X, Y, U)$.

By constructing a table of the linking numbers in a projection for just the lowest period UPO's it is possible to see if these topological indices are compatible with a branched manifold. In principle, the linking numbers for all UPO's should be checked. However, in practice, it has been found that computing linking numbers for about

half a dozen orbits is often sufficient [2, 4, 26]. It is this branched manifold that identifies the mechanism responsible for the chaotic behavior.

In the (X, Y, Z) subspace the linking numbers are expected to be consistent with the Lorenz branched manifold for small values of the control parameter β. This branched manifold has a rotational symmetry, $(X, Y, Z) \to (-X, -Y, Z)$, and the table of linking numbers for the low period orbits is given in Table 5.1. The (X, Y, U) subsystem exhibits inversion symmetry, $(X, Y, U) \to (-X, -Y, -U)$, and the linking numbers for the inversion symmetric Lorenz branched manifold are given in Table 5.2.

We will focus on these two projections and present a new result for the (X, Y, U) subspace by analyzing surrogate UPO's up to period five.

Table 5.1: Linking numbers of low period orbits in the rotation-symmetric Lorenz branched manifold.

	LR	LLR	LRR	LLLR	LRRR	LLRR
LR	-	1	1	1	1	2
LLR	1	-	1	2	1	2
LRR	1	1	-	1	2	2
LLLR	1	2	1	-	1	2
LRRR	1	1	2	1	-	2
LLRR	2	2	2	2	2	-

CHAPTER 5: THREE-DIMENSIONAL PROJECTIONS

Table 5.2: Linking numbers of low period orbits in the inversion-symmetric Lorenz branched manifold.

	LR	LLR	LRR	$LLLR$	$LRRR$	$LLRR$
LR	-	0	0	0	0	0
LLR	0	-	0	+1	0	+1
LRR	0	0	-	0	−1	−1
$LLLR$	0	+1	0	-	0	+1
$LRRR$	0	0	−1	0	-	−1
$LLRR$	0	+1	−1	+1	−1	-

5.1 Review of previous work on "When are projections embeddings?"

Moroz *et al* [16] have investigated projections of the strange attractor generated by Equations (3.27) to determine which projections provide embeddings. This was achieved through a topological analysis based upon the UPO's within the attractor. Surrogate UPO's were found using the method of close returns and then projected to a three dimensional subspace such that their linking numbers could be calculated. The linking numbers for pairs of surrogate UPO's were found by counting crossings in a two-dimensional projection. Tables of the linking numbers were computed for each of the projections over the control parameter range $0 < \beta < 8$.

The (X, Y, Z) projection produced a table of linking numbers that changed as the control parameter, β, was varied. There were three distinct regimes. For low values of the control parameter, $0 < \beta < 0.6$, the linking numbers computed were compatible with the Lorenz branched manifold with rotation symmetry. This was

CHAPTER 5: THREE-DIMENSIONAL PROJECTIONS

expected since the Equations (3.27) reduce to the Lorenz equations as $\beta \to 0$. In the intermediate range, $0.6 < \beta < 5.4$, the linking numbers were found to decrease through integer steps and the table was not compatible with any branched manifold. For higher values, $5.4 < \beta < 8$, the linking numbers were the negative of those found for the small β regime. As the linking numbers decrease through integer steps the attractor undergoes self-intersections and the uniqueness theorem [27] is violated in the projection (the uniqueness theorem is never violated in the full four-dimensional phase space). This prevents the projection to the (X, Y, Z) subspace from providing an embedding of the attractor.

The (X, Y, U) projection was found to exhibit entirely different behavior. The table of linking numbers for this projection was compatible with the Lorenz branched manifold with inversion symmetry. Since the compatibility persisted over the range of control parameter values, $0 < \beta < 8$, no self-intersections were found for this projection. We will investigate this further in Section 5.2 by considering higher period orbits beyond the six listed in Table 5.2.

5.2 Computation of linking numbers for pairs of orbits

The first step in computing the linking numbers is to find surrogates for pairs of orbits by the method of close returns. As an example we will consider the period two orbit LR and the period five orbit $LLRLR$.

Surrogates were found for each of these orbits, in the full four-dimensional phase space (X, Y, Z, U), as β was increased incrementally, in steps of 0.01, starting from $\beta = 0$ and ending at $\beta = 8$. Surrogates for the orbit LR were obtained for 795

CHAPTER 5: THREE-DIMENSIONAL PROJECTIONS

Table 5.3: Linking numbers for the period five orbits with all lower period orbits in the rotation-symmetric Lorenz branched manifold

	LR	LLR	LRR	LLLR	LRRR	LLRR
LLLLR	1	2	1	3	1	2
LLLRR	2	3	2	3	2	3
LLRRR	2	2	3	2	3	3
LLRLR	2	3	2	3	2	3
LRRLR	2	2	3	2	3	4
LRRRR	1	1	2	1	3	2

Table 5.4: Linking numbers for the period five orbits with all lower period orbits in the inversion-symmetric Lorenz branched manifold

	LR	LLR	LRR	LLLR	LRRR	LLRR
LLLLR	0	−1	0	−2	0	−1
LLLRR	0	−1	1	−2	1	0
LLRRR	0	−1	1	−1	2	0
LLRLR	0	−1	0	−1	0	−1
LRRLR	0	0	1	0	1	1
LRRRR	0	0	1	0	2	1

values of β and surrogates for the orbit $LLRLR$ were found for 476 values of β. For the values of β where surrogates for both orbits were found the linking number was computed in the (X, Y, Z) and (X, Y, U) subspaces. To calculate the linking number for any value of the control parameter in the range $0 < \beta < 8$ we can use the method described in Section 4.4 to produce surrogate orbits for the desired value of β. The $Y - U$ projection of these surrogate UPO's is shown for two values of the control

CHAPTER 5: THREE-DIMENSIONAL PROJECTIONS

parameter, $\beta = 0.8$ in Figure 5.1 and $\beta = 4.83$ in Figure 5.2.
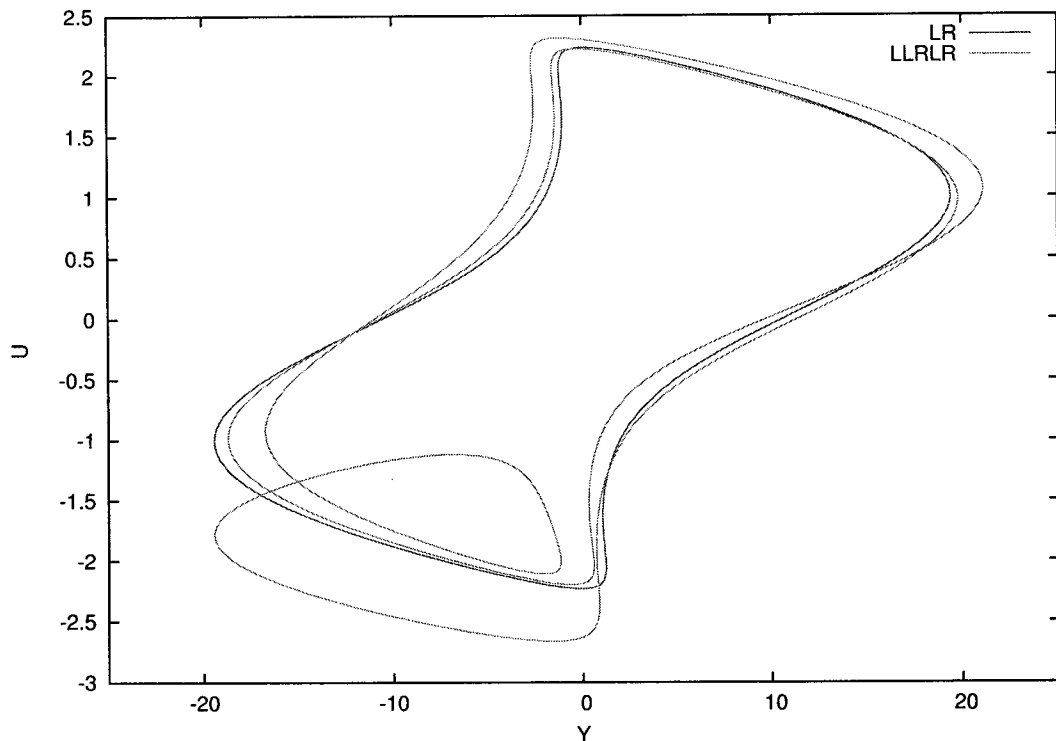
Figure 5.1: The Y - U projection of the two UPO's LR and $LLRLR$ for $\beta = 0.8$. Their linking number is $+1$ for this value of the control parameter, β.

In the (X, Y, Z) projection the linking numbers found agreed with the behavior reported by Moroz *et al* [16]. The linking number as a function of β is shown in Figure 5.3a. For $\beta = 0$ the linking number is $+2$, as expected from Lorenz branched manifold with rotation symmetry, Table 5.3, since this is the limit that reduces to the Lorenz equations. As β is increased we can see the linking number decrease through integer steps until finally assuming the negative of the values for $\beta = 0$. Self-intersections occur each time the linking number changes in this projection.

In the (X, Y, U) projection the linking number was 0 for the control parameter range, $1.5 < \beta < 8$, which is compatible with Lorenz manifold with inversion sym-

CHAPTER 5: THREE-DIMENSIONAL PROJECTIONS
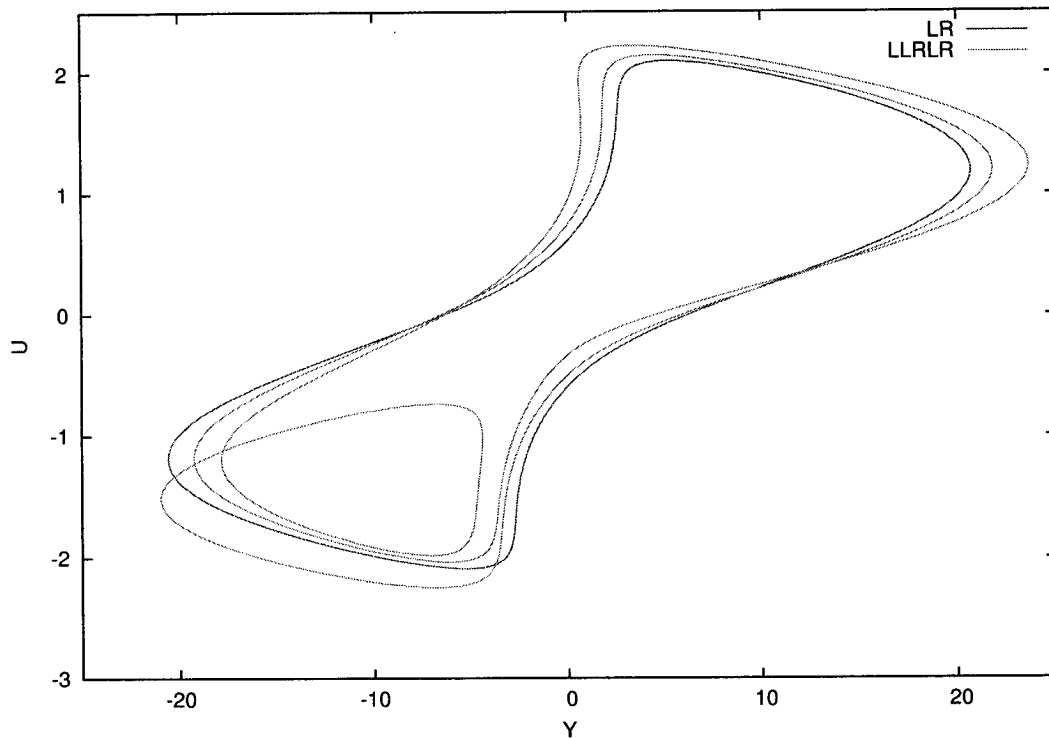
Figure 5.2: The Y - U projection of the two UPO's LR and $LLRLR$ for $\beta = 4.83$. Their linking number is zero for this value of the control parameter, β.

metry, Table 5.4. However, for $0 < \beta < 1.5$ the linking number in this projection becomes zero. Figure 5.3b shows a single step down that indicates self-intersections also occur in this projection as for the (X, Y, Z) projection. If this is the case then the (X, Y, U) projection fails to provide an embedding. To check for this the minimum distance between the orbits was computed as a function of β. This was done for each of the projections as well as the full four-dimensional phase space. Plotting this minimum distance as a function of β, Figure 5.4, we can see a sharp downward spike each time self-intersections occur in a projection. Each time this minimum distance tends toward zero the linking number for pairs of orbits changes. In the (X, Y, U)

CHAPTER 5: THREE-DIMENSIONAL PROJECTIONS

projection there is a single minimum in the minimum distance that corresponds to the change in linking number near $\beta = 1.5$, seen in Figure 5.3b. As the linking number changes the attractor must undergo self-intersection and the uniqueness principle is violated in the (X, Y, U) projection. This confirms that there are some values of β for which this projection is not an embedding. For $\beta > 1.5$ this projection does provide an embedding that is consistent with the Lorenz branched manifold with inversion symmetry but for $\beta < 1.5$ an embedding no longer exists. Figure 5.4 also shows the minimum distance between the two orbits in the original four-dimensional space before being projected. This minimum distance never reaches zero because the uniqueness principle guarantees that no self-intersections occur.

(a) The (X, Y, Z) projection

(b) The (X, Y, U) projection
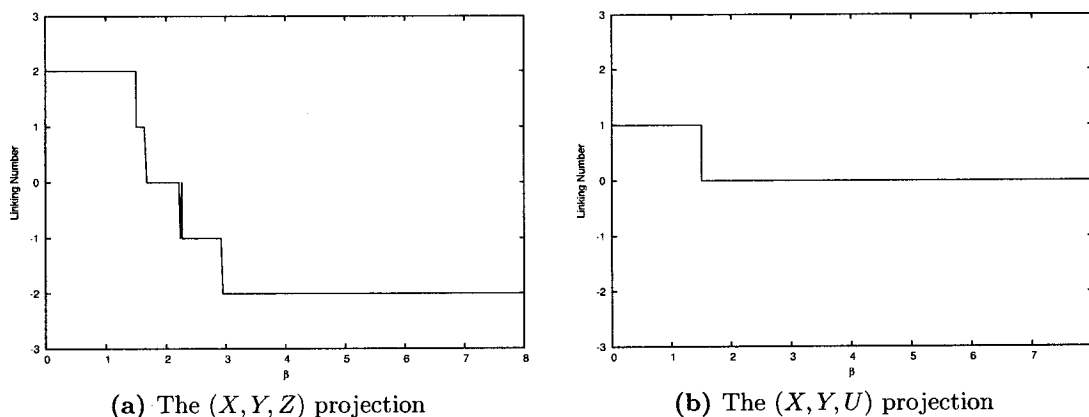
Figure 5.3: Linking numbers for the pair of surrogate unstable periodic orbits LR and $LLRLR$

5.3 Summary

It was originally thought that the two simple projections showed entirely different behavior. In the (X, Y, Z) projection the attractor undergoes self-intersections and the projection fails to provide an embedding. The (X, Y, U) projection was thought

CHAPTER 5: THREE-DIMENSIONAL PROJECTIONS
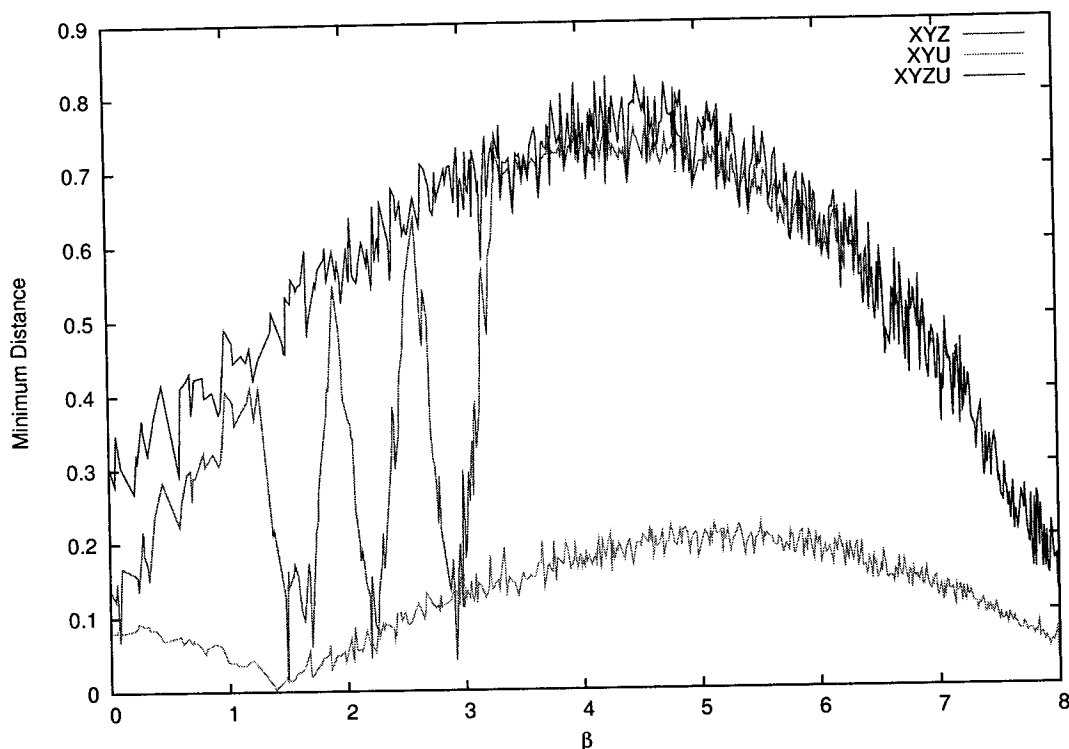
Figure 5.4: The minimum distance between the orbits LR and $LLRLR$ as a function of β. The minimum distance is shown for the two simplest projections, (X, Y, Z) and (X, Y, U) as well as the full four dimensional phase space.

to provide an embedding for all values of the control parameter in the range $0 < \beta < 8$. We have shown here that the (X, Y, U) projection is not dissimilar from the (X, Y, Z) projection since the table of linking numbers also change as β is varied. This projection is not an embedding for $\beta < 1.6$. Neither of the simple projections provide embeddings for all values of β but there is, in principle, a three-dimensional manifold in which the attractor can be embedded. Alternative approaches to the simple projection techniques will explored in Chapter 9 to find an embedding of this attractor.

CHAPTER 5: THREE-DIMENSIONAL PROJECTIONS

Chapter 6: The Missing Orbits and Homoclinic Explosions

6.1 Homoclinic Orbits

As the control parameter β is varied it may be the case that the stable manifold of the origin includes the unstable manifold of the origin. When this situation occurs we label the control parameter as $\beta = \beta'$ and there is a homoclinic orbit associated with the unstable saddle point at the origin. Any trajectory that starts on the unstable manifold of the origin will approach the origin as $t \to \pm\infty$. The bifurcation associated with a homoclinic orbit is known as a homoclinic explosion and will be discussed in the next section.

6.2 Homoclinic Explosions

In this section we will follow the approach used by Sparrow [28] for the Lorenz system and apply those methods to our strange attractor. We first attempt to detect if there are any homoclinic explosions in the parameter range $0 \leq \beta \leq 8.0$. If any homoclinic explosions do occur there will be a change in behavior of the unstable manifold of the origin as the control parameter is varied.

There are two types of homoclinic explosions and each type can either add or remove orbits from a strange attractor [28].

We will consider one branch of the unstable manifold of the origin which we calculate numerically. This is done by choosing an initial condition very close to the origin but displaced in the direction of the eigenvector associated with the positive

eigenvalue of the linearized flow. The X-Z projection of a trajectory computed by this method is shown in Figure 6.1 for $\beta = 0$. The trajectory was computed until it had reached seven consecutive maxima in the Z variable. This will allow the detection of homoclinic explosions associated with orbits up to period six.
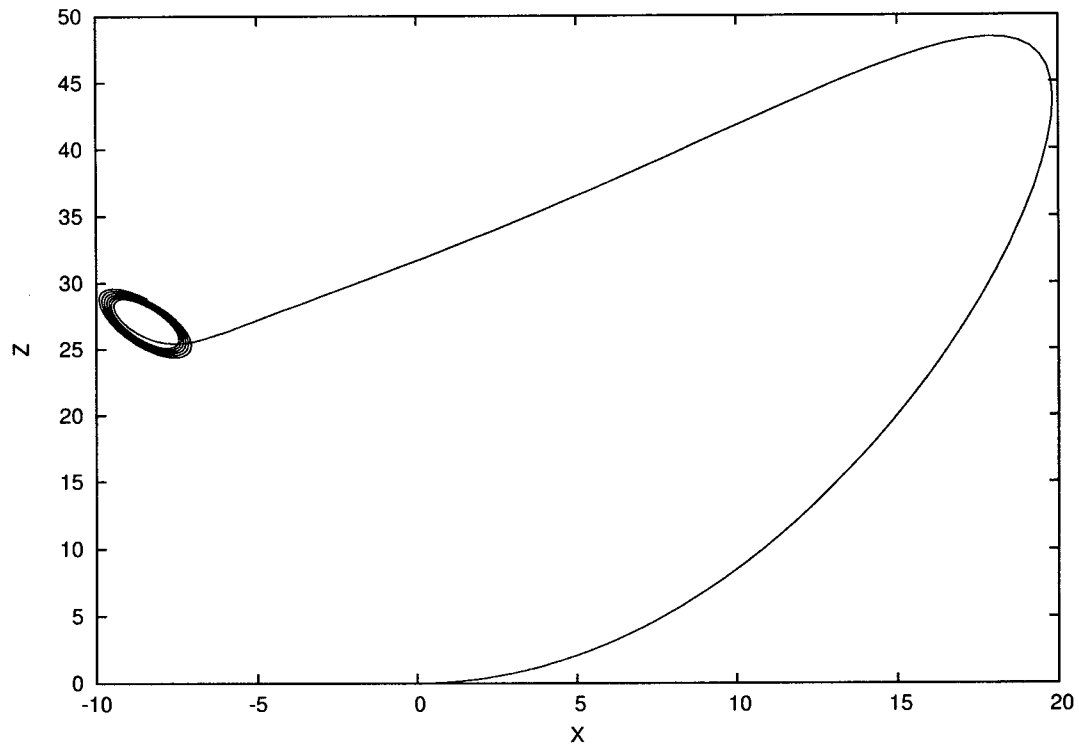
Figure 6.1: The X-Z projection of the right-hand branch of the unstable manifold of the origin for $\beta = 0$

As β is increased from a value below β' there will be a change in behavior of the unstable manifold of the origin. For β close to β' we can describe the unstable manifold of the origin in terms of a symbolic sequence introduced by Sparrow. This sequence, $k(\beta)$, is in terms of two symbols, T and S, shown in Figure 6.2. Each symbol represents a tube that surrounds the unstable manifold of the origin from the point where it leaves a small volume around the origin until it re-enters the volume

CHAPTER 6: THE MISSING ORBITS AND HOMOCLINIC EXPLOSIONS

for the first time. T corresponds to the right-hand branch, which leaves the small

volume in the direction associated with the positive eigenvalue of the linearized flow.

S is the corresponding tube for the left-hand branch. The sequence, $k(\beta)$ will change

as β increases from $\beta < \beta'$ to $\beta > \beta'$.
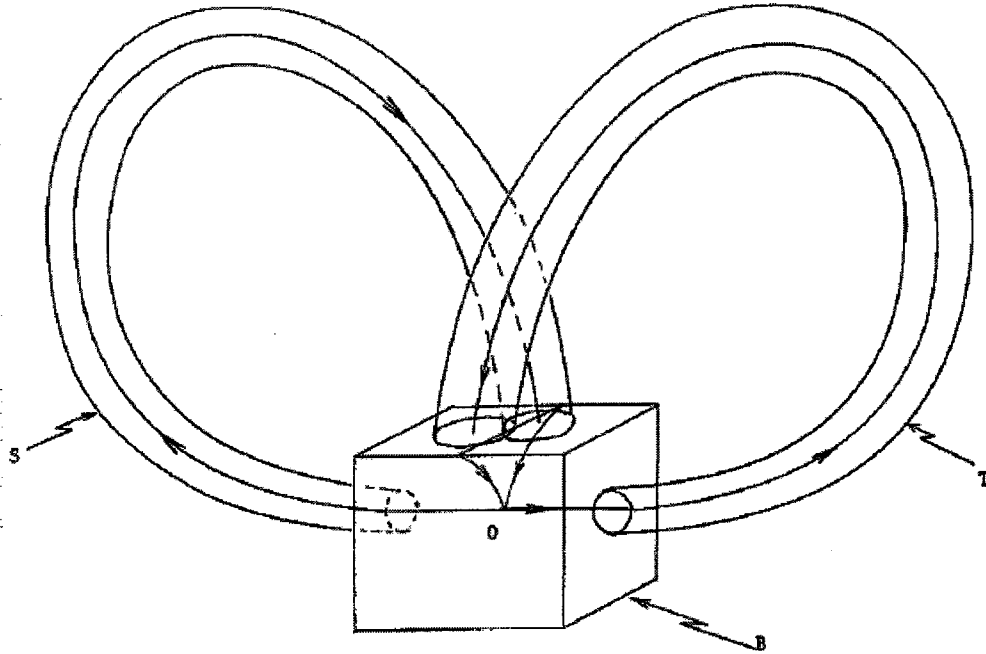
Figure 6.2: The unstable manifold of the origin in terms of a symbolic sequence. Image taken from [28].

There are two different types of homoclinic explosion. Each type, (a) and (b), produces a distinct change in $k(\beta)$. For type (a) homoclinic explosions the change is

$$\text{Type (a):} \quad \text{TTTTTT.....} \rightleftharpoons \text{TSSSSS.....} \tag{6.1}$$

CHAPTER 6: THE MISSING ORBITS AND HOMOCLINIC EXPLOSIONS

and for type (b) the change is .

$$\text{Type (b):} \quad \text{T TS TS TS..... } \rightleftharpoons \text{ TS TS TS TS.....} \qquad (6.2)$$

If $k(\beta)$ changes in the forward direction in either (6.1) or (6.2) a strange invariant set is produced. A change in the reverse direction removes a strange invariant set [28].

6.2.1 Return Maps for the RL^3-Homoclinic Explosion

We can show that a strange invariant set exists on only one side of the homoclinic explosion by considering numerically computed return maps. Here we will consider the RL^3 explosion since this is the lowest period found in the parameter range under consideration. Figure 6.3 shows how the unstable manifold of the origin changes as β is increased from 5.02792 to 5.02793. Between these two control parameter values the RL^3 homoclinic orbit exists.

(a) Y-Z projection for $\beta = 5.02792$ (b) Y-Z projection for $\beta = 5.02793$
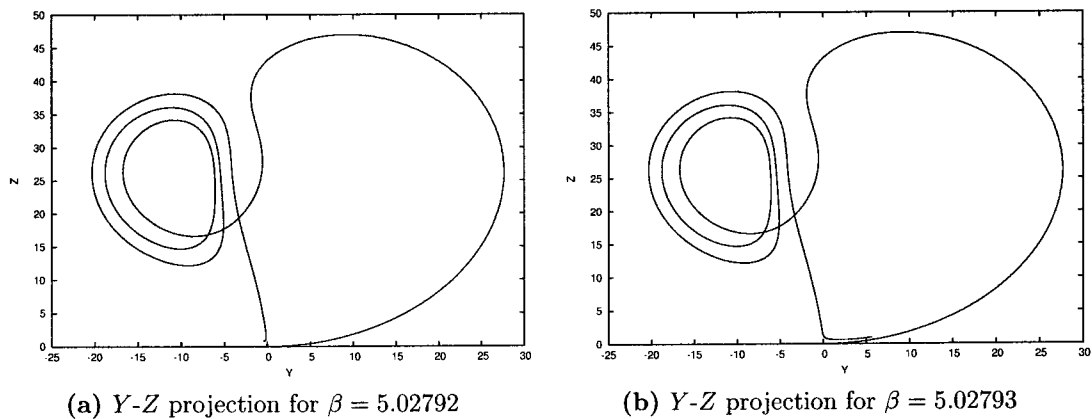
Figure 6.3: Change in behavior of the unstable manifold of the origin

We will compute return maps for trajectories that lie close to the unstable manifold

CHAPTER 6: THE MISSING ORBITS AND HOMOCLINIC EXPLOSIONS

of the origin by choosing an initial condition near to the origin but displaced in the Z-direction. Such a trajectory first tends toward the origin and then continues in the direction of the eigenvector, $\vec{e}$, associated with the positive eigenvalue of the linearized flow. When the trajectory returns close to the origin and crosses the initial Z value this final position is recorded and plotted against the initial position. The positions recorded are along the direction of the eigenvector $\vec{e}$. For $\beta = 5.02793$ this normalized eigenvector is $(0.439, 0.898, 0, 0.028)$. The coordinate being recorded, which we denote e, is given by,

$$e = 0.439X + 0.898Y + 0.028U \qquad (6.3)$$

We denote initial the position along this direction as e_n and the first return as e_{n+1}. A series of initial positions along this direction were used to construct the return maps shown in Figures 6.4 and 6.5.

The return map shown in Figure 6.5 shows that trajectories will simply escape from the region that is close to the homoclinic orbit and not return close to the origin. However, for the return map shown in Figure 6.4 trajectories can remain within a region close to the homoclinic orbit forever. That is, as the control parameter β is increased above 5.0279 a complete RL^3 invariant set is removed from the strange attractor. The simplest members of this set are LR^3, RL^3, LR^3RL^3, etc.

6.2.2 Example: The RL^5-Homoclinic Explosion

For $\beta = 0$ the sequence describing the unstable manifold of the origin, up to the seventh symbol, is RL^6. This can be seen from Figure 6.1. As β is increased these

CHAPTER 6: THE MISSING ORBITS AND HOMOCLINIC EXPLOSIONS
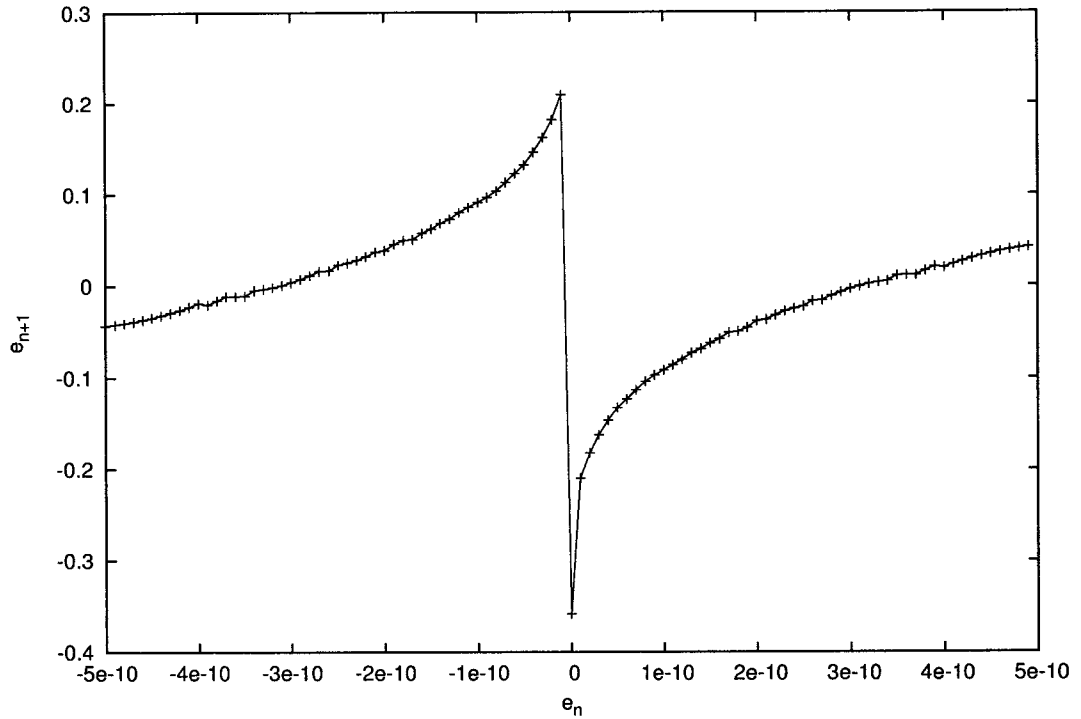
Figure 6.4: Return map for $\beta = 5.0279$

seven symbols remain the same until $\beta = 2.75$. For this value of β the sequence has changed to RL^5R. Figures 6.6a and 6.6b show the change in the unstable manifold of the origin near $\beta = 2.75$. The nature of this change suggests the existence of a RL^5-homoclinic orbit somewhere in the range $2.74 < \beta < 2.75$. Equations (6.1) and (6.2) show that the change in the first two symbols of $k(\beta)$ is identical for type (a) and (b). We need to follow the unstable manifold of the origin around the tubes at least three times to distinguish between the two types. For a RL^5-homoclinic explosion the two possible changes in the symbolic sequence can be found by substituting $T=RL^5$ and $S=LR^5$ into equations (6.1) and (6.2). This means that we need to find $k(\beta)$, in terms of L and R, up to the first thirteen symbols. Unfortunately it is not practical

CHAPTER 6: THE MISSING ORBITS AND HOMOCLINIC EXPLOSIONS
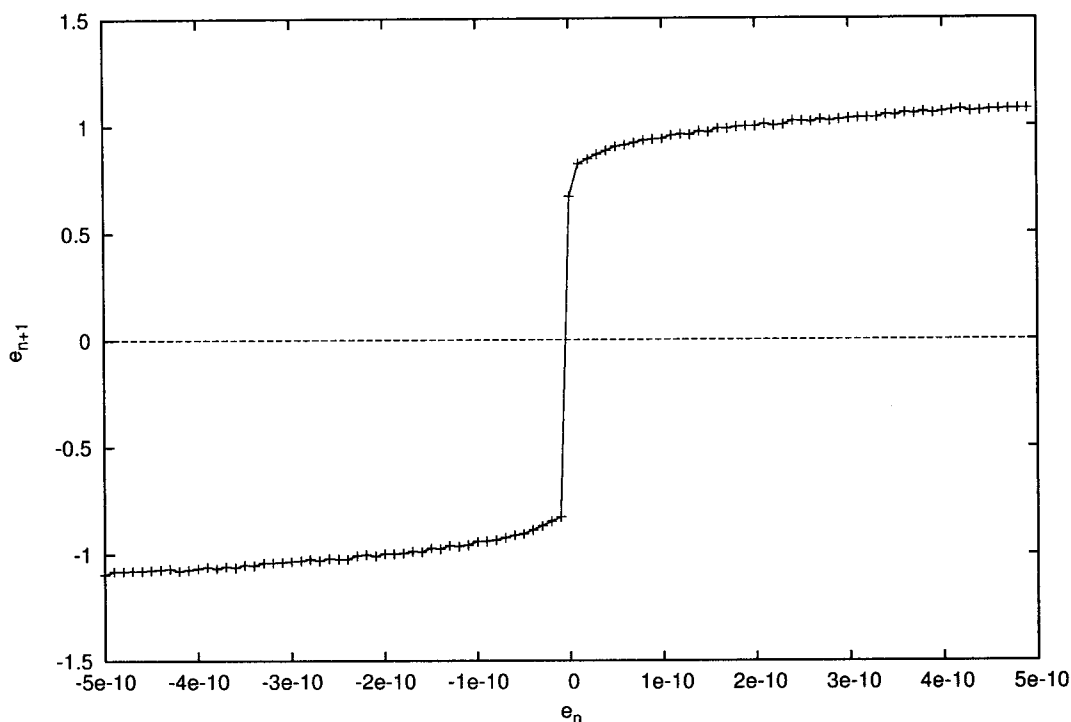
Figure 6.5: Return map for $\beta = 5.04$

to follow $k(\beta)$ for much more than seven symbols and an alternative method must be used.

To check whether a type (a) or (b) homoclinic explosion occurs for $2.74 < \beta < 2.75$ we consider two trajectories for $\beta < \beta'$ and $\beta > \beta'$ with β very close to β'. The first trajectory is along the right-hand branch of the unstable manifold of the origin. This is found using the same method that was used to produce Figure 6.1. We only need to consider the right-hand branch since the left-hand branch is just the symmetric image (found by replacing all the R's with L's and vice versa). The second trajectory under consideration is started very close to the first but displaced a small distance along the positive Z-axis. We also consider a small box around the origin enclosing

CHAPTER 6: THE MISSING ORBITS AND HOMOCLINIC EXPLOSIONS

(a) *X-Z* projection for $\beta = 2.74$ (b) *X-Z* projection for $\beta = 2.75$
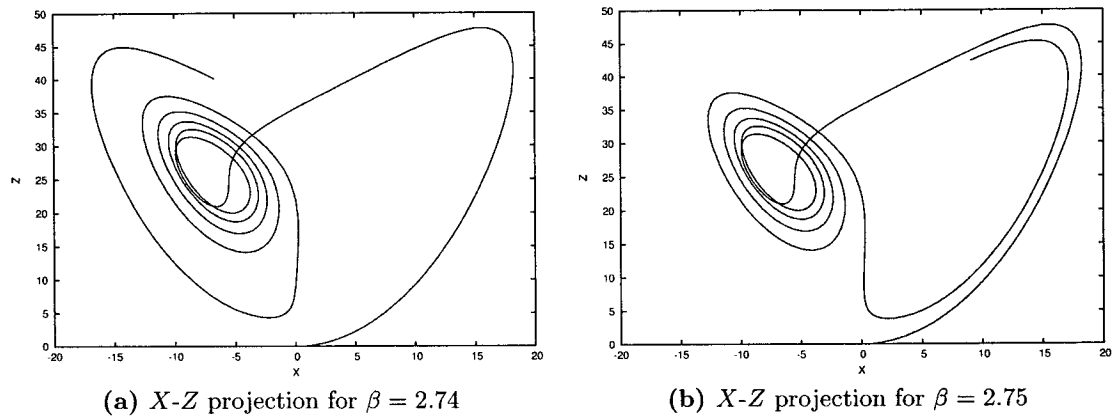
Figure 6.6: Change in behavior of the unstable manifold of the origin

the initial positions of both trajectories. Since the stable manifold of the origin looks like a plane near the origin it divides this small box into two halves. The positions, relative to the stable manifold of the origin, where these trajectories first leave and re-enter the box depend on whether we have a type (a) or (b) homoclinic explosion at $\beta = \beta'$ where $2.74 < \beta' < 2.75$. Both trajectories start to the right of the stable manifold of the origin $(X > 0)$ and may return to the top face of the box to the left or right of the stable manifold of the origin.

For the type (a) homoclinic explosion the unstable manifold of the origin will intersect the top face of the box on different sides of the stable manifold of the origin for β above and below β'. However, the second trajectory will re-enter the box on the right-hand side, provided that β is close enough to β'.

For the type (b) homoclinic explosion the unstable manifold of the origin will again re-enter the box on different sides of the stable manifold of the origin for β above and below β'. The second trajectory will re-enter the box on the left-hand

CHAPTER 6: THE MISSING ORBITS AND HOMOCLINIC EXPLOSIONS
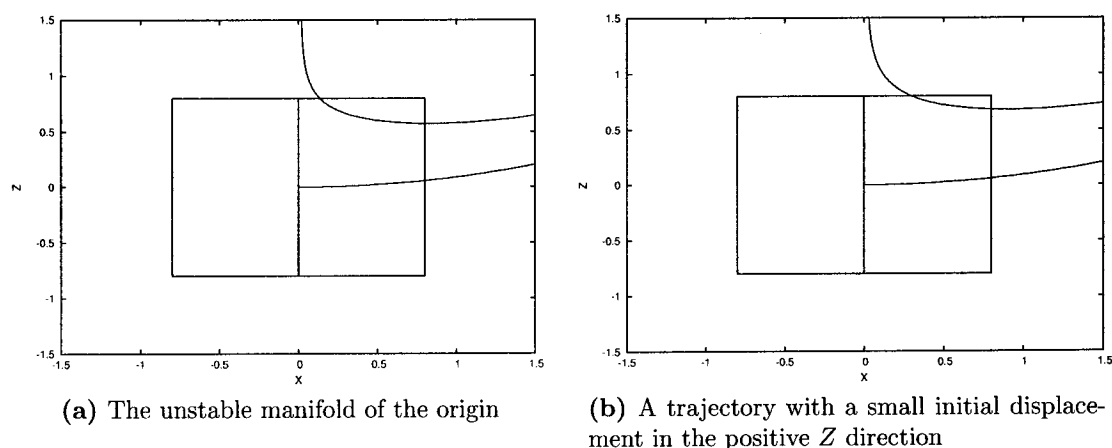
This is not unexpected since type (b) explosions can only occur for values of the control parameters that produce period doubling windows. For the classic choice of the Lorenz parameters with $\Lambda = 3.2$ and $0 < \beta < 8.0$ there are no period doubling windows present [29]. Furthermore, this explosion is proceeding in the direction that removes an invariant set. As β is increased, $k(\beta)$ changes in the reverse direction as shown in equation (6.1)

$$TSSSSS..... \rightarrow TTTTTT.....$$

The result is that the period six UPO's, RL^5, and it's symmetric image, LR^5, are removed from the strange attractor by the homoclinic explosion at $\beta \approx 2.75$.

6.2.3 Homoclinic Explosions in the Range $0 < \beta < 8.0$

Each homoclinic explosion, associated with a homoclinic orbit up to period six, may be found by following changes in $k(\beta)$ if the sequence is known up to the seventh symbol. The homoclinic explosions that occur for $0 < \beta < 8.0$ are shown in Table 6.1. All of these are type (a) homoclinic explosions.

By analyzing each change in $k(\beta)$ in the same way as Section 6.2.2, it was found that the first four explosions listed in Table 6.1 are proceeding in the direction that removes a strange invariant set. The subsequent four explosions are proceeding in the direction that produces a strange invariant set. This means that UPO's, with period of six or less, are removed from the strange attractor for $\beta < 6.98$ and added back to the strange attractor for $\beta \geq 6.98$.

Table 6.1: A list of numerically computed values of $k(\beta)$

β	$k(\beta)$	Explosion
0	RL^6	
		RL^5
2.75	RL^5R	
		RL^4
3.52	RL^4RL	
		RL^4R
4.60	RL^4RR	
		RL^3
5.03	RL^3RL^2	
		RL^3
6.98	RL^4R^2	
		RL^4R
7.18	RL^4RL	
		RL^4
7.58	RL^5R	
		RL^5
7.76	RL^6	

6.2.4 The RL^3-Homoclinic Explosion

We wish to focus on the RL^3-homoclinic explosion for two reasons. Firstly, it was this periodic orbit that was found to "disappear" for a range of control parameter values in the strange attractor. Secondly, the topological period of this homoclinic explosion is low enough to be verified against the expected behavior given by Equation (6.1).

We noted in Section 4.3 that not all surrogate UPO's could be found by the method of close returns. More specifically, certain low period surrogates could only be found for a range of the control parameter, β. The lowest period orbits to exhibit this behavior were the non-symmetric period four orbits, LR^3 and RL^3. Surrogates for these particular orbits could only be found in the range $0 < \beta < 4.6$ and $7.22 <$

CHAPTER 6: THE MISSING ORBITS AND HOMOCLINIC EXPLOSIONS

$\beta < 8.0$. Table 6.1 shows that there is a RL^3-homoclinic explosion at $\beta \approx 5.03$ that removes a strange invariant set. There is another RL^3-homoclinic explosion at $\beta \approx 6.98$ that produces a strange invariant set. It is now clear why no surrogates for the non-symmetric period four orbits could be found in the range $5.03 < \beta < 6.98$. The first RL^3-homoclinic explosion removes the RL^3 UPO's from the strange attractor (and it's symmetric image $\overline{RL^3}$ likewise). The second RL^3-homoclinic explosion re-introduces the non-symmetric period four UPO's into the strange attractor.

We stated in Section 6.2.3 that all the homoclinic explosions listed in Table 6.1 are type (a). This was confirmed in the same way as for the RL^5-homoclinic explosion in Section 6.2.2.

The change in $k(\beta)$ is identical for type (a) and (b) RL^3-homoclinic explosions if only seven symbols are used. To distinguish between the two types using the symbolic sequence requires a description with nine symbols. The symbolic sequence, $k(\beta)$, was calculated numerically for $\beta = 5.02793$ and $\beta = 5.02794$, up to nine symbols. The two sequences are given below

$$\beta = 5.02793 \qquad\qquad k(\beta) = RL^4R^3L$$

$$\beta = 5.02794 \qquad\qquad k(\beta) = RL^3RL^3R$$

To verify that the RL^3-homoclinic explosion is type (a) we make the following substitutions into equation (6.1), $T=RL^3$ and $S=LR^3$. This substitution results in a

---

CHAPTER 6: THE MISSING ORBITS AND HOMOCLINIC EXPLOSIONS

change in the first nine symbols of $k(\beta)$ given by

$$RL^3RL^3R \rightleftharpoons RL^3LR^3L$$

which confirms that the first RL^3-homoclinic explosion is type (a) proceeding in the direction that removes a strange invariant set.

6.3 Remarks

In fact, there is no need to restrict this analysis to the range $0 < \beta < 8.0$. Applying the same approach described in Section 6.2 we find a homoclinic explosion for $\beta \approx 9.34$ that is associated with the two period one orbits L and R. This is once again a type (a) homoclinic explosion but it is proceeding in the direction that removes a strange invariant set. This orbit is not present in the original strange attractor for $\beta = 0$ but is created in a Hopf bifurcation at $\beta \approx 6.4$.

The sequence of homoclinic explosions observed in the strange attractor generated by Equations (3.27) is analogous to the sequence observed in the Lorenz attractor. As β is increased from zero these bifurcations remove periodic orbits from the strange attractor. As the control parameter is increased further these orbits are recreated, in the reverse order, by homoclinic explosions. This sequence is shown in Table 6.1 for UPO's up to period six.

Reproduced with permission of the copyright owner. Further reproduction prohibited without permission.

Chapter 7: A Higher Dimensional Linking Integral

A higher dimensional linking integral has recently been introduced by Shonkwiler and Vela-Vick [1]. Their theorem gives an explicit linking integral for "visible hypersurfaces". The term visible means that there is some point from which all rays intersect a manifold, at most, one time. As stated previously, the UPO's in our strange attractor, in $\mathbb{R}^4$, lie on some lower dimensional manifold, since $D_L < 3$. By treating this manifold as a hypersurface, in the ambient four-dimensional space, we can apply the higher dimensional linking integral provided that we can show this manifold is visible.

7.1 Finding a visible point

In order to show whether the strange attractor is visible from a particular point it is useful to calculate the minimum distance from each point along the ray to the strange attractor. A plot of this minimum distance, as a function of distance along the ray, will show a single minimum if it intersects the strange attractor only once. Such a plot is shown in Figure 7.1 for six rays originating from the point $(0, 0, 200, 0)$.

For the point chosen in Figure 7.1, the strange attractor was shown to be visible for 1000 rays that spanned the diameter of the attractor. Each ray contained 500 points and the minimum distance was calculated from 400,000 sampled points on the strange attractor. The plot for each individual ray showed at most, one minimum, indicating that no more than one intersection took place. This result shows that the
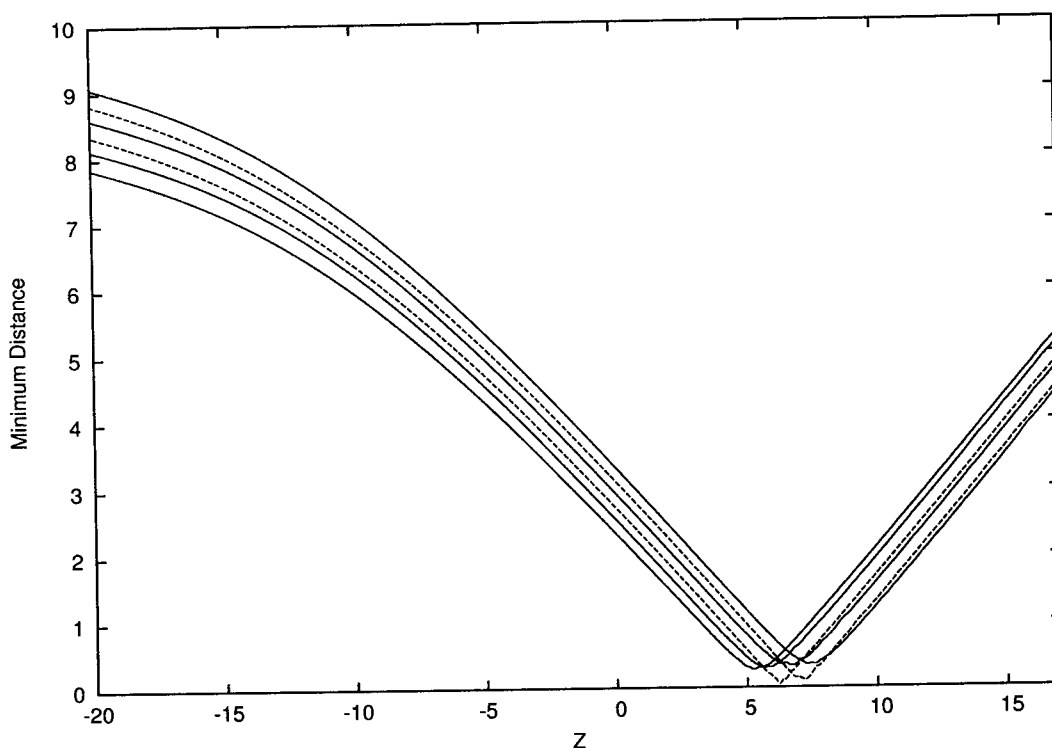
Figure 7.1: The minimum distance between rays originating from $(0, 0, 200, 0)$ and 400,000 sampled points on the strange attractor, as a function of the Z-coordinate, for $\beta = 0$.

strange attractor is visible from the point $(0, 0, 200, 0)$.

7.2 Computation of the linking number

The linking integral for visible hypersurfaces derived in [1] is

$$Lk(K, L) = \frac{1}{\mathrm{vol}S^n} \int_{K \times L} \frac{\Omega_{k,l}(\alpha)}{|x|^{k+1}|y|^{l+1}\sin^n \alpha}[x, dx, y, dy] \qquad (7.1)$$

CHAPTER 7: A HIGHER DIMENSIONAL LINKING INTEGRAL

where K^k and L^l are submanifolds of a visible hypersurface $M^n \subset \mathbb{R}^{n+1}$ with $k + l = n - 1$ and,

$$\Omega_{k,l}(\alpha) = \int_{\theta=\alpha}^{\pi} \sin^k(\theta - \alpha) \sin^l \theta \, d\theta \tag{7.2}$$

Here $\alpha(x,y)$ is the angle between $x \in K$ and $y \in L$ thought of as vectors in $\mathbb{R}^{n+1}$.

$$[x, dx, y, dy] = \det\left(x, \frac{\partial x}{\partial s_1}, ..., \frac{\partial x}{\partial s_k}, y, \frac{\partial y}{\partial t_1}, ..., \frac{\partial y}{\partial t_l}\right) ds \, dt \tag{7.3}$$

For the case of a three-dimensional visible manifold in $\mathbb{R}^4$, each submanifold, K and L, the UPO's, are one-dimensional. The linking integral formula in this case is

$$Lk(K,L) = \frac{1}{2\pi^2} \int_{K \times L} \left(\frac{\Omega_{k,l}(\alpha)}{|x|^2 |y|^2 \sin^3 \alpha}\right) \det\left(x, \frac{\partial x}{\partial s}, y, \frac{\partial y}{\partial t}\right) ds dt \tag{7.4}$$

with

$$\Omega_{k,l}(\alpha) = \int_{\theta=\alpha}^{\pi} \sin(\theta - \alpha) \sin \theta \, d\theta \tag{7.5}$$

Here K and L are the UPO's lying on the visible manifold. These two closed orbits are parametrized by s and t. The angle α is between x and y which are position vectors for points on each of the closed orbits. $\frac{\partial x}{\partial s}$ and $\frac{\partial y}{\partial t}$ are tangent vectors to each of the closed orbits at the points $x(s)$ and $y(t)$.

Using Equation (7.4) the four-dimensional linking integral was computed for UPO's up to period four and these are shown in Table 7.1. The linking number was computed for a range of control parameter values, $0 < \beta < 8$, and the values shown in Table 7.1 are the averages over this range. Although linking numbers are integer val-

---

CHAPTER 7: A HIGHER DIMENSIONAL LINKING INTEGRAL

ued, here they are given to two decimal places to give an indication of the numerical error associated with the computation. By comparison with Table 5.2 we can see that these linking numbers are consistent with the branched manifold for the Lorenz system with inversion symmetry. All linking numbers in this table varied within 0.05 of the nearest integer value for all values of β.

Table 7.1: Averaged linking integral values for UPO's lying on a visible hyper-surface.

	LR	LLR	LRR	$LLLR$	$LRRR$	$LLRR$
LR	-	0.02	-0.01	0.02	-0.01	0.01
LLR	0.02	-	0.04	-0.99	-0.02	-0.97
LRR	-0.01	0.04	-	0.04	0.92	1.00
$LLLR$	0.02	-0.99	0.04	-	-0.04	-1.01
$LRRR$	-0.01	-0.02	0.92	-0.04	-	1.02
$LLRR$	0.01	-0.97	1.00	-1.01	1.02	-

The four-dimensional linking integral was also used to calculate the linking numbers for the period five UPO's. The results were consistent with the values obtained in the (X, Y, U) projection for $\beta > 1.6$ and exhibited a change in sign as the control parameter β was varied. For the visible point found in Section 7.1 the higher dimensional was equivalent to the Gauss linking integral, Equation (2.2), in the (X, Y, U) subspace.

7.3 Summary

In this chapter we have determined the linking numbers for pairs of UPO's, Table 7.1, using a higher dimensional linking integral. This required the determination of a

---

CHAPTER 7: A HIGHER DIMENSIONAL LINKING INTEGRAL

visible point and, for this point, the linking numbers obtained are the same as for the (X, Y, U) projection in Section 5.2. These linking numbers were found to change as the control parameter was increased over the range $0 < \beta < 8$. The results from this chapter, along with chapter 5, motivate an alternative approach to determining the organization of the UPO's through the use of dimensionality reduction techniques. This will be addressed in the next chapter where several algorithms for dimension reduction will be reviewed and compared.

CHAPTER 7: A HIGHER DIMENSIONAL LINKING INTEGRAL

Chapter 8: Review of Dimensionality Reduction Techniques

Dimensionality reduction techniques have been developed to find low dimensional structure within high dimensional data sets. More specifically, for a data set consisting of N vectors, each with D components, the points in the data set may lie on or near to a manifold of dimension d (where $d < D$). Dimensionality reduction algorithms find a d-dimensional representation that best preserves certain geometric properties of the data. The problem of finding lower dimensional structure in a high-dimensional data set is a common problem in many fields of research. In recent years these techniques have become widely used in a variety of fields. This wide variety of examples include molecular modeling [30], gene expression analysis [31], sound source localization [32] and dynamical systems [33].

In this chapter we will review some of the most popular dimensionality reduction techniques. We begin with the classical methods of the field that are essentially linear in nature. In section 8.2 we give an overview of three different nonlinear techniques. These are isometric feature mapping (Isomap) [34], locally linear embedding (LLE) [35, 36] and Laplacian eigenmaps [37]. We compare each of these nonlinear methods in section 8.3 by considering both the effectiveness and the efficiency of the algorithms.

8.1 Classical Methods

The classical methods in this field include principal component analysis (PCA) [38], linear discriminant analysis (LDA) [39, 40], independent component analysis (ICA)

[41, 42] and metric multi-dimensional scaling (MDS) [43]. These techniques are linear in nature and nonlinear structure within a data set is essentially invisible to these methods. To demonstrate this we consider one of the most commonly used methods, PCA, as applied to a nonlinear manifold.

8.1.1 Principal Component Analysis (PCA)

PCA [38] is a transformation that takes a set of N data points $\mathbf{x}_i \in \mathbb{R}^D$ and projects them to a set of points $\mathbf{y}_i \in \mathbb{R}^d$, with maximal variance in the subspace. If the input data set is centered on the origin (which can be obtained by subtracting the mean for each direction from the components of every vector, $\mathbf{x}_i$) then the basis vectors of the subspace can be determined by finding the eigenvectors of the covariance matrix defined by

$$C_{ij} = \frac{1}{N} \sum_{k=1}^{D} x_{ik} x_{jk} \tag{8.1}$$

where x_{ij} denotes the jth component of $\mathbf{x}_i$. Denoting this $N \times D$ data matrix by $\mathbf{X}$ we have

$$\mathbf{C} = \left(\frac{1}{N}\right) \mathbf{X}\mathbf{X}^\top \tag{8.2}$$

The output data set, $\mathbf{y}_i$, is obtained from the eigenvectors of $\mathbf{C}$ corresponding to the d largest eigenvalues.

Applying PCA to the S-shaped manifold demonstrates how the algorithm is incapable of detecting the nonlinear structure. Figure 8.1 shows how regions that are

CHAPTER 8: REVIEW OF DIMENSIONALITY REDUCTION TECHNIQUES

separated on the manifold are brought closer together and overlap in the lower dimensional projected subspace.

(a) S-Curve   (b) PCA   (c) MDS
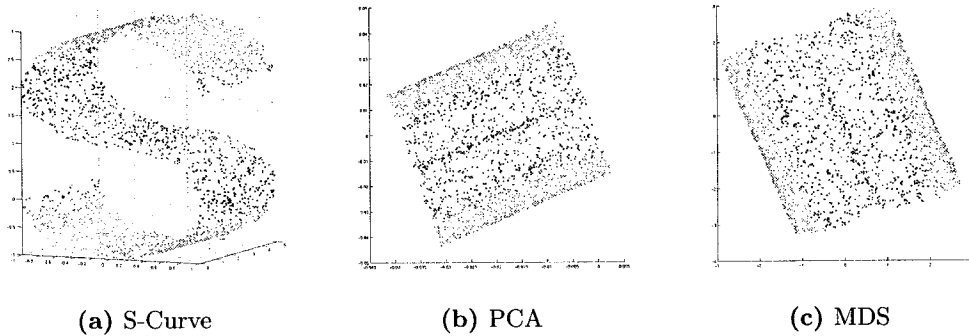
Figure 8.1: PCA and MDS applied to 2000 points sampled from the S-shaped manifold. Overlapping of the data points occurs near edges of the data set in two dimensions as the linear nature of these algorithms fail to preserve the geometry of the underlying manifold.

8.1.2 Metric Multidimensional Scaling (MDS)

MDS [13] is a dimensionality reduction technique that aims to preserve pairwise distances between data points. We are giving an overview of this technique not only because it is commonly used as a dimensionality reduction tool in its own right but also due to the fact that it is an integral component of other nonlinear algorithms such as Isomap.

Here we will be reviewing *classical* MDS which means these pairwise distances are Euclidean. The classical MDS algorithm takes as input a set of N pairwise distances and generates an output configuration in d-dimensional Euclidean space. There are four main steps to the algorithm.

1. Calculate the $N \times N$ matrix of squared distances, Δ.

CHAPTER 8: REVIEW OF DIMENSIONALITY REDUCTION TECHNIQUES

2. Apply the double centering matrix $-\frac{1}{2}\mathbf{C}\Delta\mathbf{C} = \mathbf{B}$, where $\mathbf{C} = \mathbf{I} - \left(\frac{1}{N}\right)\mathbf{1} \cdot \mathbf{1}^{\mathsf{T}}$

3. Compute the d largest eigenvalues, $\lambda_1...\lambda_d$ and the corresponding eigenvectors, $\mathbf{e}_1...\mathbf{e}_d$, of $\mathbf{B}$

4. Find a d-dimensional configuration from $\mathbf{X} = \Lambda^{1/2}\mathbf{E}$, where, Λ is the diagonal matrix of the d eigenvalues of $\mathbf{B}$ and $\mathbf{E}$ is the matrix of the d eigenvectors of $\mathbf{B}$.

The result of applying MDS to 2000 points sampled from the S-shaped manifold is shown in Figure 8.1. The main difference between MDS and PCA is that MDS only required the pairwise distances as input while PCA performs a singular valued decomposition on the covariance matrix which is defined in terms of the vectors, $\mathbf{x}_i \in \mathbb{R}^D$.

All of the classical techniques are closely related and give similar results to PCA when applied to data lying on a nonlinear manifold. This highlights the need for nonlinear techniques and in recent years a plethora of methods have been developed. Some of these build on the linear methods, such as isometric feature mapping (Isomap) [44], which is an extension of classical multidimensional scaling [43], whilst others adopt an entirely new approach. Some of the more popular techniques include the Isomap algorithm [44]; locally linear embedding [36]; Laplacian eigenmaps [37] and diffusion maps [45]. They were developed for manifold learning, in the machine learning community, with applications such as facial recognition and handwritten character recognition.

CHAPTER 8: REVIEW OF DIMENSIONALITY REDUCTION TECHNIQUES

8.2   Nonlinear Methods

8.2.1   Isometric Feature Mapping (Isomap)

Isomap [34] is an extension of MDS that uses approximations of geodesics rather than the Euclidean distances that are used in classical MDS. The approximate geodesics are calculated from the shortest paths between points in a neighborhood graph. The Isomap algorithm aims to preserve pairwise geodesic distances over the manifold. There are three main steps

1. Construct a neighborhood graph

2. Compute shortest paths

3. Construct a d-dimensional embedding

In the first step nearest neighbors are assigned to each data point. This is based on Euclidean distances $d_{ij}^{(X)}$ between points in the D dimensional input space. One common method is to choose the K nearest neighbors based on the distance $d_{ij}^{(X)}$. Once neighbors have been assigned to each data point a neighborhood graph is constructed. This is a weighted graph where the weights of the edges for neighboring points are equal to $d_{ij}^{(X)}$.

In the second step, shortest distances are computed on the weighted graph for all of the data points x_i. These distances are used to approximate the geodesic distances between the data points over a submanifold. The shortest paths can be calculated using methods such as Dijkstra's algorithm [46] or Floyd's algorithm [47].

CHAPTER 8:   REVIEW OF DIMENSIONALITY REDUCTION TECHNIQUES

The final step is to use the shortest path distances as inputs to the MDS algorithm, Section 8.1.2. This results in a d-dimensional representation of the data set that best preserves the approximate geodesic distances.

8.2.2 Locally Linear Embedding (LLE)

In LLE [35, 36] it is assumed that a data set in a D-dimensional space lie on a manifold of lower dimension, d, that is locally linear. Each data point is characterized by a set of weights that best reconstruct that point through a linear combination of its neighbors. The key idea is that these reconstruction weights depend locally on the geometry of the manifold and the same weights are used to construct a d-dimensional embedding of the data set. The LLE algorithm has three main steps

1. Assign neighbors to each data point in the original data set.

2. Compute the weights that best linearly reconstruct each data point from its neighbors.

3. Find the vectors in the low-dimensional space by fixing the weights to be those found in step 2 and minimizing the cost function.

The LLE algorithm will be described in detail in Section 9.1.

8.2.3 Laplacian Eigenmaps

The Laplacian eigenmap method [48] is similar to LLE but aims to preserve proximity relations rather than reconstruction weights. The first step is the same as for Isomap or LLE and involves assigning K nearest neighbors to each data point. As

CHAPTER 8: REVIEW OF DIMENSIONALITY REDUCTION TECHNIQUES

with Isomap, an undirected graph is generated with N nodes representing the input data points $\mathbf{x}_i$. The weights for each edge of the graph are typically chosen to be a constant or computed by an exponential decay function such as a heat kernel [49] or Gaussian kernel [50]. The low dimensional data points, $\mathbf{y_i}$, are found by minimizing the following cost function

$$\epsilon_{Lap} = \sum_{i=1}^{N}\sum_{j=1}^{N} W_{ij}|\mathbf{y}_i - \mathbf{y}_j|^2 \tag{8.3}$$

where w_{ij} are the weights of edges in the neighborhood graph. The cost function is minimized subject to constraints that the d-dimensional vectors, $\mathbf{y}_i$, are centered and have unit covariance. This particular cost function aims to preserve proximity relations by projecting nearby points in the original data set, as measured by the weight matrix, to nearby points in $\mathbb{R}^d$.

The cost function, ϵ_{Lap}, can be expressed in terms of a graph Laplacian [51], $\mathbf{L} = \mathbf{D} - \mathbf{W}$, where $\mathbf{D}$ is the diagonal weight matrix, $D_{ii} = \sum_j W_{ij}$, by [51]

$$\epsilon_{Lap} = \mathrm{Tr}\left(\mathbf{Y}^{\mathsf{T}}\mathbf{L}\mathbf{Y}\right) \tag{8.4}$$

and minimizing this cost function subject to the constraints, centering and unit covariance of the $\mathbf{y}_i$'s, is equivalent [52] to finding the d eigenvectors associated with the d smallest nonzero eigenvalues of the generalized eigenvalue problem

$$\mathbf{L}\mathbf{v} = \lambda\mathbf{D}\mathbf{v} \tag{8.5}$$

CHAPTER 8: REVIEW OF DIMENSIONALITY REDUCTION TECHNIQUES

8.3 Comparison of the Algorithms

Now that we have reviewed some of the most commonly used dimensionality reduction techniques we will compare the results of each when applied to a set of data points in three dimensions lying on a two dimensional manifold. This will allow visualization of the results and, since the manifold which the data points lie on is known *a priori*, the effectiveness of each algorithm at revealing the structure of the manifold can be compared.

We begin with a data set sampled from the S-curve that was used in Section 8.1.1. Applying the nonlinear techniques to this data set allows a comparison with the linear methods, PCA and MDS, shown in Figure 8.1. Each algorithm, Isomap, LLE and Laplacian eigenmaps, was applied to a set of 2000 points sampled from the S-curve, shown in 8.1. We used the same number of nearest neighbors for each algorithm, $K = 15$, and the resulting two dimensional representations of the data set are shown in Figure 8.2.

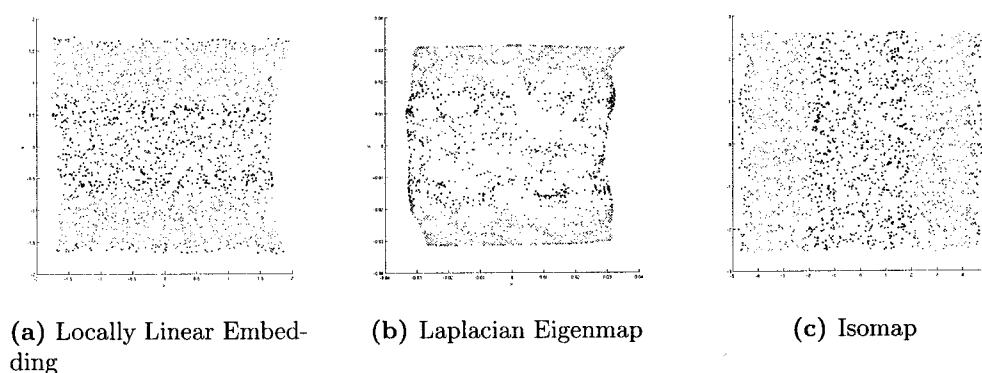(a) Locally Linear Embedding   (b) Laplacian Eigenmap   (c) Isomap

Figure 8.2: Nonlinear dimensionality reduction algorithms applied to 2000 points sampled from the S-shaped manifold shown in Figure 8.1. Comparison with Figure 8.1 shows the improved results in unfolding the two dimensional manifold compared to the linear methods of PCA and metric MDS.

The S-shaped manifold example shows how each of the nonlinear techniques can represent the data points correctly in the lower dimensional space when the manifold they are sampled from is curved in the higher dimensional space. Next we will test each of the algorithms on a set of data points that are generated by a Gaussian function. The lower dimensional manifold that these points lie on looks like a curved surface in three dimensions. We will use an input data set consisting of 2000 points, in this case the data points were generated from the following Gaussian function,

$$z = \left(\frac{1}{2\pi}\right) e^{(-x^2-y^2)/2} \tag{8.6}$$

by using 2000 pairs of random numbers, between zero and one, for the coordinates x and y. A useful feature of the data generated in this way is that it mimics non-uniform sampling of a lower dimensional manifold. This can be seen in Figure 8.3 where there is a high density of points for large z and the data set becomes sparse for lower values of z. This input data set is shown alongside the two dimensional representation obtained by the Laplacian eigenmap algorithm using 15 nearest neighbors, in Figure 8.3. The representations obtained by Isomap and LLE applied to the same input data set, also using 15 nearest neighbors, are shown in Figure 8.4

It is clear from Figures 8.3 and 8.4 that the Laplacian eigenmap algorithm does not represent the data set well in two dimensions. The reason for this, as Belkin and Niyogi have stated [48], is that there is an implicit assumption of uniform sampling of data points on the manifold in the Laplacian eigenmap algorithm. For data sets where the points are approximately uniform over an underlying manifold the algorithm can

CHAPTER 8: REVIEW OF DIMENSIONALITY REDUCTION TECHNIQUES

(a) Gaussian Data Set

(b) Laplacian Eigenmap
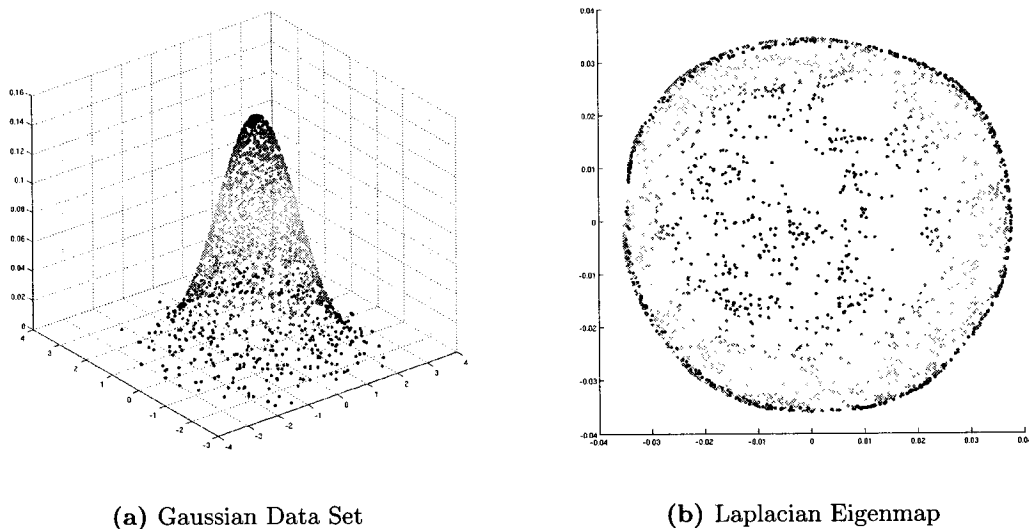
Figure 8.3: The Laplacian eigenmap algorithm applied to 2000 points obtained using a Gaussian function, Equation 8.6, to simulate non-uniform sampling of a low dimensional manifold, 15 nearest neighbors were used.

(a) Isomap

(b) LLE
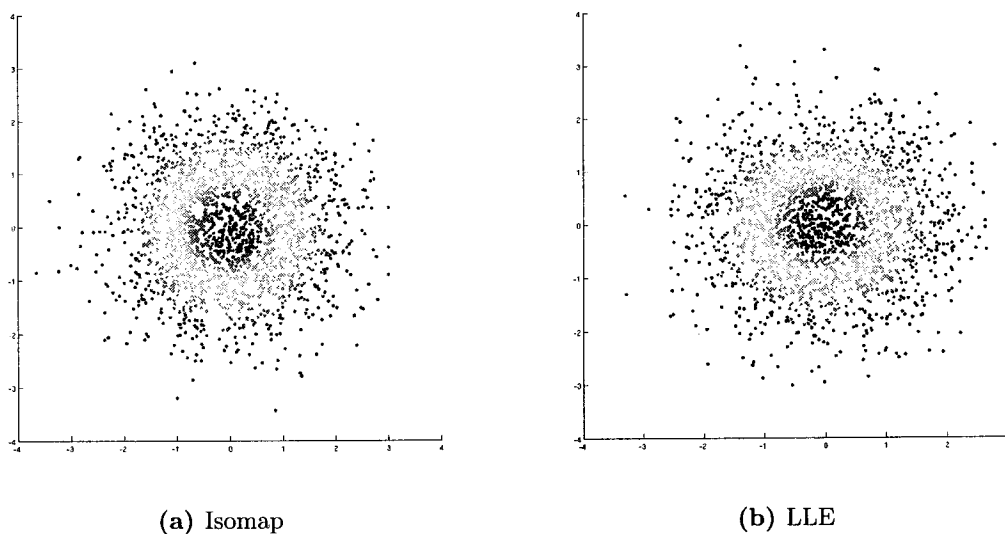
Figure 8.4: The two dimensional representations of the Gaussian data set from Figure 8.3 obtained by Isomap and Locally linear embedding both using 15 nearest neighbors.

CHAPTER 8: REVIEW OF DIMENSIONALITY REDUCTION TECHNIQUES

produce a faithful representation of the data in the lower dimensional space. This was observed for the S-curve example in Figure 8.2. The result from the Gaussian data set in Figure 8.3 shows that the uniformity of the data set over the manifold is an important consideration when determining which dimensionality reduction technique to apply.

Another important consideration is the run time for each of the algorithms. This can vary considerably amongst the different methods. If a dimensionality reduction technique is to be applied to surrogate UPO's in a strange attractor they will have to be run numerous times. This is because a lower dimensional representation will be required for several pairs of surrogate UPO's to construct a table of their linking numbers. Furthermore, this must be repeated as the control parameter is varied for the range $0 < \beta < 8$. This will be explained further in Chapter 9.

A comparison of the run times for the different algorithms was made by applying each method to the same input data set and using the same number of nearest neighbors. The results are shown in Table 8.1, which shows the run time for each algorithm when applied to 2000 points sampled from the S-shaped manifold shown in Figure 8.1. PCA was the fastest procedure and the times normalized to this value are given for ease of comparison. Some other techniques that were not discussed in this section have been included to give a better sense of typical run times. These additional methods are diffusion maps [45], local tangent space alignment (LTSA) [53, 54], and Hessian locally linear embedding (HLLE) [55, 56]. Each of these algorithms were implemented using codes publicly available from the authors of the original papers.

The algorithm that stands out the most from this list is Isomap, which takes

---

CHAPTER 8: REVIEW OF DIMENSIONALITY REDUCTION TECHNIQUES

considerably longer to run than any of the other techniques. This is mainly due to the second step of the algorithm, see Section 8.2.1, which involves calculating the approximate geodesic distances between points and also because it uses MDS which was one of the slowest algorithms. This can prohibit the use of Isomap for large data sets although there have been several modified versions of the algorithm developed to help address this issue [57–59].

Table 8.1: Comparison of run times for several dimensionality reduction techniques when applied to the S-shaped manifold with 2000 points using 15 nearest neighbors

Algorithm	Time (s)	Scaled Time (t/t_{PCA})
PCA	0.39	1
Laplacian Eigenmap	2.43	6.23
Diffusion Map	3.25	8.33
LLE	4.61	11.90
LTSA	6.97	17.87
Hessian LLE	61.50	157.69
MDS	96.66	247.85
Isomap	387.23	992.90

8.4 Summary

In this chapter we have reviewed several of the most popular dimensionality reduction algorithms. The two classical techniques considered, PCA and MDS, are closely related but differ in the format of the input data sets. PCA is a very fast process that can be used to quickly obtain a low dimensional representation of a data set that is

CHAPTER 8: REVIEW OF DIMENSIONALITY REDUCTION TECHNIQUES

essentially equivalent to a series of rotations and projections. MDS requires an input data set consisting of pairwise distances rather than a set of coordinates. The linear nature of these algorithms means that they are incapable of detecting the intrinsic structure of a data set lying on a curved manifold. This was clearly demonstrated in Figure 8.1 for data points sampled from a two dimensional S-shaped manifold in $\mathbb{R}^3$.

The nonlinear techniques that were discussed are Isomap, LLE and Laplacian eigenmaps. An overview of each technique was given and the ability of these algorithms to essentially unfold the S-shaped manifold was shown in Figure 8.2. A comparison of the algorithms was made, in Section 8.3, that focused on two main attributes. These were the ability of the algorithms to deal with non-uniformly sampled data and the computational efficiency of each algorithm. Isomap and LLE were both successful in revealing the intrinsic structure of a two dimensional Gaussian data set in Figure 8.4. However, the Isomap was found to run much slower on these data sets than the LLE algorithm.

The motivation for comparing the speed of the algorithms and the ability to handle non-uniformly sampled data comes from thinking about the surrogate UPO's in the EMR strange attractor. We would like to be able to apply a dimensionality reduction technique to these surrogate orbits, since they are assumed to lie in a three dimensional manifold in $\mathbb{R}^4$. This would allow the computation of Gauss linking numbers for pairs of orbits. These computations must be repeated for many pairs of orbits to construct a table of linking numbers. Furthermore, this table should be computed over the control parameter range $0 < \beta < 8$ to check whether the linking numbers change value. Since a repeated use of the dimensionality reduction

CHAPTER 8: REVIEW OF DIMENSIONALITY REDUCTION TECHNIQUES

is required the efficiency of the algorithm is an important factor. Also, there is no reason to assume that data points from a surrogate UPO, or points sampled from the strange attractor, should be spread uniformly in an underlying three dimensional manifold. Since LLE was capable of dealing with non-uniformly sampled data points and has a reasonable run time, see Table 8.1, we choose this method to find a three dimensional representation of surrogate UPO's in Chapter 9.

CHAPTER 8: REVIEW OF DIMENSIONALITY REDUCTION TECHNIQUES

Chapter 9: Locally Linear Embedding

In this chapter we begin by explaining the LLE algorithm in detail. The algorithm requires two input parameters, the embedding dimension and the number of nearest neighbors. In Section 9.2 we describe the specific regularization required when the embedding dimension is less than the number of nearest neighbors. In Section 9.3 we give the procedure for preparing the data set in the higher dimensional space, $\mathbb{R}^4$. In Section 9.4 the remaining input to the algorithm is determined, namely the number of nearest neighbors, K. Finally the LLE algorithm is applied to the UPO's and a table their linking numbers is computed in Section 9.5.

9.1 The Algorithm

LLE assumes that each data point in a high dimensional space lies on a lower dimensional nonlinear manifold [35]. The input to the algorithm is a set of N vectors in $\mathbb{R}^D$ that lie on a manifold of dimension d, with $d < D$. Furthermore, it is assumed that each data point and its neighbors lie close to a locally linear patch of the manifold. The algorithm aims to reconstruct the original data set in a lower dimensional space that best preserves the local geometry of every neighborhood and outputs a set of N vectors in $\mathbb{R}^d$.

There are three main steps to the algorithm:

1. Assign neighbors to each data point in the original data set.

2. Compute the weights that best linearly reconstruct each data point from its neighbors.

3. Find the vectors in the low-dimensional space by fixing the weights to be those found in step 2 and minimizing the cost function.

Each of these steps will now be explained in more detail.

Assigning the nearest neighbors to each data point usually involves one of two methods. This is to either take the K-nearest data points based on Euclidean distance (K-nearest neighbors) or to choose the neighbors contained in a ball of fixed radius, ϵ, centered on each data point (ϵ-ball). In either case, choosing the number of neighbors to properly reconstruct each data point may be difficult [60]. If the number of neighbors is too small then the local geometry is not well characterized by the weights and if it is too large then the assumption of a locally linear neighborhood is violated. We will consider the K-nearest neighbors based on Euclidean distance. The choice of the value of K will be discussed in Section 9.4. The exact relation between K and the faithfulness of the resulting embedding remains an important open question [35].

Consider a data set consisting of N points. By thinking of each data point in the higher-dimensional space as a vector, $\vec{X}_i$, each can be reconstructed through a linear combination of its neighbors. The error in this reconstruction is measured by the cost function,

$$\varepsilon(W) = \sum_{i=1}^{N} \left| \vec{X}_i - \sum_{j=1,j\neq i}^{N} W_{ij}\vec{X}_j \right|^2 \qquad (9.1)$$

CHAPTER 9: LOCALLY LINEAR EMBEDDING

which adds up the squared distances between all the data points and their reconstructions. The weights, W_{ij}, are found by minimizing this cost function subject to two constraints. The first is that each data point is reconstructed only from its neighbors, i.e. $W_{ij} = 0$ if $\vec{X}_j$ is not a neighbor of $\vec{X}_i$ and $W_{ii} = 0$. The second constraint is

$$\sum_j W_{ij} = 1 \tag{9.2}$$

which imposes translational invariance. This can be seen by considering the effect of adding a constant vector, $\vec{c}$, to $\vec{X}_i$ and each of its neighbors. The cost function becomes

$$
\begin{aligned}
\varepsilon(W) &= \sum_{i=1}^{N} \left| \left(\vec{X}_i + \vec{c} \right) - \sum_{j=1}^{N} W_{ij} \left(\vec{X}_j + \vec{c} \right) \right|^2 \tag{9.3} \\
&= \sum_{i=1}^{N} \left| \left(\vec{X}_i + \vec{c} \right) - \sum_{j=1}^{N} W_{ij} \vec{X}_j - \sum_{j=1}^{N} W_{ij} \vec{c} \right|^2 \\
&= \sum_{i=1}^{N} \left| \vec{X}_i + \vec{c} - \sum_{j=1}^{N} W_{ij} \vec{X}_j - \vec{c} \right|^2 \\
&= \sum_{i=1}^{N} \left| \vec{X}_i - \sum_{j=1}^{N} W_{ij} \vec{X}_j \right|^2
\end{aligned}
$$

which is the same as Equation 9.1 showing that the cost function is translation invariant under the constraint given by Equation 9.2.

The third step also involves minimization of the cost function. However, this time the weights are fixed and the vectors are found that minimize the reconstruction error.

CHAPTER 9: LOCALLY LINEAR EMBEDDING

The weights from step two are used in minimizing the embedding cost function,

$$\Phi(Y) = \sum_{i=1}^{N} \left| \vec{Y_i} - \sum_{j=1}^{N} W_{ij} \vec{Y_j} \right|^2 \qquad (9.4)$$

where $\vec{Y_i}$ are the low dimensional embedding vectors.

The minimization is performed subject to two constraints. The first constraint removes the translational degree of freedom such that the output vectors, $\vec{Y_i}$, are centered on the origin,

$$\sum_{i=1}^{N} \vec{Y_i} = \vec{0} \qquad (9.5)$$

The embedding cost function is unaffected by a rotation of the vectors, $\vec{Y_i}$. The second constraint removes the rotational degree of freedom such that the output vectors have unit covariance,

$$\frac{1}{N} \sum_{i=1}^{N} \vec{Y_i} \vec{Y_i}^{\mathsf{T}} = I_d \qquad (9.6)$$

The embedding cost function Equation (9.4) can be rewritten in terms of a cost matrix,

$$\Phi(Y) = \sum_{i=1}^{N} \sum_{j=1}^{N} M_{ij} (\vec{Y_i} \cdot \vec{Y_j}) \qquad (9.7)$$

CHAPTER 9: LOCALLY LINEAR EMBEDDING

where the cost matrix is given by,

$$M_{ij} = \delta_{ij} - W_{ij} - W_{ji} + \sum_{k=1}^{N} W_{ki}W_{kj} \tag{9.8}$$

Minimizing Equation (9.4) is equivalent to finding the eigenvectors corresponding to the $d+1$ lowest eigenvalues of the cost matrix, since the eigenvector corresponding to eigenvalue zero, $(1, 1, ..., 1)$, represents a free translation (Goldstone mode [61]). This equivalence is a form of the Rayleigh-Ritz theorem [62].

The result of applying this algorithm to points sampled from a two dimensional manifold in $\mathbb{R}^3$ is shown in Figure 9.1.
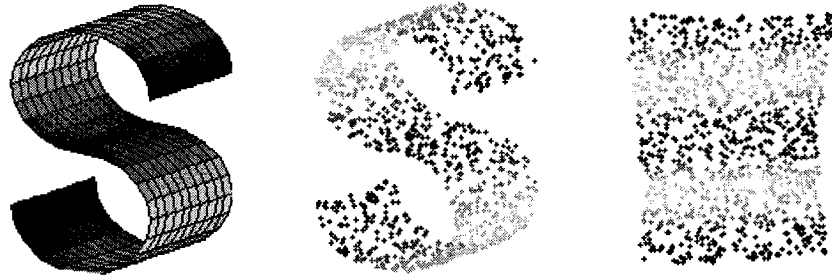
Figure 9.1: LLE applied to the two dimensional S-shaped manifold. 1000 points were sampled from the known manifold and the resulting embedding was computed using 12 nearest neighbors.

The S-shaped manifold is a common example used for testing dimensionality reduction techniques [63]. In this case 1000 points were sampled from the manifold and 12 nearest neighbors were used to compute the two dimensional embedding. The rightmost image in Figure 9.1 shows how the LLE algorithm is capable of unfolding the data set to reveal the intrinsic two dimensional structure. LLE has also been successfully applied to other manifolds, such as the "Swiss Roll" manifold [64]. Some

CHAPTER 9: LOCALLY LINEAR EMBEDDING

example applications of LLE include analysis of data sets of hyperspectral images [65] and articulated shape matching [66].

LLE aims to preserve intrinsic geometric properties of every neighborhood. These are the intrinsic properties characterized by the reconstruction weights. These constrained weights, for any particular data point, are invariant to rotations, rescalings, and translations of that data point and its neighbors. The algorithm is effective in revealing global nonlinear structure through the local symmetries of linear reconstructions [35]. The effectiveness depends on the two inputs to the algorithm, the number of nearest neighbors and the embedding dimension. For problems where the data points are assumed to lie on a nonlinear manifold of known dimension the important question is: how does the choice of number of nearest neighbors affect the lower dimensional embedding? This will be addressed in section 9.5 where the algorithm will be applied to orbits in $\mathbb{R}^4$.

9.2 $K > D$ regularization

There is a subtlety that has been glossed over in the preceding section. In step 2 of the LLE algorithm, where the cost function is minimized, it may be the case that there is no unique solution. In fact, when the number of nearest neighbors is greater than the dimension of the input vectors, $K > D$, the problem of minimizing $\varepsilon(W)$ in Equation (9.1) becomes ill-posed. The minimization problem is under-determined since there are K unknown weights and D equations. One common way to regularize such problems is through Tikhonov regularization [67]. This approach involves solving

the following minimization problem

$$\varepsilon_r(W) = \sum_{i=1}^{N} \left(\left| \vec{X}_i - \sum_{j=1}^{N} W_{ij} \vec{X}_j \right|^2 + \alpha \sum_{j=1}^{N} W_{ij}^2 \right) \tag{9.9}$$

where $\varepsilon_r(W)$ is the regularized cost function and $\alpha > 0$. The additional term $\alpha \sum_j W_{ij}^2$ is known as a regularizer or penalty term and the original cost function is recovered as $\alpha \to 0$.

The regularizer has the effect of penalizing the sum of the squared weights. In other words, it favors weights that are uniformly distributed in magnitude. This can be seen by considering the limit as $\alpha \to \infty$. In this case, minimizing the cost function amounts to minimizing the sum of the squared weights. Under the constraint given by Equation (9.2), minimization will be achieved when all of the weights are equal in magnitude.

Considering the regularized cost function for a particular point, $\vec{X}_i$, with K nearest neighbors, Equation (9.9) can be rewritten as

$$\varepsilon_r^{(i)}(W) = \left| \sum_{j=1}^{K} W_{ij}(\vec{X}_i - \vec{X}_j) \right|^2 + \alpha \sum_{j=1}^{K} W_{ij}^2 \tag{9.10}$$

where the constraint imposed by Equation (9.2) has been utilized. In terms of the local $K \times K$ Gram matrix given by

$$G_{jl}^i = (\vec{X}_i - \vec{X}_j).(\vec{X}_i - \vec{X}_l) \tag{9.11}$$

CHAPTER 9: LOCALLY LINEAR EMBEDDING

this becomes

$$\varepsilon_r^{(i)}(W) = \mathbf{w}_i^\mathsf{T} \mathbf{G_i} \mathbf{w_i} + \alpha \mathbf{w}_i^\mathsf{T} \mathbf{w}_i \qquad (9.12)$$

where $\mathbf{w_i}$ is the $K \times 1$ weight matrix. The regularized cost function can be minimized under the constraint given by Equation (9.2) using a Lagrange multiplier, λ. The Lagrangian is given by

$$\mathcal{L}(\mathbf{w_i}, \lambda) = \mathbf{w}_i^\mathsf{T} \mathbf{G_i} \mathbf{w_i} + \alpha \mathbf{w}_i^\mathsf{T} \mathbf{w}_i - \lambda(\mathbf{1}^\mathsf{T} \mathbf{w}_i - 1) \qquad (9.13)$$

where $\mathbf{1}$ is a $K \times 1$ matrix of all ones. Minimizing the Lagrangian with respect to $\mathbf{w_i}$ gives

$$(\mathbf{G_i} + \alpha \mathbf{I})\mathbf{w_i} = \frac{\lambda}{2}\mathbf{1} \qquad (9.14)$$

Solving for the reconstruction weight and choosing λ such that the solution is normalized gives

$$\mathbf{w}_i = \frac{\lambda}{2}(\mathbf{G}_i + \alpha \mathbf{I})^{-1}\mathbf{1} \qquad (9.15)$$

$$\mathbf{w}_i = \frac{\sum_{l=1}^{k}(G + \alpha I)_{il}^{-1}}{\sum_{m=1}^{k}\sum_{n=1}^{k}(G + \alpha I)_{mn}^{-1}} \qquad (9.16)$$

The regularization is usually chosen such that $\alpha \ll 1$. For example, Roweis and Saul

---

[35] recommend conditioning the Gram matrix in the following way

$$G^i_{jk} \leftarrow G^i_{jk} + \left(\frac{\Delta^2}{K}\right) \mathrm{Tr}(G) \qquad (9.17)$$

with $\Delta^2 \ll 1$. This was the conditioning used, with $\Delta^2 = 1 \times 10^{-3}$, for the S-curve example in Figure 9.1. This $K > D$ regularization will also be implemented when applying LLE to UPO's within the EMR attractor, (Chapter 3), since $D = 4$ and the number of nearest neighbors used will always be greater than four.

9.3   Preparing the orbits

In order to apply LLE to these orbits we take not only the surrogates but also a set of points sampled from the attractor that lie near to these orbits in $\mathbb{R}^4$. LLE does not require a uniform sampling of points in the phase space. However, these sampled points should be spread evenly across each of the orbits to reveal the geometry of the underlying manifold that the attractor is assumed to lie in. The sampled points are found by integrating from an initial condition and recording the coordinates each time the trajectory passes within a given distance of the surrogate orbits. We denote this threshold distance between the trajectory and surrogate orbit by δ_{to}. The closeness condition is not checked at every time step because this would cause clumping of the sampled points. Instead the distance between the integrated trajectory and the orbits is checked at regular time intervals, denoted by Δt. This results in a more even spread of the sampled data points along the orbits. The data set generated in this way contains two surrogate orbits, since we wish to calculate linking numbers for

CHAPTER 9:   LOCALLY LINEAR EMBEDDING

pairs of orbits, along with the points sampled from the attractor.

As an example, we will consider the two UPO's LR and LR^2 for $\beta = 5.0$. They contain 347 and 556 points respectively. The points sampled from the attractor were obtained by integrating from an initial point within the basin of attraction $(x, y, z, u) = (11.67, 22.56, 28.00, 1.36)$ for 300 seconds with a time step of $dt = 0.01$. As noted by Schuon et al [68] and Kim & Finkel [65], the CPU power and memory requirements can be quite high when applying LLE to large data sets. For this reason the final data set was kept below 5000 points. In this case it was found that a closeness condition of $\delta_{t_o} = 1.0$ and time interval, $\Delta t = 5$, gave 2851 sampled points. A plot of these sampled points with the two surrogate periodic orbits is shown in Figure 9.2.
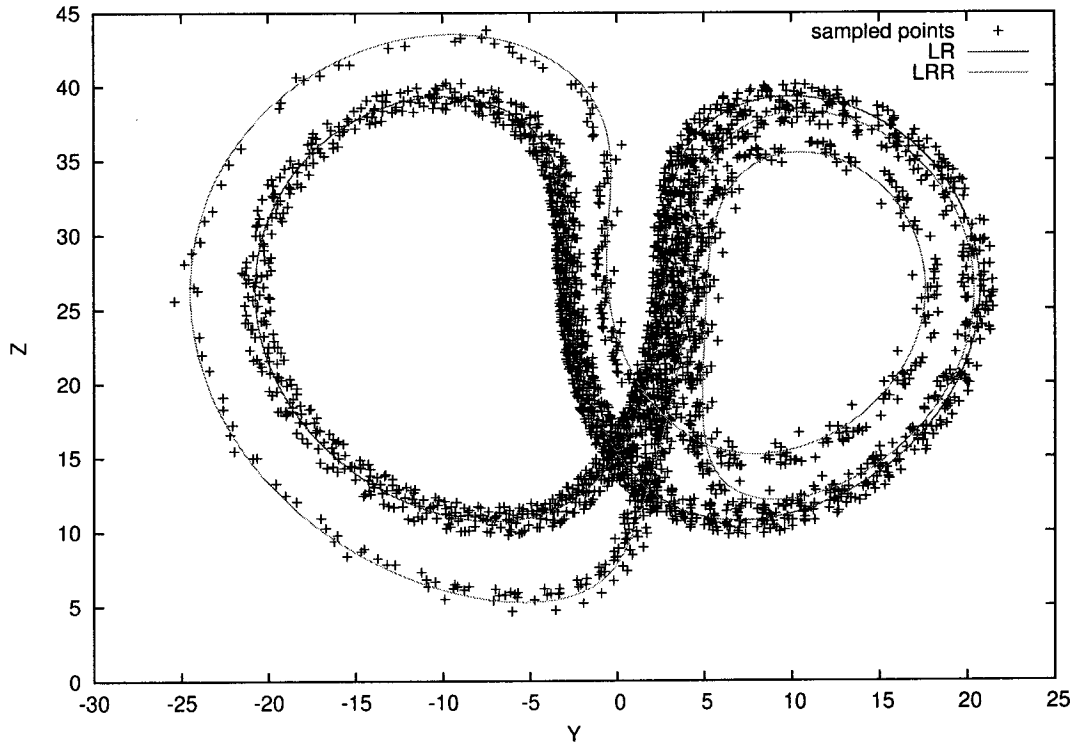

Figure 9.2: The Y-Z projection of two surrogate UPO's, LR and LRR, for $\beta = 5.0$, with 2851 points sampled from the underlying three-dimensional manifold. The orbit LR consists of 347 points and the orbit LRR consists of 556 points.

CHAPTER 9: LOCALLY LINEAR EMBEDDING

9.4 Choice of nearest neighbors

Implementing the LLE algorithm requires only two input parameters: the embedding dimension, d, and the number of nearest neighbors, K. The manifold containing the attractor is assumed to be three-dimensional, since $D_L = 2.2$, so we set $d = 3$. However the choice of the value of K is not so straightforward. If K is too small then the geometry of the manifold is not recovered due to undersampling. If K is too large then the assumption that the neighborhood is locally linear would be violated. The aim is to find a range of K values over which the embedding remains stable. Figures 9.3, 9.4 and 9.5 show the orbit $LLRR$ embedded in three dimensions for three different values of K.
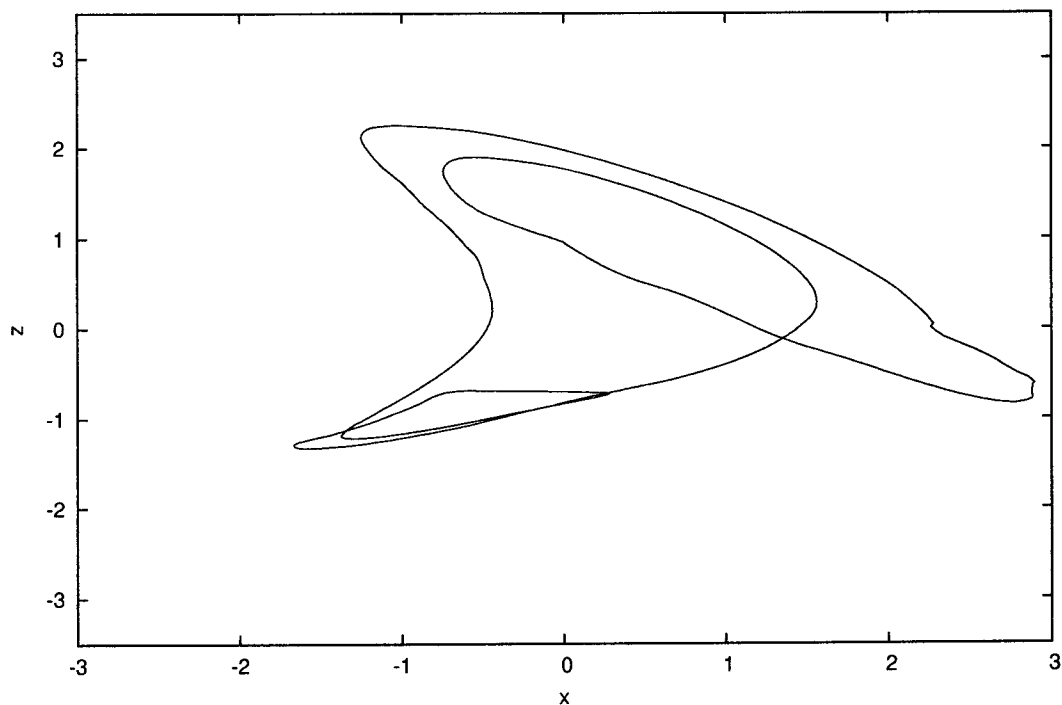

Figure 9.3: Locally linear embedding of the orbit $LLRR$ for $K = 10$.

CHAPTER 9: LOCALLY LINEAR EMBEDDING
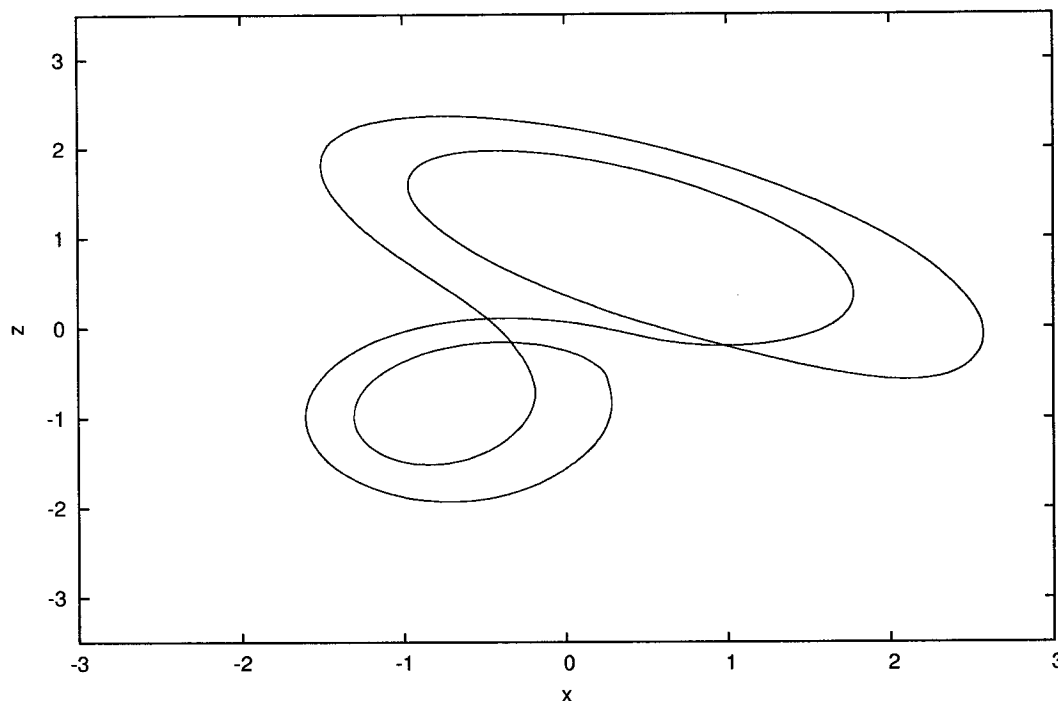
Figure 9.4: Locally linear embedding of the orbit *LLRR* for $K = 20$.

In each case, the points sampled from the strange attractor were removed from the data set after the LLE algorithm had been applied. Then, a specific orientation was chosen in the three-dimensional space; this is possible because LLE is invariant up to a rotation. Three dimensional representations with different parity are isotopic in $\mathbb{R}^4$ [69]. To ensure the orbits were projected to the lower dimension in a consistent way, the following orientation convention was adopted. For each orbit, the point closest to the component R of the Poincaré section (Figure 4.1) was determined. The orbit was then rotated so that this point was on the x-axis with the tangent vector at this point directed with components in the positive x, y and z directions. Orienting each orbit in the same sense allowed each of the embeddings to be compared to find the

CHAPTER 9: LOCALLY LINEAR EMBEDDING
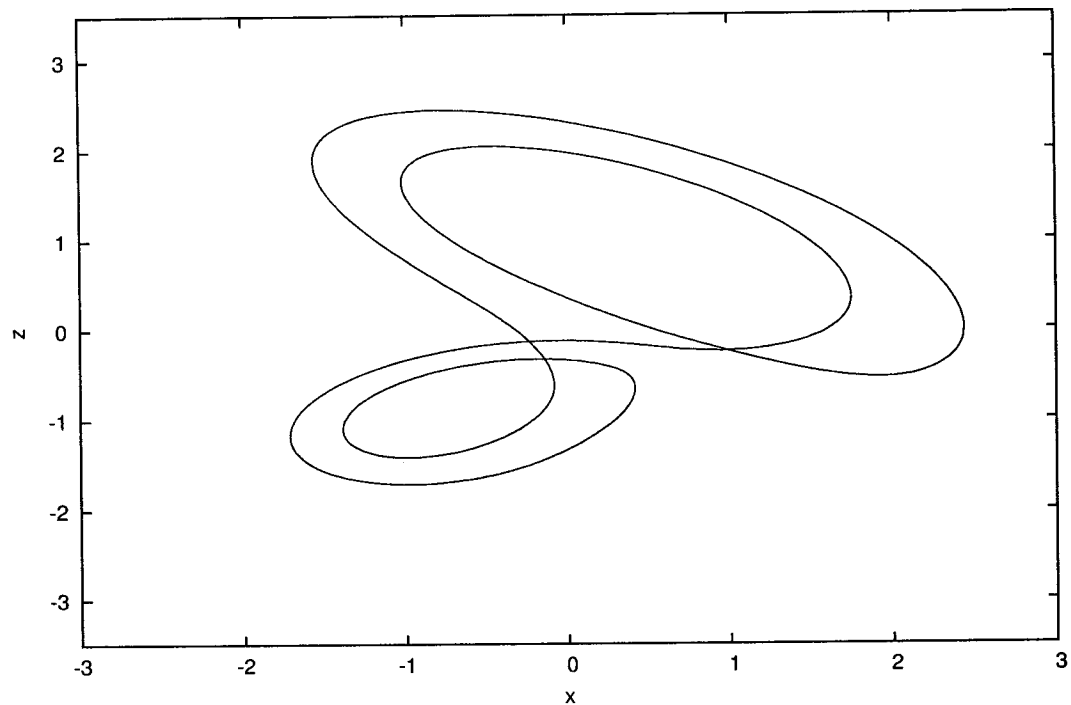
Figure 9.5: Locally linear embedding of the orbit $LLRR$ for $K = 30$.

range of K values over which the embedding remained stable.

9.5   Results and comparison with projection methods

Many surrogate UPO's were found in $\mathbb{R}^4$ using the method of close returns described in Section 4.1. Application of LLE to pairs of these surrogates should yield an embedding in three dimensions where linking numbers can be computed to reveal the organization of these UPO's in this lower dimensional space.

As an example, we will consider the two UPO's LR and L^2R^2. In order to apply LLE to these UPO's we take not only the surrogates but also a set of points sampled from the attractor that lie near to these orbits. This data set is generated using the

CHAPTER 9:   LOCALLY LINEAR EMBEDDING

procedure described in Section 9.3. A sufficient number of sampled points will supply the nearest neighbors required to reveal the geometry of the underlying manifold that the attractor is assumed to lie in. This manifold is assumed to be three dimensional so, with the target dimension set to $d = 3$, there is only one remaining input to the algorithm - the number of nearest neighbors. From inspection of the embedded orbits it was found that a K value in the range 16-22 provided the best embeddings. The embedding of the orbits LR and L^2R^2 into $\mathbb{R}^3$ using 18 nearest neighbors is shown in Figure 9.6.
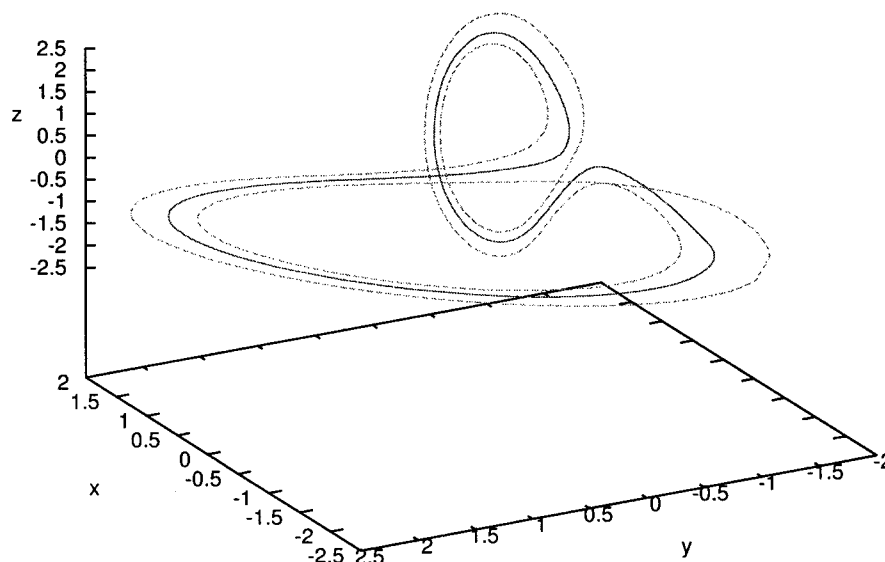

Figure 9.6: Two UPO's LR and L^2R^2 for $\beta = 6.99$ embedded in $\mathbb{R}^3$ using $K = 20$.

The linking numbers for pairs of orbits, in the three-dimensional embedding, were computed by counting crossings in the x-z projection. These linking numbers were

CHAPTER 9: LOCALLY LINEAR EMBEDDING

computed for all values of K in the range $5 \leq K \leq 40$. For the lowest values of K the linking numbers were found to vary depending on the number of nearest neighbors used. This type of error should be expected from inspection of Figure 9.3. However, for all pairs of orbits, the linking number was found to remain the same for all values of K above a certain threshold value. For all the orbits studied here, $K = 20$ proved to be a sufficient number of nearest neighbors since it was contained within the range over which the linking number remained constant.

The results are shown in Table 9.1, for all UPO's up to period five. These results are consistent with those for the Lorenz branched manifold with rotation symmetry. The most important aspect of these results is that the table of linking numbers remains the same for the entire range of control parameter, $0 < \beta < 8.0$. For the orbits involved in homoclinic bifurcations, (indicated by a *), the linking numbers were the same before and after they were removed and then re-introduced to the strange attractor. This is under the previously mentioned assumption that there is a three-dimensional manifold in which the attractor may be embedded. No self intersections were observed as with the simple projections discussed in Chapter 5.

CHAPTER 9: LOCALLY LINEAR EMBEDDING

Table 9.1: The linking numbers of unstable periodic orbits that were embedded using LLE. * indicates orbits involved in homoclinic bifurcations, these linking numbers were only calculated for control parameter values where the orbits where present in the strange attractor.

	LR	LLR	LRR	LLLR*	LRRR*	LLRR	LLLLR*	LLLRR	LLRRR	LLRLR	LRRLR	LRRRR*
LR	-	1	1	1	1	2	1	2	2	2	2	1
LLR	1	-	1	2	1	2	2	3	2	3	2	1
LRR	1	1	-	1	2	2	1	2	3	2	3	2
LLLR*	1	2	1	-	1	2	3	3	2	3	2	1
LRRR*	1	1	2	1	-	2	1	2	3	2	3	3
LLRR	2	2	2	2	2	-	2	3	3	4	4	2
LLLLR*	1	2	1	3	1	2	-	3	2	3	2	1
LLLRR	2	3	2	3	2	3	3	-	3	5	4	2
LLRRR	2	2	3	2	3	3	2	3	-	4	5	3
LLRLR	2	3	2	3	2	4	3	5	4	-	4	2
LRRLR	2	2	3	2	3	4	2	4	5	4	-	3
LRRRR*	1	1	2	1	3	2	1	2	3	2	3	-

CHAPTER 9: LOCALLY LINEAR EMBEDDING

Chapter 10: Conclusion

A topological analysis program exists for three dimensional strange attractors but there are no analogous methods when the dimension is higher than three. We show, for the first time, how the current program can be extended to a strange attractor in $\mathbb{R}^4$. This extension is possible for strange attractors in higher dimensional spaces when the attractor is essentially three dimensional, with Lyapunov dimension that satisfies, $D_L < 3$.

We have analyzed a strange attractor generated by the four dimensional dynamical system that was introduced in Chapter 3. This analysis was conducted in three different ways, each with the goal of determining the topological organization of the UPO's within the attractor. The three different methods are

1. Projections of the strange attractor into three dimensional subspaces

2. Using a four dimensional linking integral

3. Applying a dimensionality reduction technique (LLE) to surrogate UPO's

A previous study [10] on projections to the (X, Y, Z) and (X, Y, U) subspaces claims that the (X, Y, U) projection is an embedding of the attractor for all values of the control parameter in the range $0 < \beta < 8$. We were able to show that this is not the case by computing the linking numbers for the period five UPO's. The linking numbers for these orbits changed as the control parameter, β, was varied. For $\beta > 1.5$

we found that this projection did provide an embedding that was consistent with the Lorenz branched manifold with inversion symmetry but for $\beta < 1.5$ an embedding no longer existed. Near $\beta = 1.5$, self-intersections occurred as the uniqueness principle was violated in this projection. This was confirmed by calculating the minimum distance between surrogate UPO's for $0 < \beta < 8$, this result is shown in Figure 5.4. In the (X, Y, Z) projection our results agreed with the previous study. This projection provides an embedding for low values of β that is consistent with a Lorenz branched manifold with rotational symmetry. As β is increased the linking numbers change through integer steps as self intersections of the attractor occur. This occurs until a value of β is reached where the attractor has essentially turned inside out and the linking numbers become the negative of those for low values of β. At this point the table of linking numbers is consistent with a branched manifold that is the mirror image of that for the low β regime.

During the analysis of projections to three-dimensional subspaces it was discovered that not all of the low period UPO's could be found over the entire range, $0 < \beta < 8$, by the method of close returns. When this occurred, the surrogates could be found for low values of β and again for higher values, but there was an intermediate range of β values for which no surrogates could be found. This behavior was explained in Chapter 6 by analyzing the sequence of homoclinic bifurcations for this attractor. As the control parameter, β, is increased, some of the UPO's are first removed and then re-introduced back into the attractor by the sequence of homoclinic bifurcations. The sequence was determined for orbits up to period six and is given in Table 6.1.

The second technique involved a higher dimensional linking integral that has re-

CHAPTER 10: CONCLUSION

cently been introduced [1]. The linking integral applies to the case of visible hyper-surfaces. We were able to find a visible point, in $\mathbb{R}^4$, by calculating the minimum distance between rays emanating from that point and the strange attractor. Linking numbers for UPO's are commonly computed by the Gauss integral, in three dimensions, but never for dimension greater than three. By locating the visible point in $\mathbb{R}^4$ we were able to compute the linking numbers for pairs of UPO's using the four dimensional linking integral. The table of linking numbers calculated in this new way is presented in Table 7.1.

In Chapter 8 we reviewed several of the most popular dimensionality reduction techniques. The nonlinear methods were tested on sample data sets and compared in terms of their efficiency and ability to handle non-uniform sampling. The results are presented in Table 8.1. This comparison of the different methods highlighted three key characteristics of the LLE algorithm. These were: (1) the ability of the algorithm to reveal the structure of an underlying nonlinear manifold, as demonstrated by the S-curve example, in Figure 8.2; (2) the successful representation of a non-uniformly sampled data set; and (3) reasonable computational cost compared with other dimensionality reduction techniques. For these reasons LLE was chosen for application to the UPO's in the strange attractor in $\mathbb{R}^4$.

In Chapter 9 we developed the method and procedures for applying the LLE algorithm to UPO's in the strange attractor in $\mathbb{R}^4$. The dimensionality reduction of these UPO's was successful in revealing the underlying structure of the three dimensional manifold that the attractor and its UPO's lie in. This allowed the computation of linking numbers for pairs of UPO's in the three dimensional representation. These

CHAPTER 10: CONCLUSION

calculations were stable over a range of the input parameter to the algorithm, the number of nearest neighbors K. A table of linking numbers was constructed, Table 9.1, for all UPO's up to period five. The linking numbers in this table remained the same for all values of the control parameter in the range $0 < \beta < 8$. The branched manifold consistent with this set of linking numbers is the Lorenz branched manifold with rotation symmetry. This uniquely determines the organization of the UPO's within this strange attractor.

So, where does this leave us? The problem of understanding strange attractors in spaces of dimension greater than three remains unresolved. If the attractor has *Lyapunov* dimension $D_L < 3$ it ought to be possible to squeeze the attractor into a three dimensional space, after which a topological analysis becomes possible. This thesis describes one successful way to carry out this program.

A more sophisticated way would be to find a standard method (a 'machine') for constructing a three-dimensional *inertial manifold* or *attracting manifold* in R^N ($N > 3$) and a change of coordinates so that three of the coordinates describe the flow in the three dimensional manifold and the remaining coordinate obeys an equation describing the asymptotic approach of any initial condition to this manifold. Such machinery exists to some extent in the theory of partial differential equations. Regrettably, it seems to be a hard problem to construct coordinate transformations for finite sets of ordinary differential equations to put them into the canonical form of a lower dimensional attracting manifold containing all of the interesting dynamics and additional equations showing exponential relaxation to this attracting manifold. If such a result could be constructed, and if the Lyapunov dimension of a strange

---

CHAPTER 10: CONCLUSION

attractor were confined to the range $2 < D_L < 3$, the attracting manifold ought to be three-dimensional, and it then ought to be possible to apply the methods of topological analysis.

It is hoped that one does not have to wait too long for results of this nature to be developed.

CHAPTER 10: CONCLUSION

Bibliography

[1] Clayton Shonkwiler and David Shea Vela-Vick. Higher-dimensional linking integrals. *Proc. Amer. Math. Soc.*, 139(4):1511–1519, 2011.

[2] R Gilmore. Topological analysis of chaotic dynamical systems. *Rev. Mod. Phys.*, 70(4):1455–1529, October 1998.

[3] R Devaney and Z Nitecki. Mathematical Physics Shift Automorphisms in the Henon Mapping. 146:137–146, 1979.

[4] R Gilmore and M Lefranc. *The Topology Of Chaos*. Wiley, New York, 2002.

[5] P Holmes and R F Williams. Knotted periodic orbits in suspensions of Smale's horseshoe: torus knots and bifurcation sequences. *Archive for Rational Mechanics and Analysis*, 90(2):115–194, 1985.

[6] G B Mindlin and H G Solari. Topologically inequivalent embeddings. *Phys. Rev. E.*, 52:1497–1502, 1995.

[7] Joan S Birman and R F Williams. Knotted periodic orbits in dynamical systems. I. Lorenz's equations. *Topology*, 22(1):47–82, 1983.

[8] J S Birman and R F Williams. Knotted periodic orbits in dynamical systems II: Knot holders for fibered knots. *Contemporary Mathematics*, 20:1–60, 1983.

[9] R Hide. The nonlinear differential equations governing a hierarchy of self-exciting coupled Faraday-disk homopolar dynamos. *Physics of the Earth and Planetary Interiors*, 103:281–291, 1997.

[10] E C Bullard. The stability of a homopolar dynamo. *Math. Proc. Cambridge Philos. Soc.*, 51:744–760, 1955.

[11] T Rikitake. Oscillations of a system of disk dynamos. *Proc. Camb. Phil. Soc.*, 54:89–105, 1958.

[12] W V R Malkus. Reversing Bullard's dynamo. *Eos Trans. Am. Geophys. Union*, 53:617, 1972.

[13] K A Robbins. A new approach to sub-critical instability and turbulent transitions in a simple dynamo. *Math. Proc. Cambridge Philos. Soc.*, 82:309–325, 1977.

[14] I M Moroz. The Malkus-Robbins Dynamo With A Linear Series Motor. *Int. J. of Bifurcation and Chaos*, 13:147–161, 2003.

[15] I.M. Moroz. The extended MalkusRobbins dynamo as a perturbed Lorenz system. *Nonlinear Dynamics*, 41(1):191–210, 2005.

[16] I M Moroz, C Letellier, and R Gilmore. When are projections also embeddings? *Phys. Rev. E.*, 75:46201, 2007.

[17] H K Moffat. A self-consistent treatment of simple dynamo systems. *Geophys. Astrophys. Fluid Dyn.*, 14:147–166, 1979.

[18] E N Lorenz. Deterministic nonperiodic flow. *J.Atm. Sci.*, 20:130, 1963.

[19] C Letellier, I M Moroz, and R Gilmore. A Topological Test for Embeddings. 2007.

[20] H Poincaré and R Magini. Les méthodes nouvelles de la mécanique céleste. *Il Nuovo Cimento (1895-1900)*, 10(1):128–130, 1899. ISSN 1827-6121.

[21] Greg Byrne, Robert Gilmore, and Christophe Letellier. Distinguishing between folding and tearing mechanisms in strange attractors. *Phys. Rev. E.*, 70(5):56214, November 2004.

[22] Christophe Letellier, Tsvetelin D Tsankov, Greg Byrne, and Robert Gilmore. Large-scale structural reorganization of strange attractors. *Phys. Rev. E.*, 72(2): 26212, August 2005.

[23] D F Elliott and K R Rao. *Fast transforms: algorithms, analyses, applications.* Computer Science and Applied Mathematics Series. Academic Press, 1982. ISBN 9780122370809.

[24] W H Press, W T Teukolsky, V Flannery, and B P Flannery. *Numerical Recipes.* Cambridge University Press, 1992. ISBN 0521574390.

[25] G B Arfken and H J Weber. *Mathematical methods for physicists.* Elsevier, 2005. ISBN 9780120598762.

[26] R Gilmore and C Letellier. *The Symmetry Of Chaos.* Oxford University Press, New York, 2006.

[27] V I Arnol'd. *Ordinary Differential Equations.* MIT Press, 1978.

[28] C Sparrow. *The Lorenz Equations: Bifurcations, Chaos, and Strange Attractors.* Springer-Verlag, 1982.

[29] Raymond Hide and I.M. Moroz. Effects due to induced azimuthal eddy currents in a self-exciting Faraday disk homopolar dynamo with a nonlinear series motor. I.:: Two special cases. *Physica D: Nonlinear Phenomena*, 134(2):287–301, 1999.

[30] Mathura S Venkatarajan and Werner Braun. New quantitative descriptors of amino acids based on multidimensional scaling of a large number of physical-chemical properties. *Journal of Molecular Modeling*, 7(12):445–453, 2001. ISSN 1610-2940.

BIBLIOGRAPHY

[31] Rui Xu, Steven Damelin, and Donald C Wunsch. Applications of diffusion maps in gene expression data-based cancer diagnosis analysis. In *In Proceedings of the Annual International Conference of the IEEE Engineering in Medicine and Biology Society.*, volume 2007, pages 4613–6, January 2007. ISBN 1424407885. doi: 10.1109/IEMBS.2007.4353367.

[32] R. Duraiswami and V.C. Raykar. The manifolds of spatial hearing. In *Acoustics, Speech, and Signal Processing, 2005. Proceedings.(ICASSP'05). IEEE International Conference on*, volume 3, pages iii–285. IEEE, 2005. ISBN 0780388747.

[33] E Bollt. Attractor modelling and empirical nonlinear model reduction of dissipative dynamical systems. *Int. J. of Bifurcation and Chaos*, 17:1199–1219, 2007.

[34] J.B. Tenenbaum, V. Silva, and J.C. Langford. A global geometric framework for nonlinear dimensionality reduction. *Science*, 290(5500):2319, 2000. doi: 10. 1126/science.290.5500.2319.

[35] L K Saul and S T Roweis. Think globally, fit locally: unsupervised learning of low dimensional manifolds. *Journal of Machine Learning Research*, 4:119–155, 2003.

[36] S T Roweis and L K Saul. Nonlinear dimensionality reduction by locally linear embedding. *Science*, 260:2323–2326, 2000.

[37] M Belkin and P Niyogi. Laplacian eigenmaps for dimensionality reduction and data representation. *Neural Computation*, 15:1373–1396, 2003.

[38] I T Jolliffe. *Principal Component Analysis*. Springer, New York, 1986.

[39] R A Fisher. The Statistical Utilization of Multiple Measurements. *Annals of Eugenics*, 8:376–386, 1938.

[40] K Fukunaga. *Introduction to Statistical Pattern Recognition*. Academic Press, 2 edition, 1990.

[41] Pierre and Comon. Independent component analysis, A new concept? *Signal Processing*, 36(3):287–314, 1994. ISSN 0165-1684. doi: 10.1016/0165-1684(94) 90029-9.

[42] Christian Jutten and Jeanny Herault. Blind separation of sources, part I: An adaptive algorithm based on neuromimetic architecture. *Signal Processing*, 24 (1):1–10, 1991. ISSN 0165-1684. doi: 10.1016/0165-1684(91)90079-X.

[43] T F Cox and M A Cox. *Multidimensional Scaling*. Chapman and Hall, London, 1994.

[44] J B Tenenbaum, V de Silva, and J Langford. A global geometric framework for nonlinear dimensionality reduction. *Science*, 260:2319–2323, 2000.

BIBLIOGRAPHY

[45] R Coifman and S Lafon. Diffusion Maps. *Applied and Computational Harmonic Analysis*, 21:5–30, 2006.

[46] E W Dijkstra. A note on two problems in connexion with graphs. *Numerische Mathematik*, 1(1):269–271, 1959. ISSN 0029599X. doi: 10.1007/BF01386390.

[47] Robert W Floyd. Algorithm 245: Treesort. *Commun. ACM*, 7(12):701—, December 1964. ISSN 0001-0782. doi: http://doi.acm.org/10.1145/355588.365103.

[48] Mikhail Belkin. Laplacian eigenmaps for dimensionality reduction and data representation. *Neural computation*, 15(6):1373–1396, 2003.

[49] Mikhail Belkin and Partha Niyogi. Laplacian eigenmaps and spectral techniques for embedding and clustering. *Advances in neural information processing systems*, 14:585–591, 2001.

[50] LJP Van der Maaten, EO Postma, and HJ Van den Herik. Dimensionality reduction: A comparative review. *Published online*, 10(February):1–35, 2007.

[51] William N Anderson. Eigenvalues of the Laplacian of a graph. *Linear and Multilinear Algebra*, 18(2):141–145, 1985. ISSN 03081087. doi: 10.1080/03081088508817681.

[52] F R K Chung. *Spectral Graph Theory*, volume 92 of *CBMS Regional Conference Series in Mathematics*. American Mathematical Society, 1997. ISBN 0821803158.

[53] T Zhang, Jie Yang, Deli Zhao, and Xinliang Ge. Linear local tangent space alignment and application to face recognition. *Neurocomputing*, 70(7-9):1547–1553, 2007. ISSN 09252312. doi: 10.1016/j.neucom.2006.11.007.

[54] Gelan Yang, Xue Xu, and Jianming Zhang. Manifold Alignment via Local Tangent Space Alignment. *2008 International Conference on Computer Science and Software Engineering*, pages 928–931, 2008. doi: 10.1109/CSSE.2008.1332.

[55] David L Donoho and Carrie Grimes. Hessian eigenmaps: Locally linear embedding techniques for high-dimensional data. *Proceedings of the National Academy of Sciences of the United States of America*, 100(10):5591–5596, 2003.

[56] D Donoho and C Grimes. Hessian eigenmaps: new tools for nonlinear dimensionality reduction. In *Proceedings of National Academy of Science*, volume 100, pages 5591–5596, 2003.

[57] Chittaranjan Pradhan and S. Mishra. Optimized ISOMAP algorithm using similarity matrix. In *Electronics Computer Technology (ICECT), 2011 3rd International Conference on*, volume 5, pages 212–215. IEEE, 2011.

[58] V. Silva and J.B. Tenenbaum. Global versus local methods in nonlinear dimensionality reduction. *Advances in neural information processing systems*, 15: 705–712, 2003.

BIBLIOGRAPHY

[59] Dongfang Zhao and Li Yang. Incremental isometric embedding of high-dimensional data using connected neighborhood graphs. *IEEE transactions on pattern analysis and machine intelligence*, 31(1):86–98, January 2009. ISSN 0162-8828. doi: 10.1109/TPAMI.2008.34.

[60] Yaozhang Pan, Shuzhi Sam Ge, and Abdullah Al Mamun. Weighted locally linear embedding for dimension reduction. *Pattern Recognition*, 42(5):798–811, 2009.

[61] J Zinn-Justin. *Quantum field theory and critical phenomena*. International series of monographs on physics. Clarendon Press, 2002. ISBN 9780198509233.

[62] C R Johnson and American Mathematical Society. *Matrix theory and applications*. Proceedings of symposia in applied mathematics. American Mathematical Society, 1990. ISBN 9780821801543.

[63] J Ham, D D Lee, S Mika, and B Scholköpf. A kernel view of the dimensionality reduction of manifolds. Technical Report TR-110, Max-Planck-Institut für Biologische Kybernetik, Tübingen, 2003.

[64] L J P van der Maaten, E O Postma, and H J van den Herik. Dimensionality Reduction: A comparative review. Technical Report 2009-05, Tilburg centre for Creative Computing, Tilburg University, The Netherlands, 2009.

[65] D H Kim and L H Finkel. Hyperspectral image processing using locally linear embedding. In *First International IEEE EMBS Conference on Neural Engineering*, pages 316–319, 2003.

[66] D Mateus, F Cuzzolin, R Horaud, and E Boyer. Articulated shape matching using locally linear embedding and orthogonal alignment. In *IEEE International Conference on Computer Vision*, pages 1–8, 2007.

[67] A N Tikhonov and V Y Arsenin. *Solutions of Ill-Posed Problems*. Wiley, New York, 1977.

[68] S. Markward S. Schuon, M. Durkovic, K. Diepold, J. Scheuerle. Truly Incremental locally linear embedding in : 1st International Workshop on Cognition for Technical Systems. Technical report.

[69] Daniel Cross and R. Gilmore. Complete set of representations for dissipative chaotic three-dimensional dynamical systems. *Physical Review E*, 82(5):1–5, November 2010. ISSN 1539-3755. doi: 10.1103/PhysRevE.82.056211.

BIBLIOGRAPHY

Appendix A: Paper accepted by the International Journal of Bifurcation and Chaos (IJBC-D-10-00276)

Dimension Reduction for Analysis of Unstable Periodic Orbits Using Locally Linear Embedding

Benjamin Coy

Department of Physics, Drexel University, 3141 Chestnut Street
Philadelphia, PA 19104, USA
btc24@drexel.edu

An autonomous four-dimensional dynamical system is investigated through a topological analysis. This system generates a chaotic attractor for the range of control parameters studied and we determine the organization of the unstable periodic orbits (UPOs) associated with the chaotic attractor. Surrogate UPOs were found in the four-dimensional phase space and pairs of these orbits were embedded in three-dimensions using Locally Linear Embedding. This is a dimensionality reduction technique recently developed in the machine learning community. Embedding pairs of orbits allows the computation of their linking numbers, a topological invariant. A table of linking numbers was computed for a range of control parameter values which shows that the organization of the UPOs is consistent with that of a Lorenz-type branched manifold with rotation symmetry.

Keywords: Unstable periodic orbit; locally linear embedding; linking number.

1. Introduction

Strange attractors in $\mathbb{R}^3$ are remarkably well understood because they may be classified through a topological analysis. This involves determining the organization of the unstable periodic orbits in the attractor by computing linking numbers for pairs of these orbits. This topological invariant can be calculated in $\mathbb{R}^3$ but there is no analog for higher dimensions.

It is possible for a higher dimensional dynamical system to generate a strange attractor, with Lyapunov dimension $D_L < 3$, that is essentially three dimensional (that is, in principle there is a three-dimensional

manifold in which the attractor can be embedded) [Moroz *et al.*, 2007]. In this case, a topological analysis can be carried out provided that a suitable three dimensional embedding can be found. Due to the uniqueness theorem [Arnol'd, 1978], trajectories in the embedding cannot self-intersect. If an embedding can be found, on a three-dimensional manifold, then a topological analysis can be carried out in the same way as for strange attractors in $\mathbb{R}^3$. Recent advances in dimensionality reduction techniques enable us to find a three dimensional representation of the orbits, without any self-intersections, for some strange attractors with Lyapunov dimension satisfying the condition $D_L < 3$. In section 5 we find a three dimensional representation of a strange attractor in $\mathbb{R}^4$, or more accurately of the unstable periodic orbits in this attractor.

This work is organized as follows. In section 2 we describe how strange attractors in $\mathbb{R}^3$ can be analyzed using topological methods. In section 3 we introduce a four-dimensional dynamical system. We review a previous study on this system involving projections of the strange attractor into three-dimensional subspaces. In section 4 we discuss dimensionality reduction as developed by the machine learning community. We differentiate between the types of projections in section 3 and those in section 4 by referring to the mappings described in section 3 as simple projections and the result of a dimensionality reduction technique as a projection. In particular, we focus on the Locally Linear Embedding (LLE) algorithm. In section 5 we explain how the LLE algorithm can be applied to surrogate periodic orbits within the strange attractor. We then give the results of this procedure, including the linking numbers for pairs of periodic orbits. We summarize our results in section 6.

2. Background

Strange attractors in $\mathbb{R}^3$ can be classified in the sense that one attractor is equivalent to another when there is a smooth deformation that takes one to the other in a continuous way. This classification scheme is topological and provides, for each attractor, a branched manifold that describes the mechanism acting on the flow to create the strange attractor. This approach relies on a theorem due to Birman & Williams [1983a,b]. The theorem identifies two points in phase space if they have the same asymptotic future. This can be formally stated as,

$$\mathbf{x} \approx \mathbf{y} \quad \text{if} \quad |\mathbf{x}(t) - \mathbf{y}(t)| \xrightarrow{t \to \infty} 0. \tag{1}$$

This identification corresponds to projecting the flow along the stable direction to a two-dimensional

---

APPENDIX A: PAPER ACCEPTED BY THE INTERNATIONAL JOURNAL OF BIFURCATION AND CHAOS

branched manifold. Under this projection the forward flow is uniquely determined but these trajectories no longer have unique histories. The flow in $\mathbb{R}^3$ becomes a semi-flow on the branched manifold. The important aspect of the Birman-Williams theorem is that when a strange attractor is projected down to the branched manifold the unstable periodic orbits remain unchanged, in the following way. In the projection, there are the same number and type of periodic orbits with the same topological organization as those in the strange attractor.

The topological organization of the orbits can be determined by computing the Gauss linking number for pairs of orbits [Holmes & Williams, 1985; Mindlin & Solari, 1995]. The linking number is defined as,

$$\text{LN}(A, B) = \frac{1}{4\pi} \oint_A \oint_B \frac{(\mathbf{r}_A - \mathbf{r}_B) \cdot (d\mathbf{r}_A \times d\mathbf{r}_B)}{|\mathbf{r}_A - \mathbf{r}_B|^3}. \tag{2}$$

Alternatively, the linking number can be computed by counting crossings in a two-dimensional projection. Each intersection of the orbits in the projection is assigned an integer ± 1. The sign is determined by considering tangent vectors to each orbit in the direction of the flow at the point of intersection. If the rotation of the upper segment (closer to the observer) tangent vector into the lower tangent vector is counter-clockwise then the crossing is assigned a value $+1$. If the rotation is clockwise the crossing is assigned a value -1. The linking number is simply half the sum of the signed crossings.

A table of the linking numbers for pairs of periodic orbits describes their organization on the branched manifold and within the strange attractor. The mechanism that produces the strange attractor can be identified from the particular type of branched manifold. In fact, only the linking numbers for a few of the lowest period orbits are usually required to determine the mechanism responsible for chaotic behavior [Carroll, 1999].

Many strange attractors have been studied using this topological approach in three-dimensional phase space. However, the lack of a higher dimensional analog to the Gauss linking number prevents this method from being extended to higher dimensions. It is for this reason that a method of dimensionality reduction, for attractors in higher dimensional spaces, is desirable.

3. A Four-Dimensional Dynamical System

Here we will consider an autonomous four-dimensional dynamical system that generates a strange attractor with Lyapunov dimension, $D_L < 3$. Although the strange attractor exists in $\mathbb{R}^4$ it is essentially three dimensional. If the attractor can be embedded in $\mathbb{R}^3$ then a topological analysis can be carried out. The

---

APPENDIX A: PAPER ACCEPTED BY THE INTERNATIONAL JOURNAL OF BIFURCATION AND CHAOS

four-dimensional dynamical system we will be considering is the extended Malkus-Robbins (EMR) system [Moroz, 2003, 2005],

$$
\begin{aligned}
\dot{X} &= \sigma(Y - X) - \nu^2 \beta U \\
\dot{Y} &= \frac{RX}{\nu} - Y - XZ \\
\dot{Z} &= -\nu Z + XY \\
\dot{U} &= X - \Lambda U,
\end{aligned}
\tag{3}
$$

where X, Y, Z and U are the state variables and σ, ν, R, β and Λ are control parameters. These dynamical equations are an extension of the Malkus-Robbins dynamo equations [Robbins, 1977]. They essentially describe a Lorenz-like system with feedback. The (X, Y, Z) subsystem behaves like a Lorenz attractor [Lorenz, 1963] that is coupled to the U subsystem through the control parameter β. When $\beta = 0$ Eqs. (3) become identical to the Lorenz equations under the correspondence,

$$
(\sigma, R/\nu, \nu) \to (\sigma, r, b).
\tag{4}
$$

The classic choice of Lorenz parameters $(\sigma, b, r) = (10, 8/3, 28)$ corresponds to $(\sigma, \nu, R) = (10, 8/3, 74.667)$. These values will be used throughout along with $\Lambda = 3.2$. For this particular choice of the control parameters chaotic solutions extend well into the $\beta > 0$ regime, until $\beta \approx 8$ at which point a boundary crisis destroys the attractor [Letellier *et al.*, 2007]. We will consider the strange attractor generated by Eqs. (3) for these values of the control parameters over the range of values $0 \leq \beta \leq 8.0$. An X-Z projection of the strange attractor for $\beta = 3.0$ is shown in Fig. 1.

3.1. *Unstable periodic orbits*

Topological analyses of strange attractors can be based upon the set of unstable periodic orbits (UPOs) within the attractor. A relatively small number are required [Gilmore & Letellier, 2006] and we will focus our attention on the orbits of lowest period. The UPOs may be found by the method of close returns [Gilmore, 1998]. Since (3) is a four variable system we search for trajectories satisfying,

$$
\| \mathbf{X_i} - \mathbf{X_j} \| < \delta,
\tag{5}
$$

APPENDIX A: PAPER ACCEPTED BY THE INTERNATIONAL JOURNAL OF BIFURCATION AND CHAOS
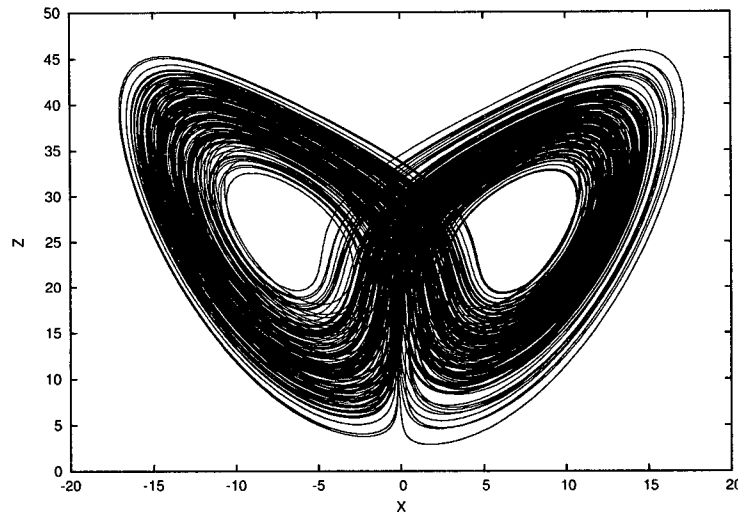
Fig. 1. The X-Z projection of the strange attractor for $(\sigma, \nu, R, \beta, \Lambda) = (10, 8/3, 74.667, 3.0, 3.2)$.

where $\mathbf{X_i} = \mathbf{X}(t_i)$ and $\|\mathbf{X}\| = \sqrt{X^2 + Y^2 + Z^2 + U^2}$. The parameter δ is usually chosen to be about 1% of the diameter of the strange attractor [Gilmore & Lefranc, 2002]. The actual value used depends on a compromise between the accuracy of the surrogates and how many are required. A more stringent threshold will result in fewer surrogates that are very good in the sense that they close up well and represent the UPO accurately. In this case δ was chosen to be 0.1 which is $\sim 0.2\%$ of the diameter of the strange attractor.

The method of close returns allows us to find trajectories that evolve around the attractor and return to a neighborhood of the starting point. Each surrogate orbit can be labeled using a symbol representation introduced by [Moroz *et al.*, 2007] which is based on the labeling used for the Lorenz attractor [Byrne *et al.*, 2004; Letellier *et al.*, 2005]. The symbol representation is a sequence of the symbols L and R indicating passage in the neighborhood of the left or right focus respectively. This passage is checked by the use of a Poincaré section consisting of two half infinite planes, each centered on one of the foci of the attractor. The number of times that a UPO intersects these two planes is simply the topological period of the orbit. For example, the period three orbit shown in Fig. 2 intersects the left component of the Poincaré section once and the right component twice.

Fig. 2 illustrates the natural way to label each of the UPOs. Every orbit is labeled by two symbols, L and R, indicating intersection with component L or R of the Poincaré section. Under this labeling scheme the orbit shown in Fig. 2 is LR^2.
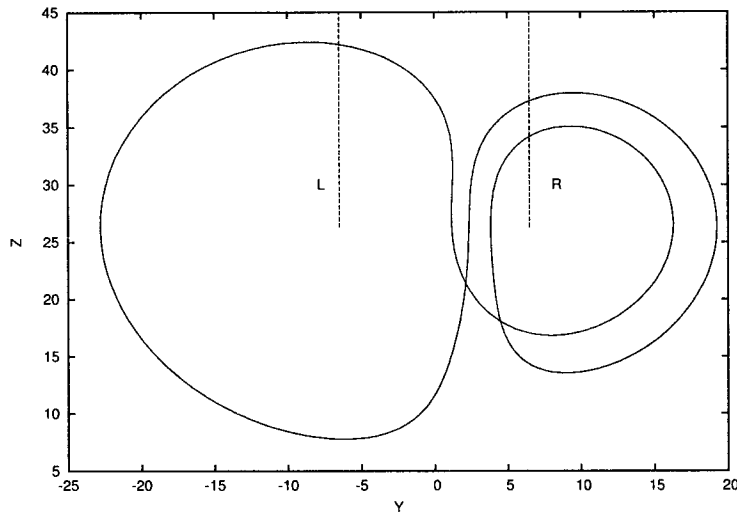
APPENDIX A: PAPER ACCEPTED BY THE INTERNATIONAL JOURNAL OF BIFURCATION AND CHAOS

the table of linking numbers for several values of β. For each value of the parameter, β, the table of linking numbers is checked for compatibility with a branched manifold.

Such an analysis has been carried out on projections of the strange attractor [Moroz *et al.*, 2007]. The two simplest projections considered were from (X, Y, Z, U) to (X, Y, Z) and (X, Y, U). In the projected subspaces the linking number for pairs of orbits can be calculated either by the Gauss linking integral, Eq. (2), or more simply by counting crossings in a two-dimensional projection. The linking number is simply half the sum of the signed crossings in the two-dimensional projection.

Moroz *et al.* [2007] showed that the (X, Y, Z) projection was described by a Lorenz type branched manifold with rotation symmetry for small values of the control parameter, $0 < \beta < 0.6$. For intermediate values, $0.6 < \beta < 5.4$, the projected subspace failed to provide an embedding. For large values, $5.4 < \beta < 7.9$, the subsystem was described by the mirror image of the branched manifold for the small-β regime. This was determined by the fact that the linking numbers decreased through integer steps, in the intermediate-β range, eventually assuming the negative of the value in the small-β regime. As the linking numbers change, for intermediate values of β, trajectories in the three-dimensional phase space undergo self-intersections. This violates the uniqueness principle, in the subspace, and prevents the projection from providing an embedding.

The projection $(X, Y, Z, U) \to (X, Y, U)$ exhibits different behavior. This projection is described by a Lorenz branched manifold with inversion symmetry for most, but not all, values of β. In contrast to previously published results [Moroz *et al.*, 2007], we found that some orbit pairs exhibited a change in their linking number, in this projection, as β is varied. Specifically, orbits LR and $LLRLR$ have LN $= +1$ for $\beta = 0.8$ (Fig. 3) and LN $= 0$ for $\beta = 4.83$ (Fig. 4). This means that the (X, Y, U) projection does not remain an embedding for all values of β.

This change in the linking number suggests there are self-intersections of the attractor in the same way as was observed for the (X, Y, Z) projection. To test for this we computed the linking numbers over the entire range of the control parameter, $0 < \beta < 8.0$. We found that the linking number was $+1$ for $\beta < 1.4$ and 0 for $\beta > 1.4$.

As a final check, the minimum distance between the pair of UPOs for each value of β was computed. Fig. 5 shows a plot of this minimum distance as a function of the control parameter.

Each time a self-intersection occurs in the (X, Y, Z) projection a sharp downward spike is observed. These correspond to the values of β where the linking numbers systematically decrease through integer steps. The plot of minimum distance for the (X, Y, U) projection also tends toward zero for $\beta \approx 1.4$.

APPENDIX A: PAPER ACCEPTED BY THE INTERNATIONAL JOURNAL OF BIFURCATION AND CHAOS
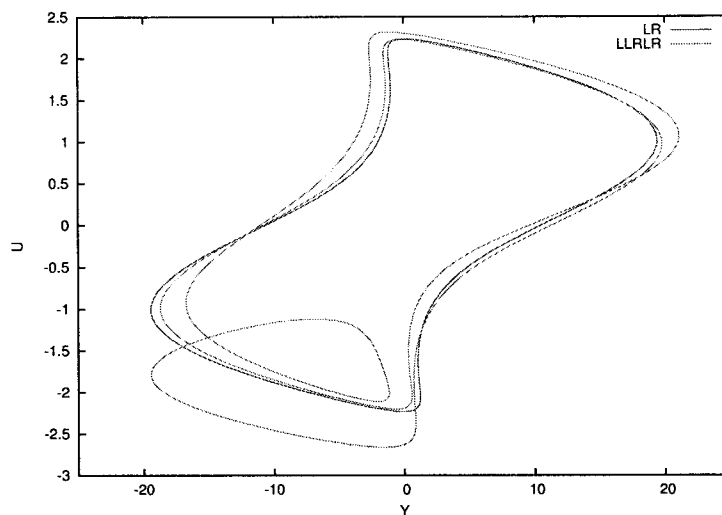
8   *Benjamin Coy*

Fig. 3.   The Y-U projection of the two UPOs LR and $LLRLR$ for $\beta = 0.8$. Their linking number is +1 for this value of the control parameter, β.
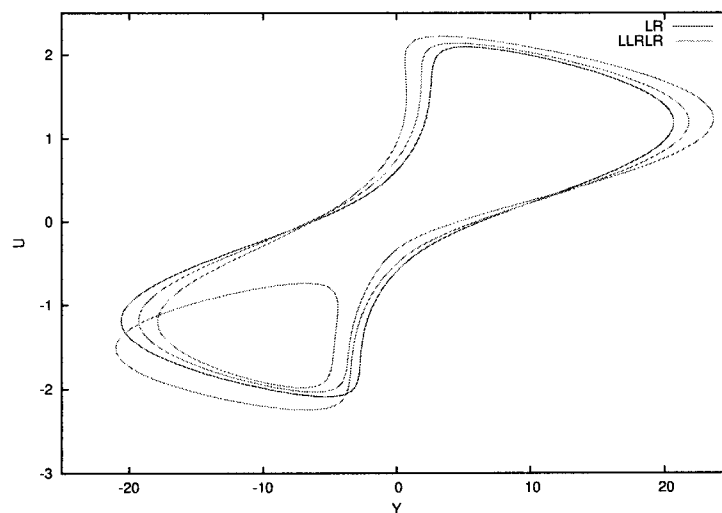
Fig. 4.   The Y-U projection of the two UPOs LR and $LLRLR$ for $\beta = 4.83$. Their linking number is zero for this value of the control parameter, β.

The minimum distance in the full four-dimensional phase space never tends to zero due to the uniqueness principle.

It is now clear that self-intersections occur in the (X, Y, U) subspace as the linking number changes
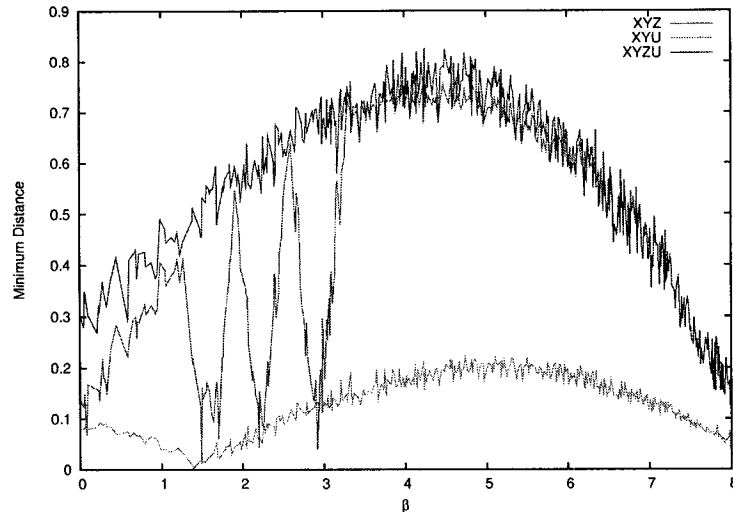
APPENDIX A: PAPER ACCEPTED BY THE INTERNATIONAL JOURNAL OF BIFURCATION AND CHAOS

Fig. 5. The minimum distance between the orbits LR and $LLRLR$ as a function of β. The minimum distance is shown for the two simplest projections, (X, Y, Z) and (X, Y, U) as well as the full four dimensional space.

value and this projection is not an embedding. Since simple projections of the attractor do not provide embeddings we turn to other dimensionality reduction techniques.

4. Dimensionality Reduction

Dimensionality reduction techniques have been developed to find low dimensional structure within high dimensional data sets. More specifically, for a data set consisting of N vectors, each of dimension D, the points in the data set may lie on or near to a manifold of dimension d (where $d < D$). Dimensionality reduction algorithms find a d-dimensional representation that best preserves certain geometric properties of the data.

Two classical methods in this field are principal component analysis (PCA) [Jolliffe, 1986] and linear discriminant analysis (LDA) [Fisher, 1938; Fukunaga, 1990]. These techniques are linear in nature and nonlinear structure within a data set is essentially invisible to these methods. In recent years, many nonlinear techniques have been developed. Some of these build on linear methods, such as isometric feature mapping (Isomap) [Tenenbaum *et al.*, 2000], which is an extension of classical multidimensional scaling [Cox & Cox, 1994], whilst others adopt an entirely new approach. Some of the more popular techniques include the Isomap algorithm [Tenenbaum *et al.*, 2000]; locally linear embedding [Roweis & Saul, 2000]; Laplacian eigenmaps [Belkin & Niyogi, 2003] and diffusion maps [Coifman & Lafon, 2006]. They were developed

---

for manifold learning, in the machine learning community, for applications such as facial recognition and handwritten character recognition.

The problem of finding lower dimensional structure in a high-dimensional data set is common to many areas of science and it is no surprise that these techniques have become more widely used in other fields of research. One example is the use of these techniques in the study of dynamical systems [Bollt, 2007].

These nonlinear algorithms tend to be computationally expensive for large data sets. For this reason we decided not to apply them to the entire attractor but to the UPOs. This allows the techniques to be used to determine the organization of the UPOs within the attractor by computing the linking numbers for pairs of orbits.

We have studied all the methods indicated above. Here we choose to focus on the LLE algorithm to reduce UPOs, in four-dimensional phase space, to a representation in three dimensions. This was partly due to computational efficiency since LLE was found to perform much quicker than the Isomap algorithm. Laplacian eigenmaps require a uniform sampling of the underlying manifold. LLE, however, is robust to different sampling methods which allows us to sample points from the attractor that lie near to the UPOs that we wish to study. Finally, LLE has an intuitive approach that involves reconstructing each data point from its nearest neighbors. The algorithm requires only two input parameters, the target dimension and the number of nearest neighbors. Diffusion maps require other input parameters and the embedding can be quite sensitive to the choice of these parameter values.

In short, LLE seems to combine good performance with an acceptable computational cost. The LLE algorithm will now be explained in more detail.

4.1. *Review of locally linear embedding*

LLE assumes that each data point in a high dimensional space lies on a lower dimensional nonlinear manifold [Saul & Roweis, 2003]. The input to the algorithm is a set of N vectors in $\mathbb{R}^D$ that lie on a manifold of dimension d, with $d < D$. Furthermore, it is assumed that each data point and its neighbors lie close to a locally linear patch of the manifold. The algorithm aims to reconstruct the original data set in a lower dimensional space that best preserves the local geometry of every neighborhood and outputs a set of N vectors in $\mathbb{R}^d$. There are three main steps to the algorithm:

(1) Assign neighbors to each data point in the original data set.

(2) Compute the weights that best linearly reconstruct each data point from its neighbors.

(3) Find the vectors in the low-dimensional space by fixing the weights to be those found in step (2) and

---

APPENDIX A: PAPER ACCEPTED BY THE INTERNATIONAL JOURNAL OF BIFURCATION AND CHAOS

minimizing a cost function.

Each of these steps will now be explained in more detail.

Assigning the nearest neighbors to each data point usually involves one of two methods. This is to either take the K-nearest data points based on Euclidean distance (K-nearest neighbors) or to choose the neighbors contained in a ball of fixed radius, ϵ, centered on each data point (ϵ-ball).

Consider a data set consisting of N points. By thinking of each data point in the higher-dimensional space as a vector, $\vec{X}_i$, each can be reconstructed through a linear combination of its neighbors. The error in this reconstruction is measured by the cost function,

$$\varepsilon(W) = \sum_{i=1}^{N} |\vec{X}_i - \sum_{j \neq i} W_{ij} \vec{X}_j|^2, \tag{6}$$

which adds up the squared distances between all the data points and their reconstructions. The weights, W_{ij}, are found by minimizing this cost function subject to two constraints. The first is that each data point is reconstructed only from its neighbors, i.e. $W_{ij} = 0$ if $\vec{X}_j$ is not a neighbor of $\vec{X}_i$. The second constraint is $\sum_j W_{ij} = 1$, which imposes translational invariance.

The third step also involves minimization of the cost function. However, this time the weights are fixed and the vectors are found that minimize the reconstruction error. The weights from step two are used in minimizing the embedding cost function,

$$\Phi(Y) = \sum_{i=1}^{N} |\vec{Y}_i - \sum_{j \neq i} W_{ij} \vec{Y}_j|^2, \tag{7}$$

where $\vec{Y}$ are the low dimensional embedding vectors.

The minimization is performed subject to two constraints. The first constraint removes the translational degree of freedom such that the output vectors, $\vec{Y}_i$, are centered on the origin,

$$\sum_i \vec{Y}_i = \vec{0}. \tag{8}$$

The second constraint removes the rotational degree of freedom such that the output vectors have unit covariance,

APPENDIX A: PAPER ACCEPTED BY THE INTERNATIONAL JOURNAL OF BIFURCATION AND CHAOS

$$\frac{1}{N} \sum_i \vec{Y}_i \vec{Y}_i^\mathsf{T} = I. \tag{9}$$

The embedding cost function Eq. (7) can be rewritten in terms of a cost matrix,

$$\Phi(Y) = \sum_{ij} M_{ij}(\vec{Y}_i . \vec{Y}_j), \tag{10}$$

where the cost matrix is given by,

$$M_{ij} = \delta_{ij} - W_{ij} - W_{ji} + \sum_k W_{ki} W_{kj}. \tag{11}$$

Minimizing Eq. (7) is equivalent to finding the eigenvectors corresponding to the $d + 1$ lowest eigenvalues of the cost matrix.

The result of applying this algorithm to points sampled from a two dimensional manifold in $\mathbb{R}^3$ is shown in Fig. 6.
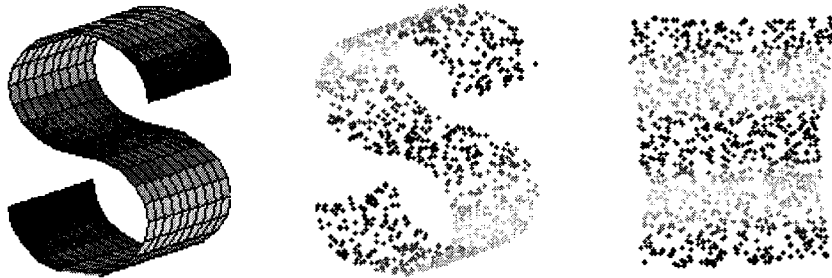

Fig. 6.   LLE applied to the two dimensional S-shaped manifold using the MATLAB procedure by Saul & Roweis [2003] that is publicly available from http://cs.nyu.edu/~roweis/lle/. 1000 points were sampled from the known manifold and the resulting embedding was computed using 12 nearest neighbors.

The S-shaped manifold is a common example used for testing dimensionality reduction techniques [Ham *et al.*, 2003]. In this case 1000 points were sampled from the manifold and 12 nearest neighbors were used to compute the two dimensional embedding. The rightmost image in Fig. 6 shows how the LLE algorithm is capable of unfolding the data set to reveal the intrinsic two dimensional structure. LLE has also been successfully applied to other manifolds, such as the "Swiss Roll" manifold [van der Maaten *et al.*,

APPENDIX A: PAPER ACCEPTED BY THE INTERNATIONAL JOURNAL OF BIFURCATION AND CHAOS

2009]. Some example applications of LLE include analysis of data sets of hyperspectral images [Kim & Finkel, 2003] and articulated shape matching [Mateus *et al.*, 2007].

LLE aims to preserve intrinsic geometric properties of every neighborhood and these intrinsic properties are characterized by the reconstruction weights W_{ij}. We additionally constrain these weights to satisfy $\sum_j W_{ij} = 1$ so that for any particular data point, they are invariant to translations in addition to rotations and rescalings of that data point and its neighbors. The algorithm is effective in revealing global nonlinear structure through the local symmetries of linear reconstructions. The effectiveness depends on the two inputs to the algorithm, the number of nearest neighbors and the embedding dimension. For problems where the data points are assumed to lie on a nonlinear manifold of known dimension the important question is: how does the choice of number of nearest neighbors affect the lower dimensional embedding? This will be addressed in the next section where the algorithm will be applied to orbits in $\mathbb{R}^4$.

5. Application of LLE to UPOs in $\mathbb{R}^4$

The UPOs that were found by the method of close returns in section 3 must be embedded in $\mathbb{R}^3$ in order to compute linking numbers and determine their topological organization. To achieve this using LLE we took two UPOs and a sample of data points from the strange attractor. These sampled points were chosen to lie near to each of the UPOs and were used as nearest neighbors in the LLE algorithm. This ensured that the underlying manifold was sufficiently sampled to produce an accurate embedding of both UPOs simultaneously.

As an example, we consider the two orbits LR and LRR. The Y-Z projection of these orbits along with the points sampled from the attractor are shown in Fig. 7.

Implementing the LLE algorithm requires only two inputs: the embedding dimension, d, and the number of nearest neighbors, K. The manifold containing the attractor is assumed to be three-dimensional, since $D_L = 2.2$, so we set $d = 3$. However the choice of the value of K is not so straightforward. If K is too small then the geometry of the manifold is not recovered due to undersampling. If K is too large then the the assumption that the neighborhood is locally linear would be violated. The aim is to find a range of K values over which the embedding remains stable. Similar arguments apply in the case of assigning neighbors using the ϵ-ball technique. This can help in avoiding the use of neighborhoods that violate the locally linear requirement. As with the nearest neighbors method, ϵ cannot be chosen too small or undersampling could occur and the aim would be to find a range of ϵ values over which the locally linear embedding remains stable.

APPENDIX A: PAPER ACCEPTED BY THE INTERNATIONAL JOURNAL OF BIFURCATION AND CHAOS
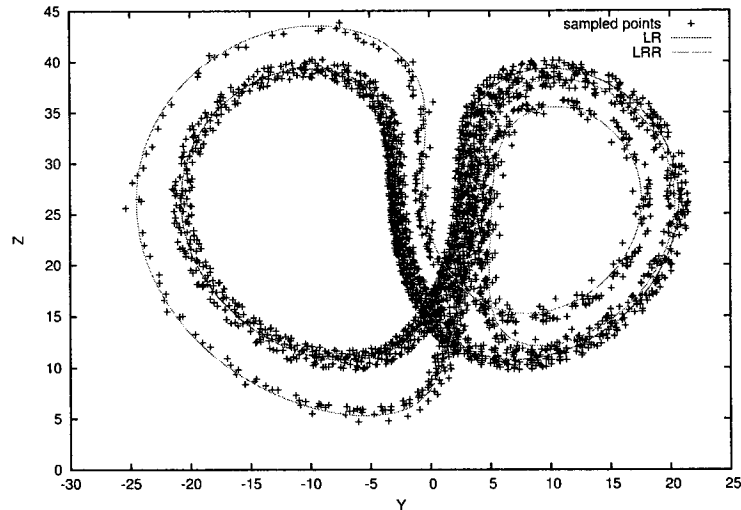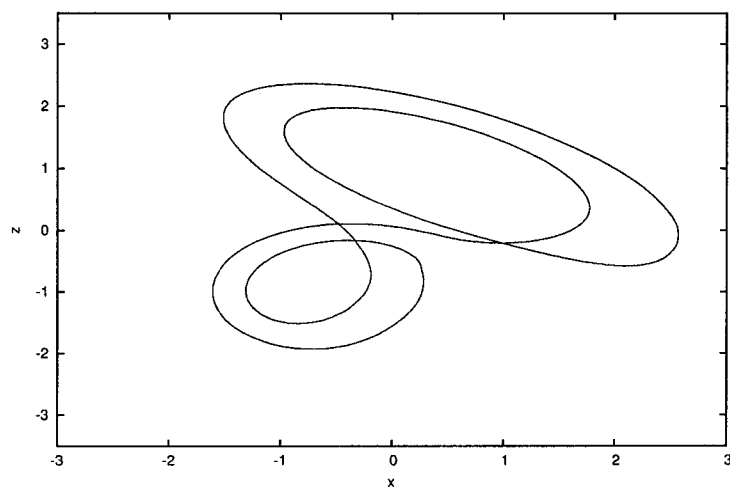
Fig. 7.   The Y-Z projection of two surrogate UPOs, LR and LRR, for $\beta = 5.0$, with 2851 points sampled from the underlying three-dimensional manifold. The orbit LR consists of 347 points and the orbit LRR consists of 556 points.

Figs. 8, 9 and 10 show the orbit LRR embedded in three dimensions for three different values of K. In each case, the points sampled from the strange attractor were removed from the data set after the LLE algorithm had been applied. Then, a specific orientation was chosen in the three-dimensional space, this is because LLE is invariant up to a rotation. The following orientation convention was adopted. For each orbit, the point closest to the component R of the Poincaré section was determined. The orbit was then rotated so that this point was on the x-axis. Orienting each orbit in the same sense allowed each of the embeddings to be compared to find the range of K values over which the embedding remained stable.

The linking numbers for pairs of orbits, in the three-dimensional embedding, were computed by counting crossings in the x-z projection. These linking numbers were computed for all values of K in the range $5 \leq K \leq 40$. For the lowest values of K the linking numbers were found to vary depending on the number of nearest neighbors used. This type of error should be expected from inspection of Fig. 8. However, for all pairs of orbits, the linking number was found to remain the same for all values of K above a certain threshold value. For all the orbits studied here, $K = 20$ proved to be a sufficient number of nearest neighbors since it was contained within the range over which the linking number remained constant.

The results are shown in Table 1, for the lowest period UPOs. These results are consistent with those for the Lorenz branched manifold with rotation symmetry. The most important aspect of these results is that the table of linking numbers remains the same for the entire range of control parameter, $0 < \beta < 8.0$.

APPENDIX A: PAPER ACCEPTED BY THE INTERNATIONAL JOURNAL OF BIFURCATION AND CHAOS
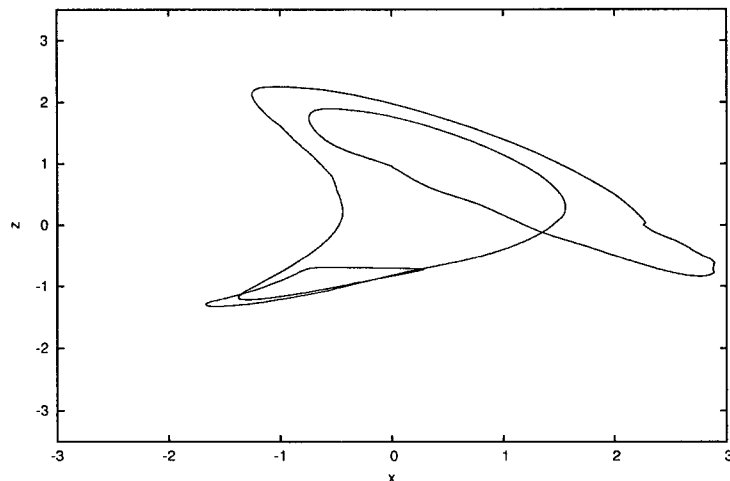
Fig. 8. Locally linear embedding of the orbit $LLRR$ for $K = 10$.

Fig. 9. Locally linear embedding of the orbit $LLRR$ for $K = 20$.

This is under the previously mentioned assumption that there is a three-dimensional manifold on which the attractor may be embedded. We did not check that the full four-dimensional dynamics are preserved in the lower dimensional subspace.

APPENDIX A: PAPER ACCEPTED BY THE INTERNATIONAL JOURNAL OF BIFURCATION AND CHAOS
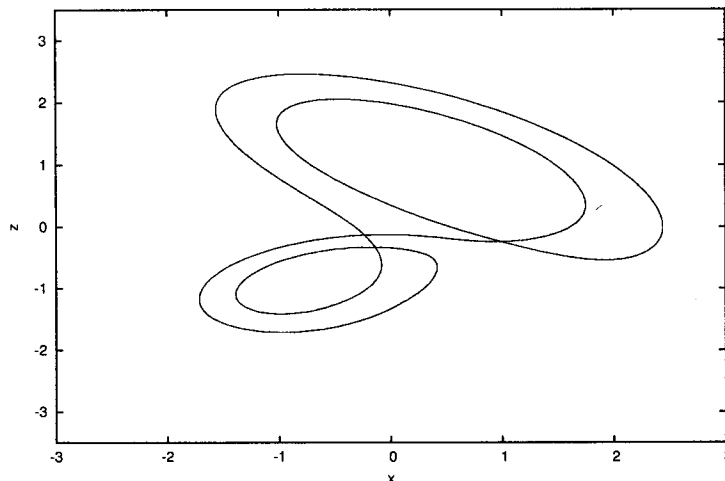
16   *Benjamin Coy*

Fig. 10.   Locally linear embedding of the orbit $LLRR$ for $K = 30$.

Table 1.   The linking numbers of unstable periodic orbits that were embedded using LLE.

	LR	LLR	LRR	LLLR	LRRR	LLRR
LR	-	1	1	1	1	2
LLR	1	-	1	2	1	2
LRR	1	1	-	1	2	2
LLLR	1	2	1	-	1	2
LRRR	1	1	2	1	-	2
LLRR	2	2	2	2	2	-

6. Conclusion

We have analyzed a four dimensional dynamical system that generates a strange attractor with Lyapunov dimension $D_L \simeq 2.2$. The analysis was dependent on the UPOs that were found by the method of close returns in the four-dimensional phase space.

We were able to use a dimensionality reduction technique, LLE, to find an alternative projection of the UPOs in $\mathbb{R}^3$. The linking numbers for pairs of these orbits were computed and these values remained constant for all values of the coupling constant in the range $0 < \beta < 8.0$. This indicates that no self-intersections occur for the dimensionality reduced orbits as β is varied. The system is described by a Lorenz-type branched manifold with rotation symmetry for all values of the control parameter, β.

The methodology described in this paper can be applied to other strange attractors that satisify the

---

APPENDIX A: PAPER ACCEPTED BY THE INTERNATIONAL JOURNAL OF BIFURCATION AND CHAOS

condition $D_L < 3$.

Acknowledgments

References

Arnol'd, V. I. [1978] *Ordinary Differential Equations* (MIT Press).

Belkin, M. & Niyogi, P. [2003] "Laplacian eigenmaps for dimensionality reduction and data representation," *Neural Computation* **15**, 1373–1396.

Birman, J. S. & Williams, R. F. [1983a] "Knotted periodic orbits in dynamical systems i: Lorenz's equations," *Topology* **22**, 47–82.

Birman, J. S. & Williams, R. F. [1983b] "Knotted periodic orbits in dynamical systems ii: Knot holders for fibered knots," *Contemporary Mathematics* **20**, 1–60.

Bollt, E. [2007] "Attractor modelling and empirical nonlinear model reduction of dissipative dynamical systems," *Int. J. of Bifurcation and Chaos* **17**, 1199–1219.

Byrne, G., Gilmore, R. & Letellier, C. [2004] "Distinguishing between folding and tearing mechanisms in strange attractors," *Phys. Rev. E.* **70**, 056214.

Carroll, T. L. [1999] "Approximating chaotic time series through unstable periodic orbits," *Phys. Rev. E.* **59**, 1615–1621.

Coifman, R. & Lafon, S. [2006] "Diffusion maps," *Applied and Computational Harmonic Analysis* **21**, 5–30.

Cox, T. F. & Cox, M. A. [1994] *Multidimensional Scaling* (Chapman and Hall, London).

Fisher, R. A. [1938] "The statistical utilization of multiple measurements," *Annals of Eugenics* **8**, 376–386.

Fukunaga, K. [1990] *Introduction to Statistical Pattern Recognition*, 2nd ed. (Academic Press).

Gilmore, R. [1998] "Topological analysis of chaotic dynamical systems," *Rev. Mod. Phys.* **70**, 1455–1529.

Gilmore, R. & Lefranc, M. [2002] *The Topology Of Chaos* (Wiley, New York).

Gilmore, R. & Letellier, C. [2006] *The Symmetry Of Chaos* (Oxford University Press, New York).

Ham, J., Lee, D. D., Mika, S. & Scholköpf, B. [2003] "A kernel view of the dimensionality reduction of manifolds," Tech. Rep. TR-110, Max-Planck-Institut für Biologische Kybernetik, Tübingen.

Holmes, P. & Williams, R. F. [1985] "Knotted periodic orbits in suspensions of Smale's horseshoe: torus knots and bifurcation sequences," *Archive for Rational Mechanics and Analysis* **90**, 115–194.

APPENDIX A: PAPER ACCEPTED BY THE INTERNATIONAL JOURNAL OF BIFURCATION AND CHAOS

18 REFERENCES

Jolliffe, I. T. [1986] *Principal Component Analysis* (Springer, New York).

Kim, D. H. & Finkel, L. H. [2003] "Hyperspectral image processing using locally linear embedding," *First International IEEE EMBS Conference on Neural Engineering*, pp. 316–319.

Letellier, C., Moroz, I. M. & Gilmore, R. [2007] "A topological test for embeddings," http://www.physics.drexel.edu/~bob/Papers/Long_topotest.pdf.

Letellier, C., Tsankov, T. D., Byrne, G. & Gilmore, R. [2005] "Large-scale structural reorganization of strange attractors," *Phys. Rev. E.* **72**, 026212.

Lorenz, E. N. [1963] "Deterministic nonperiodic flow," *J. Atm. Sci.* **20**, 130–141.

Mateus, D., Cuzzolin, F., Horaud, R. & Boyer, E. [2007] "Articulated shape matching using locally linear embedding and orthogonal alignment," *IEEE International Conference on Computer Vision*, pp. 1–8.

Mindlin, G. B. & Solari, H. G. [1995] "Topologically inequivalent embeddings," *Phys. Rev. E.* **52**, 1497–1502.

Moroz, I. M. [2003] "The Malkus-Robbins dynamo with a linear series motor," *Int. J. of Bifurcation and Chaos* **13**, 147–161.

Moroz, I. M. [2005] "The extended Malkus-Robbins dynamo as a perturbed Lorenz system," *Nonlinear Dynamics* **41**, 191–210.

Moroz, I. M., Letellier, C. & Gilmore, R. [2007] "When are projections also embeddings?" *Phys. Rev. E.* **75**, 046201.

Robbins, K. A. [1977] "A new approach to sub-critical instability and turbulent transitions in a simple dynamo," *Math. Proc. Cambridge Philos. Soc.* **82**, 309–325.

Roweis, S. T. & Saul, L. K. [2000] "Nonlinear dimensionality reduction by locally linear embedding," *Science* **260**, 2323–2326.

Saul, L. K. & Roweis, S. T. [2003] "Think globally, fit locally: unsupervised learning of low dimensional manifolds," *Journal of Machine Learning Research* **4**, 119–155.

Tenenbaum, J. B., de Silva, V. & Langford, J. [2000] "A global geometric framework for nonlinear dimensionality reduction," *Science* **260**, 2319–2323.

van der Maaten, L. J. P., Postma, E. O. & van den Herik, H. J. [2009] "Dimensionality reduction: A comparative review," Tech. Rep. 2009-05, Tilburg centre for Creative Computing, Tilburg University, The Netherlands.

APPENDIX A: PAPER ACCEPTED BY THE INTERNATIONAL JOURNAL OF BIFURCATION AND CHAOS

Vita

Benjamin Thomas Coy was born in Hillingdon, England, on 21 July 1981. From 1999 to 2003 he attended Warwick University, graduating with honors in physics. In September 2003 he began his graduate studies at Drexel University in Philadelphia, Pennsylvania. He obtained his *scientiarum magister* in physics in 2006, and he completed his *philosophiae doctor* in physics in 2011 under the direction of Robert Gilmore.